The Proof of Concept of a Fused Radiometric and Optical Stereoscopic Imaging System

Thesis submitted in accordance with the requirements of the
University of Liverpool for the degree of
Doctor in Philosophy

by

Jamie Dormand

Oliver Lodge Laboratory

July 2014

Abstract

The proof of concept of a fused radiometric and optical stereoscopic imaging device is presented. The project was in collaboration with the National Nuclear Laboratory and the Nuclear Decommissioning Authority with the aim of developing a sensor that can be deployed in a nuclear decommissioning environment. The radiometric system was a Compton camera comprised of two HPGe planar detectors and presents a significant improvement in efficiency and dynamic range over coded aperture systems currently used in industry. The optical stereoscopic camera is the proprietary Bumblebee XB3 system that provides 3D physical information of the surroundings.

Two main experiments are presented; the first investigated the disparity between true source location and reconstructed image position. This disparity was proven and methods for accounting for and correcting it were developed, whereby the image position accuracy was improved by a factor of 26.7. The second experiment imaged 20 MBq ^{137}Cs sources at distances of 80 - 150 cm with both radiometric and optical stereoscopic systems simultaneously. The first fused images were produced using this data, with the radiometric sources and surroundings clearly visible. A GUI was developed in Matlab to process and fuse the data. Alongside both experiments image optimisation techniques were investigated. Pulse shape analysis was implemented and shown to improve image resolution by 30% on average at the expense of efficiency. Fold 2 event imaging was conversely shown to improve efficiency at the expense of image resolution.

This work provides the basis to develop the project towards a complete system. The steps that must be taken to realise this are outlined and recommendations for overcoming potential challenges are discussed.

Contents

List of Figures

List of Tables

Chapter 1

Introduction

Decommissioning nuclear sites in the UK presents a unique set of challenges and new technologies must be developed to meet them. The field of nuclear physics has substantial experience in producing and optimising radiation detectors and this knowledge is increasingly finding pragmatic applications in industry. In collaboration with the National Nuclear Laboratory, a project was created to investigate the feasibility of a system combining radiometric and optical stereoscopic devices for use in a nuclear decommissioning environment. Such a system must combine good radiometric energy and image resolution with an exceptional stereoscopic calibration giving accurate source position information in 3D space. Improved efficiency over current systems and the ability to operate in a strong radioactive environment are also crucial features.

This thesis outlines the theory, experimental procedures and analysis involved in the proof of concept of a radiometric/stereoscopic fused imaging system. Project motivation is provided by considering the challenges facing the nuclear decommissioning industry and the limitations of currently employed radiometric detectors.

1.1 Nuclear Decommissioning

Nuclear decommissioning refers to the process by which a nuclear facility is safely shut down following the end of its operational life. It includes the full or partial disassembly of buildings and contents, decontamination of structures that are not removed and restoration of the site of the facility. This is managed with the goal of reducing the risk the facility poses while

ensuring the risk to workers, the public and the environment is kept to a minimum during the decommissioning process [1]. Reliance on nuclear power and the increasing number of nuclear power stations reaching the end of their lifespan has fuelled growing concern about the safety and financial implications of nuclear decommissioning, reflected in both UK and international publications [1, 2]. Nuclear power facilities vary markedly in design and scale making each decommissioning a unique challenge with no standard protocol. The UK is in the unique position of having no standard design build and their facilities were built without decommissioning consideration. This in turn makes it difficult to quantify the cost and timescale; future American decommissioning has been estimated at $700 million [3] and UK decommissioning between £200-500 million per nuclear site [4]. The first full UK nuclear reactor decommissioning was completed on the Windscale Advanced Gas Cooled Reactor (WAGCR) in 2011, marking the end of a twenty year program [5]. The scale of the problem is highlighted in Figure 1.1 which shows the current UK nuclear facilities managed by the NNL. As it stands the Nuclear Decommissioning Authority of the UK estimate the total cost of management and clean up of their legacy sites at £45.1 billion, with a project time far exceeding their current 20 year plan [6]. While the exact figure remains unclear, it is evident that the ongoing nuclear decommissioning process presents a long standing financial burden on the economy. These estimates will become clearer as decommissioning experience is gained in the coming years and new technologies that can support this are sorely needed.

The prominent consideration associated with the clean-up of a radiation facility is the location and classification of radioactive waste. Figure 1.2 shows the relative masses of the waste following the decommissioning of the Greifswald power plant in Germany [7]. Over a quarter of the total waste (566 400 tonnes) is considered to have radiation levels that could pose a risk, while only a small fraction of this radioactive waste comes from dismantled parts of the nuclear power plant. This highlights the fact that the radioactive waste is not confined to the plant itself and that other nearby structures must be carefully screened as they may have potentially dangerous levels of contamination. As this makes locating radioactive waste a far more complicated process it leads to an increase in project time and costs. Systems that provide quick and accurate location of this waste would clearly be of huge benefit to the decommissioning process.

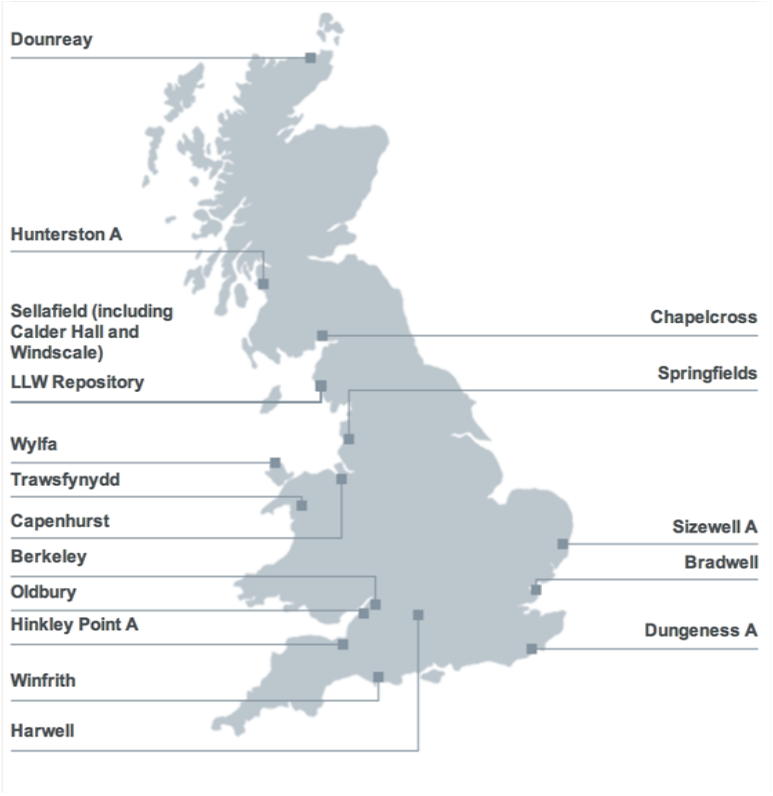

Figure 1.1: Current UK nuclear sites managed by the NNL [6].

Before radioactive waste can be located and processed correctly it is necessary to know how to classify it. Waste is graded according to the danger it poses to health and the environment and Table 1.1 gives a brief outline of the classifications described in UK radioactive waste management guidelines [8]. While High Level Waste (HLW) has the highest radioactivity levels making it the most dangerous and thus most difficult to process, the sources of HLW are clearly defined and easy to locate. Separating Intermediate Level Waste (ILW) and Low Level Waste (LLW) is a far more challenging task; As there is a specified activity that differentiates the two it is imperative any waste that can't be proven to lie below this level is treated as ILW. Waste with a radioactive content of less than 4 GBq per tonne of alpha or 12 GBq per tonne of beta or gamma activity is classed as LLW. If a material can be proven to have a radioactivity level that is so low as to present no risk to the public or the environment it can be classed as free release and no protocol for processing such waste

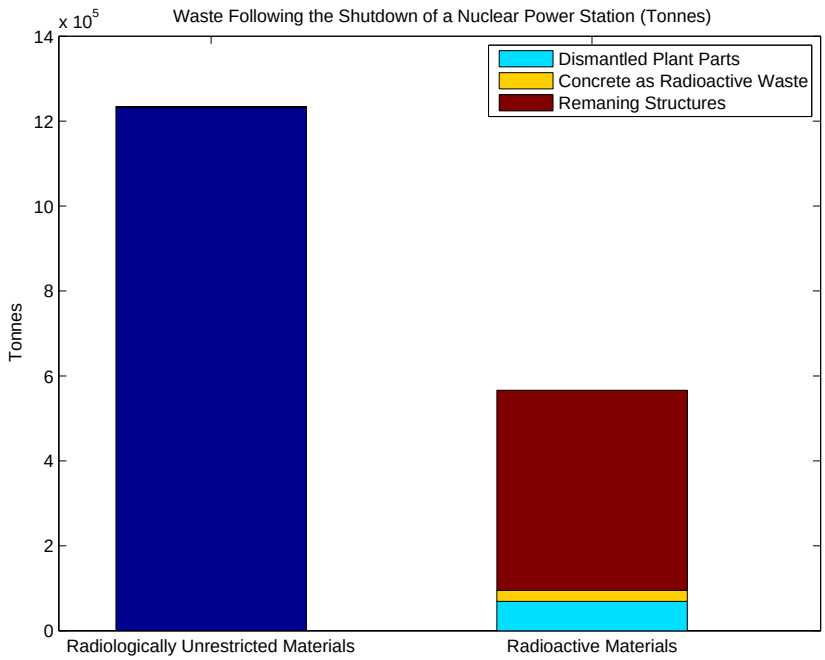

Figure 1.2: Waste generated from the decommissioning of the Greifswald nuclear power site [7].

is needed. There is a 1:125 cost ratio between processing free release and LLW material but a 1:2500 cost ratio between free release and ILW [9]. This factor of 20 in cost difference between LLW and ILW processing means there is a large financial penalty for inaccurate activity measurements.

Furthermore, radioactive waste is unlikely to have a constant activity throughout but will consist of high activity 'hot spots' on a low radiation background [10]. The location and accurate activity determination of these hot spots will make decommissioning a cheaper and safer process, making research into realising this easily justifiable. The UK has a current ILW store of 240000 m^3 which is around 7.5% that of the LLW store and this will only increase as future decommissioning projects are completed [11], so any improvements to waste classification will have a lasting benefit.

In order to locate the radioative waste and determine its activity it is important to know

	Low Level Waste (LLW)	Intermediate Level Waste (ILW)	High Level Waste (HLW)
Categorisation	Waste with a radioactive content below 4GBq/tonne of alpha or 12Gbq/tonne of beta or gamma activity.	Waste with radioactivity levels above that of LLW, but not so high as to cause rises in temperature that must be accounted for in storage design.	Waste with levels of radioactivity that cause significant increases in temperature, such that this factor must be accounted for in storage design.
Sources	Paper, plastics, scrap metal	Fuel cladding, reactor components	Reprocessed spent fuel
Safe Storage	Typically super-compacted to reduce volume before processing and near surface storage at the LLW Repository in Cumbria.	Encapsulation in cement and storage in steel drums or concrete boxes and deep storage up to hundreds of metres.	Vitrification[1], 50 years storage, further processing, storage in deep geological formations.

Table 1.1: UK radioactive waste classification [8].

the typical radioisotopes found in the waste and their properties. In a typical nuclear power generating fission reaction ^{235}U (a rare but natural Uranium isotope) absorbs thermalised neutrons to form the metastable isotope ^{236}U. This undergoes a subsequent fission decay, splitting into two fragment nuclei and two free neutrons while releasing a huge amount

[1]Vitrification is the process by which a glass is formed from a material. In this case the HLW is mixed with the glass as it is forming and placed into 150 litre stainless steel containers for easier transport and storage.

of energy. The details of these reactions is a complex area of study beyond the scope of this thesis, but the salient point is that there are many possible decay paths from this reaction. There are 37 possible fission fragments and nearly 300 isotopes produced through subsequent decays; around 80 are stable [12]. The nuclides with relatively short half-lives (much shorter than the timescale of the decommissioning process) are not so much of a concern as their activities will be negligible by the time they are due to be processed. The longer lived radionuclides form the basis of isotopes to be considered when approaching a decommissioning project [13]. Of these nuclides the radiation they emit is the critical factor for detecting and processing them safely. Radioisotopes can emit alpha, beta, gamma and neutron radiation as they undergo decay and these particles are notably different in their properties as to require very different approaches to detecting and shielding. While alpha radiation is highly ionizing it has a relatively small penetration thickness and will be stopped in a few mm of air or less than a mm of paper (though the necessity for locating alpha sources drives novel research in this area [14]). Beta particles are smaller in size and mass which increases penetration depth and makes scattering a serious problem when considering shielding. From a simple perspective however, beta particles can still be shielded using a few mm of aluminium and do not pose a serious health risk to people outside of the immediate vicinity [15]. Unfortunately their short penetration depth makes them difficult to detect and so the sources cannot be easily located.

The waste must be dismantled and screened to quantify alpha and beta contaminants. This means no information of the contamination profile can be gained from this radiation and this causes a further increase in time and cost [9]. Gamma radiation is far more penetrating and so poses a greater health risk to workers and the public resulting in thicker required shielding. Conversely the relatively transmissive nature of gamma radiation can be seen as an advantageous characteristic, as this makes it easier to detect and the sources of this radiation easier to locate. By using appropriate technology to form images from these emitted gamma rays a profile of the contaminants in an area can be built up, making the decommissioning process quicker, safer and cheaper. This is not a novel idea and gamma ray imagers have assisted decommissioning projects for over a decade in the form of coded aperture systems [16, 17]. There are drawbacks to these systems however and these will be covered in the next section. Table 1.2 shows the most significant gamma

emitting radionuclides from an imaging perspective, the most prominent emitted gamma energies and their respective half-lives [18]. As can be seen, the range of half-lives means the relative contaminant yields depends largely on the time between reactor shut down and waste processing. If the project is delayed by a few years there will be a negligible level of activity arising from ^{58}Co and ^{54}Mn and this is a prominent factor in the Safestore approach [9]. For time periods of up to 50 years ^{137}Cs poses the biggest radiation threat to those on site. However it is not unknown for the decommissioning process to begin beyond this, at which point the prevalent nuclides become ^{154}Eu and ^{94}Nb in concrete and metals respectively [18]. These nuclides emit several prominent gamma rays of various energies with a range from 122 keV to 1408 keV; this means any detector used to image these must have a large dynamic energy range. If the imaging device cannot detect these gamma rays then the sources cannot be located which will seriously hamper its ability to assist in decommissioning.

Nuclide	Half-Life (years)	Gamma Energy (MeV)
^{58}Co	0.19	0.810
^{54}Mn	0.85	0.834
^{60}Co	5.271	1.173, 1.333
^{152}Eu	13.537	0.122, 0.344, 0.779, 0.964, 1.408
^{154}Eu	8.593	0.123, 0.723, 0.873, 1.005, 1.274
^{94}Nb	20300	0.703, 0.871
^{137}Cs	30.07	0.662

Table 1.2: Significant gamma-emitting nuclides present in radioactive waste from a typical nuclear power plant [18].

In summary the challenging factors of a decommissioning project highlight the need for a gamma-ray imaging device that can accurately quantify the activity of radioactive waste. To do this effectively it requires excellent energy resolution, a large dynamic energy range and the ability to operate in a strong radioactive environment. As previously mentioned

there are already coded aperture imaging systems used for this function but the limitations of these have motivated researchers to create improved devices. In order to understand these limitations it is important to know the basic characteristics of coded aperture systems.

1.2 Coded Aperture Imaging

Coded aperture imaging is a long standing imaging approach that was first suggested as a method of forming images from low statistic sources for use in astrophysics [19]. It was also born from the limitations of a system that preceded it; the gamma pinhole camera is a system comprised of a single aperture in a shielded box that creates an inverted image of a source from its emitted gamma rays [20]. The nature of using a single hole means there is a trade off between image quality and detection efficiency as the larger the aperture size the greater angular uncertainty of detected gamma rays [21]. It is necessary to match the aperture size and thus the camera focal point to the distance from the object of interest. This is acceptable in applications such as medical imaging where the source distance is constant but a huge limitation from a decommissioning standpoint. A significant improvement was reached with the development of the Anger camera [22] that combined Sodium Iodide scintillator crystals with a lead collimator allowing positional information of gamma-ray emitting sources to be determined at a range of distances. The collimator has a grid of holes allowing the transmission of gamma-rays with a certain incident angle allowing the path of those detected to be back projected and an image to be formed. Only a small fraction of gamma-rays emitted will pass through the collimator (less than 1 %) and so a huge drop in sensitivity is required to gain positional information. The coded aperture system is an improvement on the conventional Anger camera design by using a collimator with a distinct pattern as shown in Figure 1.3. This pattern in the shielded mask causes a shadow on the position-sensitive detection medium behind with a shape dependent on the position of the gamma-ray source. A detailed understanding of this aperture pattern allows deconvolution algorithms to be used that convert the detected pattern into an image. This ensures a significant increase in sensitivity compared to the Anger camera with a negligible increase in production costs and these advantages have made coded aperture imaging the predominant gamma-ray imaging system in nuclear decommissioning [16].

As technology has improved over the past decade there is an opportunity to address

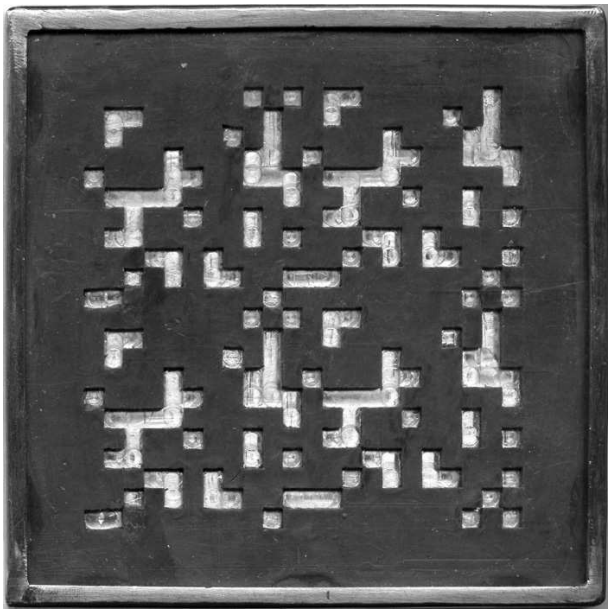

Figure 1.3: Coded aperture mask from a medical gamma camera.

some important limitations in coded aperture systems. Perhaps the crucial problem is the finite thickness of the aperture mask which reduces the operational energy range of the system. If gamma rays have sufficient energy to penetrate the shielded areas without absorption the resulting detected pattern will have no bearing on the source position and the resulting image will be rendered useless. While the energy limit of a coded aperture system is dependent on the collimator used, producing a mask that can absorb gamma rays of energies over 1 MeV is difficult to fabricate and alternate methods are required to image energy ranges above this [23]. Even below this there may be a high probability of gamma-ray transmission and coded aperture systems typically have an operational energy range below 400 keV [24]. As shown in Table 1.2 there are a number of long lived nuclides in radioactive waste that emit gamma rays with energies well above 400 keV so a coded aperture system is severely limited by its energy range in a decommissioning application.

Beyond this the detector field of view is a quality that has a profound effect on the efficiency of the system. A large field of view allows a system to scan a large area in a given time, while a small field of view means the system must be repetitively moved in order to cover a region of interest. The mechanical collimation of the coded aperture system is a

limiting factor of this field of view, as is the distance between the mask and the detector. Referring to the coded aperture schematic diagram (Figure 1.4), where D is the mask to detector distance and l is the 'mask overhang':

$$\theta = \tan^{-1}\left(\frac{l}{D}\right)$$

where θ is half the Fully Coded Field of View (FCOV). The FCOV corresponds to the solid angle in which incident radiation leaves a complete impression from all parts of the coded aperture mask and is typically over 50 degrees [25].

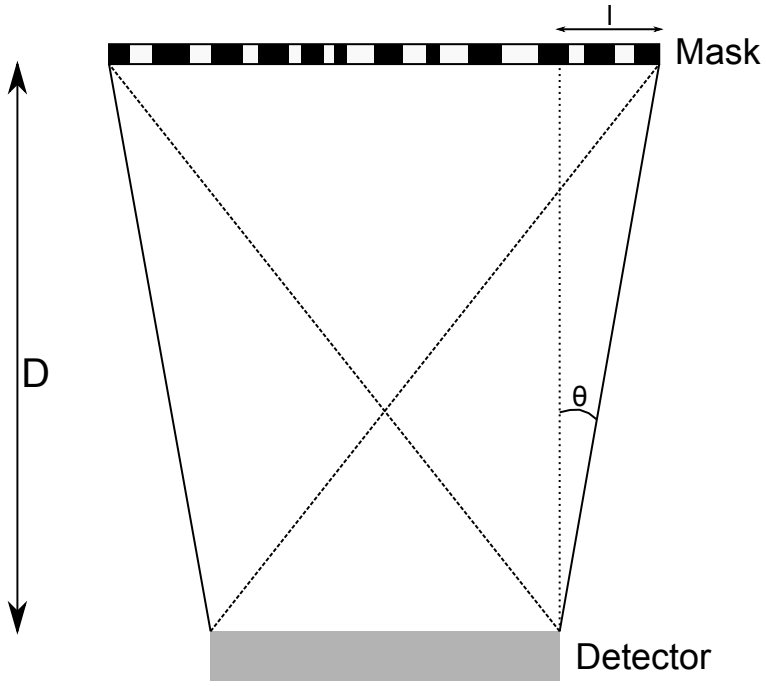

Figure 1.4: Schematic diagram of a coded aperture imaging system.

While this can be an acceptable field of view for many applications including x-ray astronomy where coded apertures are widely used, it is a limiting factor in decommissioning. Indeed in decommissioning applications coded aperture cameras tend to have FCOVs of less than 40 degrees [16, 17, 26]. A system with an improved field of view would be of great assistance and for this reason many projects are looking beyond coded apertures when approaching decommissioning research. A final drawback for the approach to decommis-

sioning is the coded aperture system's difficulties in imaging diffuse sources [23]. While it has excellent resolution when imaging point sources the size and shape of radioactive 'hot spots' in nuclear waste are likely to vary according to the waste material shape and location. As the resolution of the system is ultimately limited by the granularity of the coded aperture mask it is evident that gaining positional information without using a mask will offer the opportunity for improved image resolution, particularly when imaging diffuse sources. In addition, the positional information gained by using the mask is restricted to lateral dimensions and there are clear benefits to an approach that could determine full 3D positions of gamma emitting sources.

1.3 Thesis Outline

The Compton camera is a gamma-ray detector that can calculate energy and positional information of a radioactive source without physical collimation, which helps overcome many problems associated with the coded aperture system. The Nuclear Decommissioning Authority funded this project in association with the National Nuclear Laboratory to develop a Compton camera for use in a nuclear decommissioning environment, where the motivation for this and the limitations of current systems have been discussed. The project aims to combine a Compton camera with an optical stereoscopic camera, resulting in a system that collects detailed information of its surroundings allowing detected radioactive hotspots to be understood in relation to physical objects. This will make characterising and processing radioactive waste easier, leading to a quicker and cheaper decommissioning process. Chapter 2 will outline the necessary theory required to understand basic radiation detection and associated instrumentation. Chapter 3 will detail the two imaging systems studied in this project, comparing them to current systems used and other decommissioning projects to illustrate the potential advantages. The experimental procedures carried out to test the feasibility of this system will be explained in Chapter 4 and the implications of this work discussed in Chapter 5.

Chapter 2

Radiation Detection Principles

Compton camera systems are based on the principles of gamma-ray detection using semiconductor detectors, so a basic understanding of this is necessary to appreciate their functionality. This section will outline the principal relevant gamma-ray interactions and the basics of charge collection using semiconductor detectors. Both the theoretical and practical background to the instrumentation of such a system will be approached, while a more detailed application of these principles in the fabrication of a Compton camera will be explained in Chapter 3.

2.1 γ-ray Interactions With Matter

There are three main processes by which gamma rays can interact with matter: Photoelectric absorption, Compton scattering and pair production. They are markedly different on an atomic level and the cross section of each is governed by the energy of the incident gamma ray and the atomic number of the interaction medium. The summation of the cross section of these three interactions gives the total interaction cross section

$$\phi_{total} = \phi_{PE} + \phi_{CS} + \phi_{PP}. \tag{2.1}$$

,

where ϕ_{PE}, ϕ_{CS} and ϕ_{PP} are the cross section values from photoelectric absorption, Compton scattering and pair production respectively. Thus the linear attenuation coeffi-

cient of gamma rays through a material can be derived by multiplying the cross section by the atomic density of the material (N) in question (Nϕ) [27]. This total attenuation through germanium as a function of energy is illustrated in Figure 2.1 alongside the relative contributions from each interaction process (adapted from [28]).

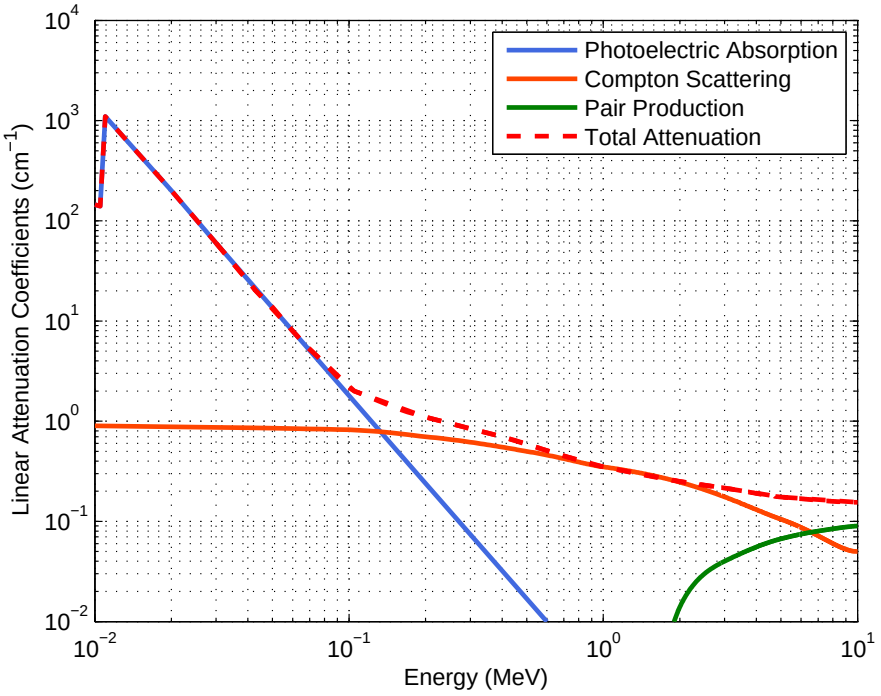

Figure 2.1: Total linear attenuation coefficients as a function of energy of gamma rays in germanium. Adapted from [28].

This highlights the regions in which the three types of interaction dominate and the energy ranges of interest for detecting such processes. Photoelectric absorption dominates from 20 - 150 keV, while Compton scattering dominates between 150 - 6000 keV and pair production above this. This supports the advantage of using a detection system that harnesses Compton scattering for the energy range of interest in this project. For incident gamma radiation with an energy range of 122 - 1408 keV interactions will predominantly occur via Compton scattering and so the ability to harness this would offer a favourable efficiency. The three processes are shown schematically in Figure 2.2 and explained below.

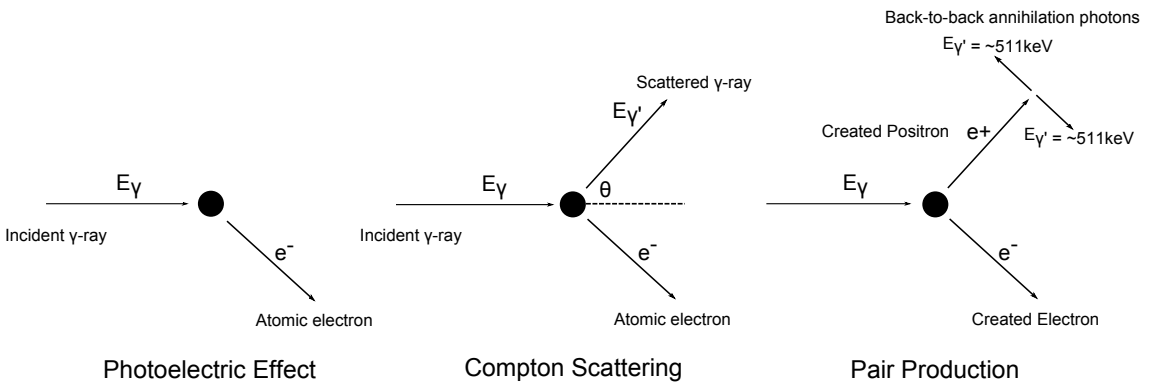

Figure 2.2: Schematic diagrams of the three main interaction processes of gamma rays with matter.

2.1.1 The Photoelectric Effect

The photoelectric effect is an interaction involving an incident gamma ray and a tightly bound electron of an atom. The gamma ray is absorbed and its energy is transferred to the electron, which is ejected from its electronic shell with kinetic energy (E_{e^-}) equal to the gamma-ray energy (E_γ) minus the binding energy of the electronic shell (E_b), shown mathematically by

$$E_{e^-} = E_\gamma - E_b. \tag{2.2}$$

The probability of such an interaction occurring is given by

$$P_\gamma = C \times \frac{Z^5}{E^{7/2}}, \tag{2.3}$$

where C is a proportionality constant, Z is the atomic number of the interacting material and E is the energy of the incident gamma ray. It can be seen that photoelectric absorption has a strong dependency on both gamma ray energy and the proton number of the interacting material. It stands to reason that highly dense materials will have greater numbers of electrons so increasing the chance of interaction with incident gamma rays [29].

2.1.2 Compton Scattering

The function of the Compton camera hinges on the Compton scattering interaction. An incident gamma ray interacts with a loosely bound electron and is scattered through an angle, imparting a fraction of its energy to the electron and continuing its trajectory. This scattering angle is dependant on the initial energy and the angular distribution of Compton scattered gamma-rays is predicted by the Klein-Nishina Formula [30], where the differential cross-section $d\theta/d\Omega$ is given by

$$\frac{d\theta}{d\Omega} = Zr_0^2 \left(\frac{1}{1+\alpha\left(1-cos\theta\right)} \right)^2 \left(\frac{1+cos^2\theta}{2} \right) \left(1 + \frac{\alpha^2\left(1-cos\theta\right)^2}{\left(1+cos^2\theta\right)\left(1+\alpha\left(1-cos\theta\right)\right)} \right), \quad (2.4)$$

where $\alpha = hv\backslash m_0 c$ and r_0 is the classical electron radius. The formula shows that with increasing energy gamma rays are preferentially forward scattered, as illustrated in Figure 2.3 (reproduced from [31]).

Crucially, the relationship between initial energy, scattered energy and scattering angle is given by the Compton scattering formula

$$E_{\gamma\prime} = \frac{E_\gamma}{1 + \frac{E_\gamma}{m_e c^2}(1-cos\theta)}, \quad (2.5)$$

where $E_{\gamma\prime}$ is the scattered gamma-ray energy, E_γ is the initial gamma-ray energy and θ is the scattering angle. It is assumed that the electron is at rest when the gamma-ray interacts, but in reality it is bound to the nucleus with an orbital momentum. This leads to a slight uncertainty on measured energy values of scattered gamma-rays and this process is known as Doppler broadening [32].

2.1.3 Pair Production

Though not as important as the other main interaction processes when considering this work, pair production is increasingly prevalent with increasing incident gamma-ray energy above 1.022 MeV and dominates above 6 MeV. It therefore must be understood to analyse

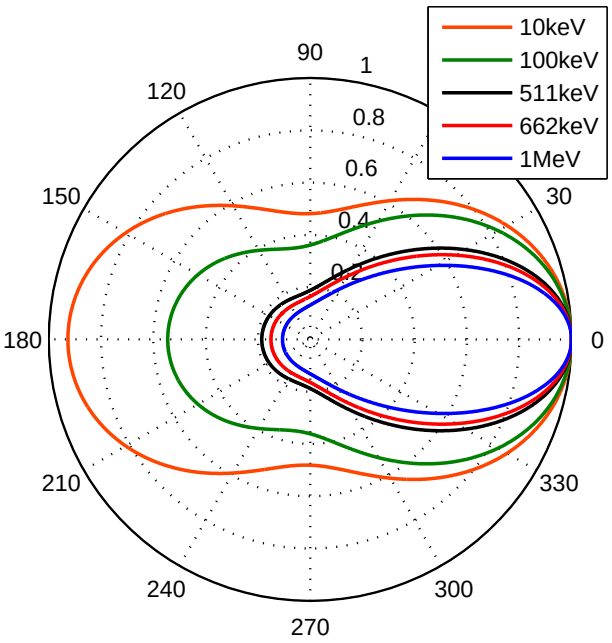

Figure 2.3: Angular distribution of Compton scattered gamma-rays for a range of typical incident energies. Radial lines show Compton scattering angles while concentric circles show the relative probabilities of Compton scattering at these angles for given gamma-ray energies. Reproduced from [31])

spectroscopy data correctly. If a gamma ray has an energy of at least twice the rest mass of an electron (2×0.511 MeV $= 1.022$ MeV) it has a chance of interacting with the Coulomb field of a nucleus. The gamma ray is converted into an electron-positron pair and each particle has a rest mass of 0.511 MeV, with the remaining gamma-ray energy shared between them as kinetic energy. The positron will travel a short distance in the material ($\ll 1$ mm) then annihilate with a free electron, emitting two 511 keV gamma rays back-to-back. This assumes the positron is at rest when annihilation occurs; annihilation cross section does increase as the positron slows down, but if the positron still has kinetic energy when annihilating it will be shared between the emitted gamma rays [27].

2.2 Acquiring Radiometric Information

The acquisition of data from these gamma-ray interaction processes requires a detection medium to create a signal from incident radiation with appropriate electronics to process this signal and extract useful information. This project uses semiconductor detectors and digital electronics which offer several improvements over alternative systems for the purpose of this task. The theory behind semiconductors and signal processing are explained in this section to highlight these advantages and provide the base knowledge required to understand Compton camera operation in Chapter 3.

2.2.1 Semiconductor Detectors

As the detector of choice in high-resolution gamma-ray spectroscopy for decades [33, 34], semiconductors are finding wide ranging applications in fields where accurate energy determination is required. They have replaced scintillators in nuclear structure physics due to their relatively efficient charge collection process that results in a far greater number of information carriers being produced for given incident radiation. Understanding the fabrication and properties of semiconductors highlights their improvements over other detection media and supports the choice of using them for this project. While the semiconductors information provided in this text is sufficient to understand this project it is by no means exhaustive and a detailed account of semiconductor theory can be found in [35].

Band Structure and Charge Carrier Generation

Semiconductors have distinct electronic characteristics that make them favourable materials for use in radiation detectors. The two most widely used pure semiconductors (comprised of a single element) are silicon and germanium, both Group IV periodic elements each has four valence electrons in its outer shell and form covalent bonds with four neighbours creating a diamond lattice structure and closing the outer electronic shells. This rigid lattice structure forms specific sets of energy states that the electrons can occupy and bound electrons are in a low energy collection of states known as the *valence band*. There is a specific energy required to break these bonds and release an electron from its lattice allowing it to move freely and contribute to the electrical conductivity of the material. Over the whole lattice this energy forms a forbidden region in which no states lie, while the energy states of those

electrons that have been released form a collection known as the *conduction band*. Each lattice site in silicon and germanium has an electron to fill it, meaning each energy state in the lattice site is filled and without external energy there will be no conduction. This is unlike the energy state structure in conductors as their occupied bands with the highest energy are only partially full. This means little energy is needed to separate these electrons from their bonds and can be represented as an overlap of the valence and conduction bands. A proportion of these electrons will always occupy conductive energy states regardless of external energy. The separation between the two energy bands is known as the bandgap and in insulators this typically exceeds 5 eV, while in semiconductors the bandgap is around 1 eV depending on the material. The band structure of these materials are shown schematically in Figure 2.4 [36].

In semiconductors, valence electrons can gain sufficient energy from incident radiation or thermal excitation to be promoted from the valence to the conduction band. This requires sufficient energy to release the electron from its lattice site and allow it to drift freely through the material. The negatively charged electron now in the conduction band leaves a vacancy in the valence band, a positively charged electron absence known as a *hole*. Both of these charges contribute to the conductivity of the material and together are known as *electon-hole (e-h) pairs*, the information carrier in semiconductor detectors. By applying an electric field across the detector these charges can be collected, the number of which is proportional to the incident radiation that formed them.

Doping and the p-n Junction

While an applied electric field would allow e-h pairs to be collected across a semiconductor the basic conditions are so unsuitable as to render it unusable as a detection medium. The conductivity created by the creation of electron-hole pairs on their own is small and the resulting signal weak. To overcome these problems a material can be doped with impurities; this is either an intentional doping or the result of all semiconductor materials containing a small impurity concentration, no matter how pure.

The impurities take up lattice spaces in the semiconductor material but have either one less or one extra electron. For the Group IV atoms of silicon and germanium, for example, doping with a Group V atom such as phosphorus causes the P atoms to have four

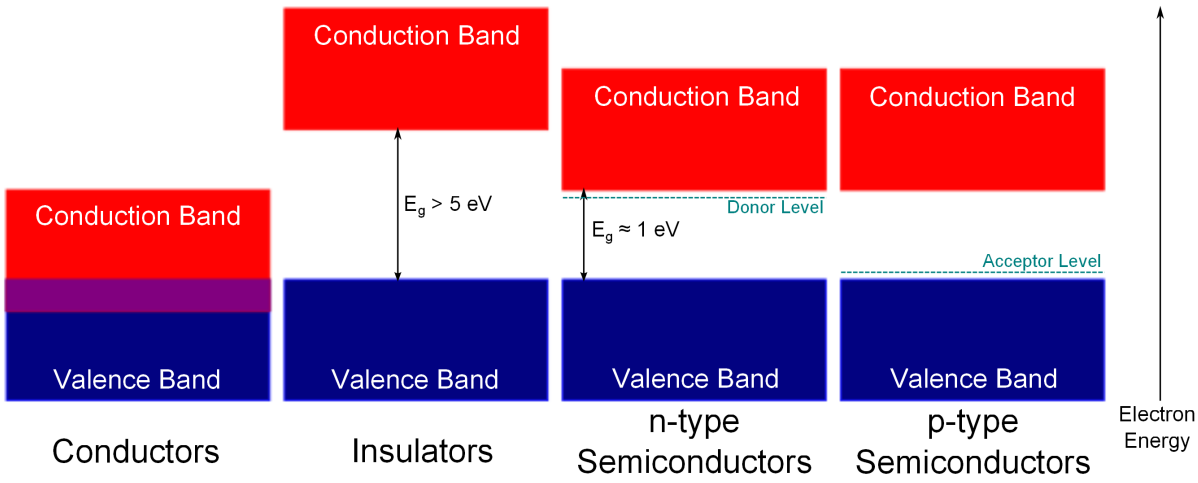

Figure 2.4: Schematic diagrams of band structure in solid materials.

covalent bonds to other atoms in the lattice but the extra electron has a weak bond with the impurity. These electrons are at energy levels above the valence band but remain weakly bound so lie below the conduction band; they occupy a *donor level* that lies just below the conduction band. These electrons typically require in the order of 0.01 eV to be promoted and the atomic thermal energy at operational temperatures is enough to introduce a large proportion of the donor electrons to the conduction band. A detector doped in this fashion is known as an *n-type* semiconductor and is shown schematically in Figure 2.4. The number of donor electrons will far outweigh the number of intrinsic charge carriers and it can be well approximated that the conductivity of a n-type semiconductor is entirely due to electrons. Alternatively, doping with a group III atom such as boron means the dopant atom has one less electron than those in the material. In a lattice space the dopant has four neighbours but three electrons meaning one of its covalent bonds will be unsaturated. This unsaturated bond leaves a vacancy that can be filled by a free electron but it is a weaker bond than

those between the pure semiconductor atoms. This means electrons bound this way occupy energy levels slightly above the valence band in the forbidden region, known as *acceptor levels*. Electrons that are thermally promoted from the valence band to the conduction band can fill these acceptor level vacancies, leaving behind holes in the valence band. These are known as *p-type semiconductors* and conversely to n-type the acceptor holes far outnumber the intrinsic electrons, meaning to a good approximation the holes completely account for the conductivity of p-type semiconductors [37]. The p-type semiconductor is also depicted in Figure 2.4. It is also worth noting that when the donor electrons and acceptor holes are liberated charge neutrality is maintained in their respective materials. When these charge carriers are released they leave behind ionized donor impurites that balance the charge, though they remain fixed in their lattice positions and thus cannot contribute to the conductivity of the material [27].

It is the use of both of these doped semiconductor types together that gives rise to a useful detection medium. Bringing an n-type and p-type semiconductor into contact on an interatomic level causes diffusion of their charge carriers, electrons and holes respectively, across this contact. There will be substantial recombination of these charge carriers as the free electrons fill the vacancies. The ionized donor impurities left behind will build up a charge as this occurs that opposes the migration of further charge carriers; there will be a positive charge build up in the n-type semiconductor that limits electron diffusion and a negative build up that limits hole diffusion in the p-type. There is now a region in which it can be approximated there are no free charge carriers known as the *depletion region*, adjoined by two regions of oppositely polarised space. This establishes an electric field across the depletion region, due to the change in electric potential from the p-side to the n-side. The p-n junction band structure can be seen in Figure 2.5. The Fermi level is controlled by the acceptor and donor levels but must be constant in thermal equilibrium contact, causing a shift in the energy bands with a transition between the two types across the depletion region.

Reverse Biasing

The pn junction has created a region in which there are few free charge carriers and an electric field. Incident radiation that creates charge carriers in this field can be easily

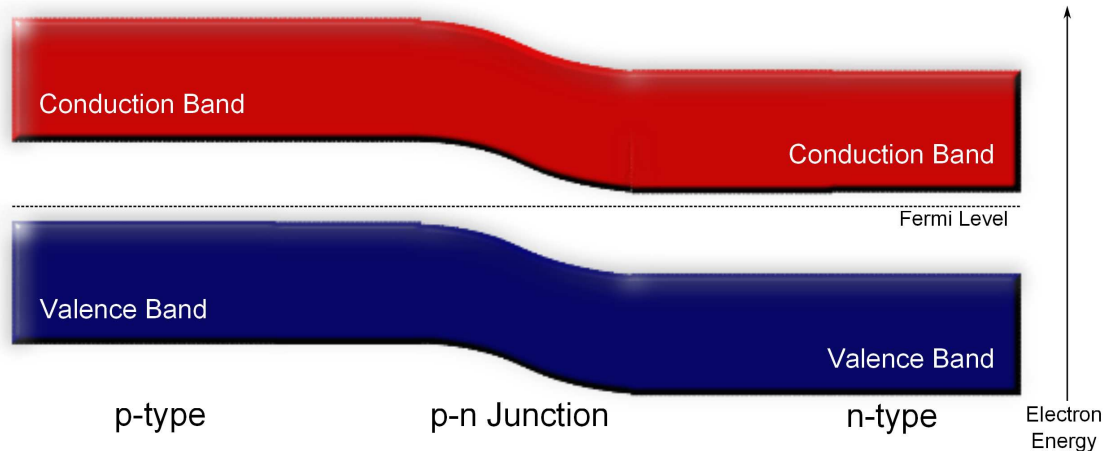

Figure 2.5: Schematic diagram of the band structure across a pn junction.

collected as electrons and holes will be moved toward their respective regions. This would function as a radiation detector, however its performance would be poor. The depletion region which represents the active volume of the detector is small (in the order of 1 μm) while the electric field is weak and inhomogeneous leading to incomplete charge collection as charge carriers frequently recombine. This problem is rectified by applying an external voltage across the detector that accentuates the electric field occurring naturally across the pn junction. This is achieved by applying a negative voltage to the p side of the detector with respect to the n side and is known as *reverse biasing* due to the reverse applied voltage when compared to the standard function of a pn junction as a diode. The increased potential causes a stronger opposition to charge carrier diffusion, leading to an increase in depletion region width. If the bias voltage is high enough the depletion region can extend far enough to cover the volume of the detector which is then said to be fully depleted. Further voltage increases past this point will increase the homogeneity of the electric field and reduce charge trapping. The width of the depletion region can be calculated using the equation

$$d \approx \left[\frac{2\epsilon V_0}{eN}\right]^{1/2}, \tag{2.6}$$

where ϵ is the dielectric constant, V_0 the applied reverse bias and N the dopant concentration on the junction side that has the lowest dopant level. It is apparent that the

depletion width is governed by the applied voltage and dopant concentration. Voltages are typically in the order of 100 V/mm [38] and higher voltages can cause damaging breakdowns of the pn junction, so purity of detection material is vital to fabricate large scale semiconductor detectors.

2.2.2 Hyperpure Germanium

This project specifically employs hyperpure germanium (HPGe) semiconductor detectors. HPGe refers to the method by which the germanium is treated to significantly reduce the impurity concentration to the order of 10^9 atoms/cm^3 [27]. This is a necessary process to produce practical depletion depths as net impurity concentration has a large effect on achievable depths. Their main advantage over other semiconductor types such as silicon is its purity allows depletion regions of much greater width. This in turn allows gamma rays of higher energies to be stopped which is necessary to detect high-energy gamma ray emitting sources such as ^{60}Co. Germanium has many other properties that make it advantageous to this project and this section will outline these.

Germanium Properties

Germanium is a semiconducting material that combines good efficiency with excellent energy resolution to create a favourable gamma ray radiation detection material. It has an ionization energy of ∼3 eV meaning many charge carriers are produced for a given incident radiation and statistical fluctuations are reduced leading to excellent energy resolution. Compared to scintillators such as Sodium Iodide that require ∼100 eV per information carrier it is clear to see why Germanium detectors give the best energy resolution of any known material. Sodium iodide detectors have an energy resolution of ∼8% while at 1.33 MeV a hyperpure germanium detector has a resolution of ∼2 keV or 0.15%. HPGe must be cooled to 77 K to reduce the thermal leakage current sufficiently and keep noise to a minimum. This is only required while the detector is operational, the device may be warmed up when not in use. This presents a significant advantage over lithium ion drifting as a process for reducing the net impurity concentration, as lithium drifted germanium detectors must remain permanently cooled [39]. The properties of Germanium are listed in Table 2.1 [27]:

Atomic Number A	32
Atomic Weight Z	72.6
Atoms	4.4×10^{22} cm^{-3}
Density	5.32 gcm^{-3}
Crystal Structure	diamond (FCC)
Dielectric Constant η_r	16.2
Intrinsic carrier concentration (300K)	2.2×10^{13} cm^{-3}
Intrinsic Resistivity	46 Ωcm
Energy Gap (300 K)	0.67 eV
Energy Gap (0 K)	0.75 eV
Ionization Energy (77 K) η_{pair}	2.96 eV
Fano Factor (77 K)	0.08
Electron Mobility (300 K)	3900 cm^{2}Vs
Hole Mobility (300 K)	1900 cm^{2}Vs
Lattice Constant (a)	567.75 pm

Table 2.1: The electronic properties of germanium [27].

Lattice Properties

Germanium has a Face Centered Cubic (FCC) diamond structure. While this is a repeated structure throughout the crystal the orientation with regards to the electric field is of great importance. This changes depending on the lattice axis along which the crystal is cut. The three possible planes along which Germanium can be cut are shown in Figure 2.6 along with the respective miller indices of each.

When electron-hole pairs are created in the detector the velocity with which they move under the applied electric field is known as the *drift velocity*. The drift velocity is initially linearly proportional to the electric field strength but will saturate at significantly high electric fields ($\sim 10^7$ cm/s for 77 K cooled germanium with an applied field of $\sim 10^4$ V/cm). This is dependant on both the temperature and crystal orientation. The orientation of the crystal lattice governs the distance between atoms along the electric field lines. The shorter this distance the greater the probability of interaction between atoms and charge

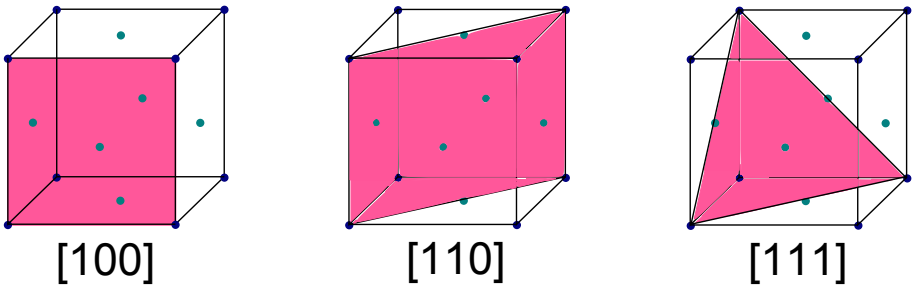

Figure 2.6: Diagrams of the Face Centered Cubic lattice structure of germanium. The three possible crystal orientations are shown with their respective miller indices below.

carriers. While these will be elastic scattering the effect is to reduce the drift velocity in the direction of motion from the electric field. Electron drift velocities as a function of electric field strengths are shown for each crystal orientation in Figure 2.7 [40]. Electrons travel faster than holes due to the nature of their transport through the material; holes move through the lattice by the continuous displacement of bound electrons into the free vacancy which is a longer process than the free movement of the electron. This gives hole saturation velocities of 9.5×10^6 [41], but while electrons velocities saturate under electric fields of the order of 10^3 V/cm, holes require a significantly higher field of the order of 10^4 V/cm. This means in an electric field of 2000 V/cm, electrons will travel between 3 and 4 times faster than their respective holes [42]. The drift velocity can be expressed in terms of electric field strength by

$$V_d = \mu E, \tag{2.7}$$

where μ is the charge carrier mobility that is dependant on charge carrier, material and material temperature. E is the electric field strength.

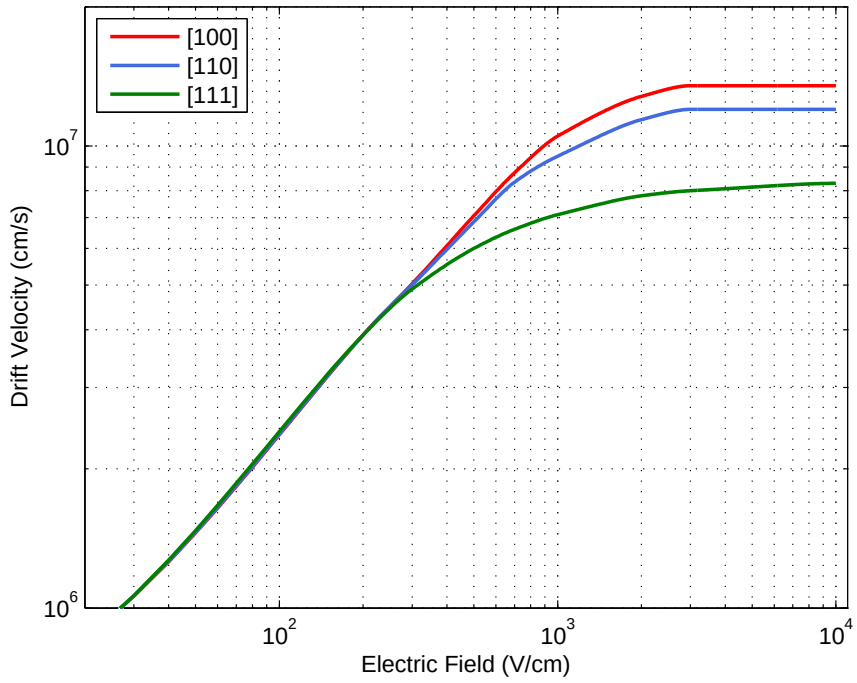

Figure 2.7: Drift velocity as a function of electric field strength for charge carriers in three crystal orientations of germanium

2.2.3 Signal Generation in a Planar Detector

This project utilises planar HPGe semiconductor detectors and the process of generating signals from incident radiation is critical to optimising the system. When gamma radiation interacts by any of the three main processes it imparts some energy to an electron which subsequently interacts via the Coulomb force with nearby bound electrons. This promotes a number of these electrons to the conduction band creating a cloud of charge carriers proportional to the imparted energy. It thus stands to reason that

$$Q_s = \frac{E}{E_i} e, \tag{2.8}$$

where Q_s is the signal charge, E the total absorbed energy, E_i the energy required to make an e-h pair and e the electronic charge. The charge carriers will drift under the influence of the applied electric field, electrons swept towards the n-side of the pn junction

and holes to the p side. For a planar detector that is biased beyond its depletion voltage, the electric field is given by

$$|E(x)| = \frac{2V_d}{d}\left(1 - \frac{x}{d}\right) + \frac{V - V_d}{d}, \tag{2.9}$$

where x is the charge carrier point in depth, V the bias voltage, d the detector thickness and V_d the drift velocity [35]. Charge carriers will be collected at electrodes on either side of the crystal, typically blocking electrodes that do not replace the collected charge carriers to reduce leakage current. It is not the collection of electrons or holes, rather their movement through the material that generates a signal. As the carriers are charged they have a Coulomb field that extends past the electrodes. Their movement changes the gradient of this field over time and it is this that generates a signal at the electrodes. The current induced at a particular point in the detector can be solved using the Shockley-Ramo theorem. This shows that the current i induced on an electrode by a moving point charge is

$$i = qv \cdot E_0(x), \tag{2.10}$$

where v is the velocity of charge q and $E_0(x)$ the electric field at point x [43].

2.2.4 The Weighting Field

The previous section explains the signal generated by charge carriers at the electrodes between which they are generated. From these signals energy and time information can be extracted as well as basic positional information as it is known the interaction occurred between these electrodes. In many detector systems (and indeed those used in this project) there is not one but many electrodes in strips on either side of the detector to improve raw positional information. This provides further advantages which can be deduced by considering the Schockley-Ramo Theorem [43]. Equation 2.10 gives the induced current at a particular point due to the applied electric field. The same precept can be represented by the equation

$$Q = q\Delta\varphi_0, \tag{2.11}$$

where Q is the total charge induced on the electrode, q is the charge of the carrier and φ_0 is the *weighting potential*. While the electric potential is actually due to the Coulomb field of the charge carriers and its magnitude at the position of the electrodes, the weighting potential is an artificial inversion of this where the field is considered to originate from the electrode itself and the magnitude of the weighting potential depends on the position of the charge carriers with respect to it. This field is known as the *weighting field* and can be found by taking the gradient of the weighting potential. The weighting values are often used as they provide a straightforward way of determining the proportion of total electric potential at given points in a detector. This allows pulse shapes of charge collection over time to be predicted.

Figure 2.8 (reproduced from [27]) shows a diagram of a detector with a planar electrode on one side and twenty five pixel electrodes on the other. The graph on the right shows weighting potential as a function of position for both electrodes. As the weighting potential is governed by the magnitude of the Coulomb field of the charge carriers extended over the electrode it stands to reason it will increase linearly as the charge carriers approach the planar electrode. The pixel electrode covers a smaller solid angle with respect to charge carrier position so the increase in weighting potential is small as they approach the electrode with a huge increase when they are very close to it. This is known as the *small pixel effect* and it increases as the electrode area decreases. It is apparent that the weighting potential with respect to the pixel electrode as a function of time will be markedly different depending on the interaction position. An interaction close to T will pass through a large potential gradient change initially which will reduce as the first charge carrier is collected at T and the second travels ever further away from it. There will be an opposing effect for an interaction near 0. Consequently study of the charge collection process as a function of time can yield the interaction depth; this is known as *Pulse Shape Analysis (PSA)* and will be illustrated experimentally in Chapter 4.

The Coulomb field of charge carriers is not limited to the electrodes between which the interaction occurred but extends over all the electrodes of the detector. This means

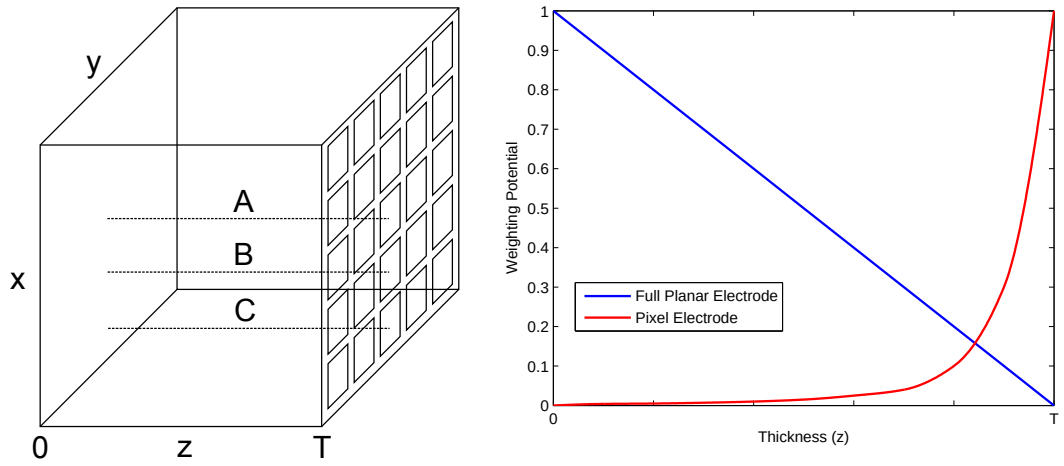

Figure 2.8: A schematic diagram of a semiconductor detector of dimensions x,y and T (left) alongside a graph of weighting potential of a pixel electrode as a function of detector thickness (right). The detector has a single planar electrode on the left side and 25 pixel electrodes on the right, while A and B show charge carrier paths at two different x-y positions in the detector [27].

the weighting potential with respect to other pixel electrodes can be ascertained which also has a bearing on interaction position. Figure 2.9 (reproduced from [27]) shows the weighting potential on a pixel electrode adjacent to the pixel parallel to the interaction (B is the position in x-y of the adjacent pixel and A the pixel of interest with respect to Figure 2.8). C shows the weighting potential on an electrode two pixels from the pixel of interest. It is worth noting that Figure 2.9 is a factor of ten smaller than Figure 2.8 (right) as the weighting potential with respect to these electrodes is far smaller. As can be seen the weighting potential is 0 at both sides of the detector for adjacent pixels as the magnitude of the Coulomb field from charge carriers at these positions is 0, which means the net charge is zero and integrating over the charge collection time will yield no signal. However while the charge carriers are moving a weighting potential will be induced, with a magnitude dependent on the proximity of the electrode to the charge carriers. Because the pixel at B is closer to the interaction than pixel C the charge induced at this electrode is greater; these are known as *image charges* and their magnitudes are dependent on the lateral position of the gamma-ray interactions. This means PSA is not restricted to the charge collecting electrodes as studying image charges can also improve interaction position

resolution and this will also be demonstrated experimentally in Chapter 4.

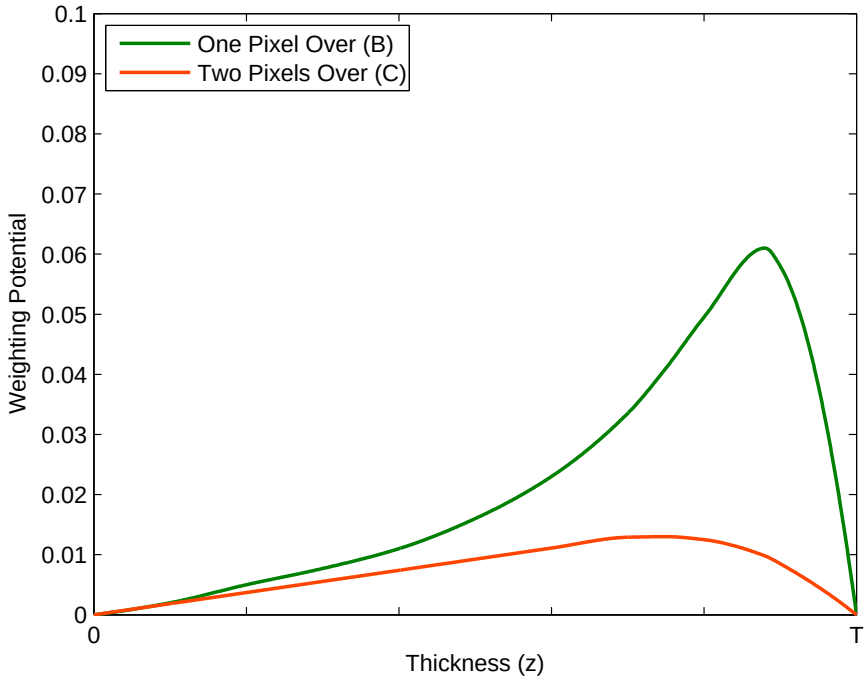

Figure 2.9: Weighting potentials as a function of detector thickness for pixel electrodes near the electrode parallel to a gamma-ray interaction, as shown in Figure 2.8 [27].

2.2.5 The Preamplifier

The current induced on the electrodes by the movement of charge carriers is detectable but relatively weak. This must be converted into an amplified voltage pulse while limiting signal degradation and pulse width. This process is handled by the preamplifier and its design must be carefully matched to compliment the detector it is used with. Common types are the current-sensitive, voltage-sensitive and charge-sensitive units where current-sensitive preamplifiers are only suitable for devices which produce charge pulses of fixed rise times such as scintillators, making them unsuitable for this project [44]. Voltage-sensitive preamplifiers amplify the input voltage which arises due to the intrinsic capacitance of the detector, so it is vital this remains constant for accurate signal measurement. Small changes in temperature can affect the capacitance, making signals amplified from semiconductors

this way of poor quality. These limitations can be overcome using the charge-sensitive preamplifier, the circuit diagram for which is shown in Figure 2.10 [45]. Note this is a circuit diagram of the resistive-feedback charge-sensitive preamplifier and there are other types with differing electronics.

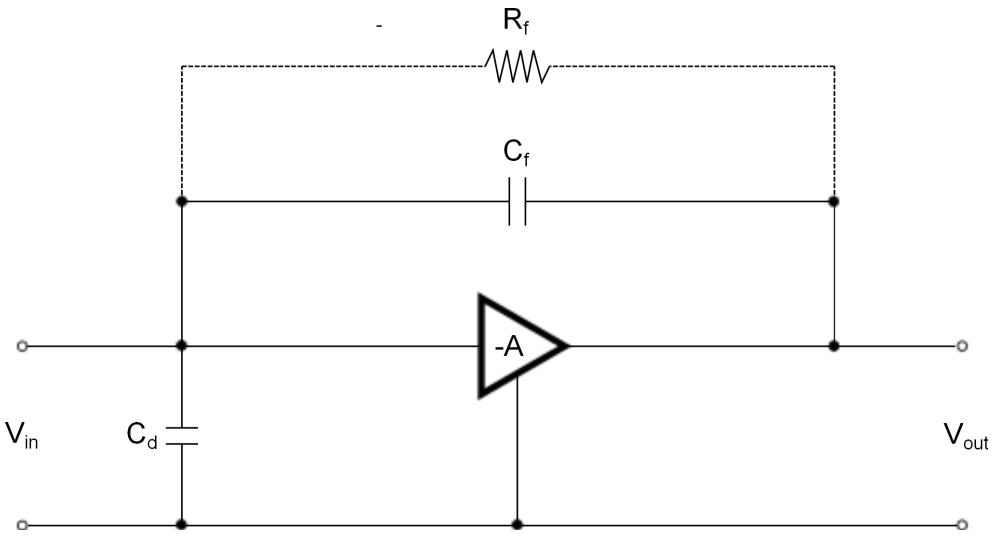

Figure 2.10: Circuit diagram of the charge-sensitive preamplifier [45].

The resistive-feedback charge-sensitive preamplifier provides the stable and linear response required for high-resolution gamma spectroscopy. Unlike the voltage-sensitive type that directly amplifies any input voltage, this device couples the detector signal to a capacitor (C_d) that is in turn integrated on another capacitor in a feedback loop (C_f). The coupling capacitor separates the feedback capacitor from the current pulse nullifying the effect of the leakage current and thus changes in detector capacitance. The feedback capacitor is in an open gain loop that greatly amplifies the signal though still in proportion with the coupling capacitance. The feedback resistor (R_f) slows the discharge of the feedback capacitor creating the 'tail' of the preamplifier output pulse. This is necessary as proportionality between input and output only holds if the input pulse duration is less than the preamplifier time constant ($R_f C_f$).

The output voltage from the charge-sensitive preamplifier is given by

$$V_{\text{out}} = \frac{Q}{C_{\text{f}}}, \tag{2.12}$$

and the decay time constant τ_{f} of the output pulse is

$$\tau_{\mathrm{f}} = R_{\mathrm{f}} C_{\mathrm{f}}. \tag{2.13}$$

The shaping of the pulse is controlled by the resistive-feedback loop and the decay time of the pulse is crucial to ensure the noise of the system is minimised and an optimal signal-to-noise ratio is achieved. There are current and voltage noise contributions from the leakage current and capacitance of the detector respectively. A long shaping time means more leakage current is measured and the greater the noise contribution. However a shorter shaping time causes the leakage current to build up on the capacitance without dissipation, leading to increased noise. This leads to an optimal shaping time where the noise contribution from both sources is minimised. There is also a noise component unrelated to shaping time as a result of trapping processes in the detector, referred to as $1/f$ noise as it is related to the frequency range of the preamplifier. The noise contributions are illustrated in Figure 2.11 as a function of shaping time, reproduced from [35].

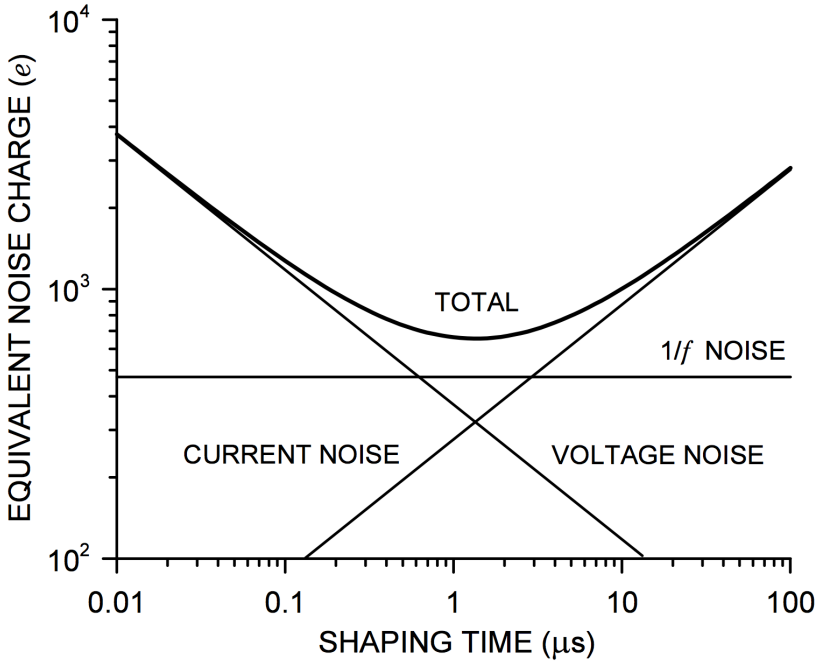

Figure 2.11: Noise contributions as a function of shaping time. Reproduced from [35].

2.3 Limiting Factors of Radiometric Information Quality

The success of this project depends on the optimisation of the detectors used to give the best Compton image quality. This section highlights those factors inherent to the detectors that impact the quality of measured radiometric information and any steps that may be taken to improve them. Note that these factors are presented for a single detector; due to the dual detector nature of the Compton camera it has an atypical response compared with single detector systems and this will be measured experimentally in Chapter 4. As the Compton camera used in this project is comprised of two planar detectors it is necessary to understand the response of a single detector to understand that of the whole system.

2.3.1 Energy Resolution

The energy resolution of HPGe detectors for gamma rays is the best currently achievable by any material often making them the first choice for projects that require accurate energy information. As aforementioned this is due to the relatively small amount of energy required to liberate charge carriers from the germanium crystal lattice. Table 2.2 shows typical energies required to create information carriers for commonly used semiconductor materials and the widely used scintillator material sodium iodide [46, 47].

Material	Energy Required to Create Information Carriers at 77K (eV)
Germanium (Ge)	2.96
Silicon (Si)	3.76
Cadmium Zinc Telluride (CdZnTe)	5
Sodium Iodide (NaI)[1]	∼100

Table 2.2: Typical information carrier production energies for commonly used gamma-ray detection materials [46, 47].

The energy resolution is determined by three main factors: Statistical fluctuations in ionization, the effects due to incomplete charge collection and electronic noise induced from system components [48]. If the Full Width at Half Maximum (FWHM) values of an energy peak due to these conditions are taken to be W_D, W_X and W_E respectively the total FWHM of this peak can be written as

$$W_T^2 = W_D^2 + W_X^2 + W_E^2. \tag{2.14}$$

Statistical broadening occurs due to small variations in temperature which in turn cause small variations in the bandgap energy. It can be calculated by

$$W_D = 2.35\sqrt{F\epsilon\ E}, \tag{2.15}$$

where ϵ is the energy required to liberate an e-h pair, E is the energy of the incident radiation and F a correctional value known as the *Fano Factor*. The Fano factor is the term that accounts for the variation in the energy required to create an electron-hole pair and is notoriously hard to measure with a large spread of published values [49]. The effect of incomplete charge collection W_X is governed by the size and electric field of the detector. It can be estimated for a given detector by collecting FWHM measurements as a function of applied bias voltage. W_E represents peak broadening from each component of the electronic chain and so varies with components used. It can be tested using a pulser, a generator of pulses of specific amplitude and time, while recording changes in recorded peak width. Assuming the system is grounded correctly and there are no unnecessary components used there will always be a level of intrinsic electronic signal degradation. Figure 2.12 shows FWHM as a function of energy for each energy resolution contribution for an 86 cm^3 coaxial HPGe detector (reproduced from [50]).

It is also helpful to consider the effect of thermally generated charge carriers on the resulting energy resolution. The probability per unit time of an electron-hole pair being thermally generated can be calculated using the relationship

[1]While the energy required to produce a scintillation photon is 26 eV around 20 - 30% of these are converted to photoelectrodes at the photocathode. This is known as the *quantum efficiency* and means on average it takes four times the energy to produce an information carrier.

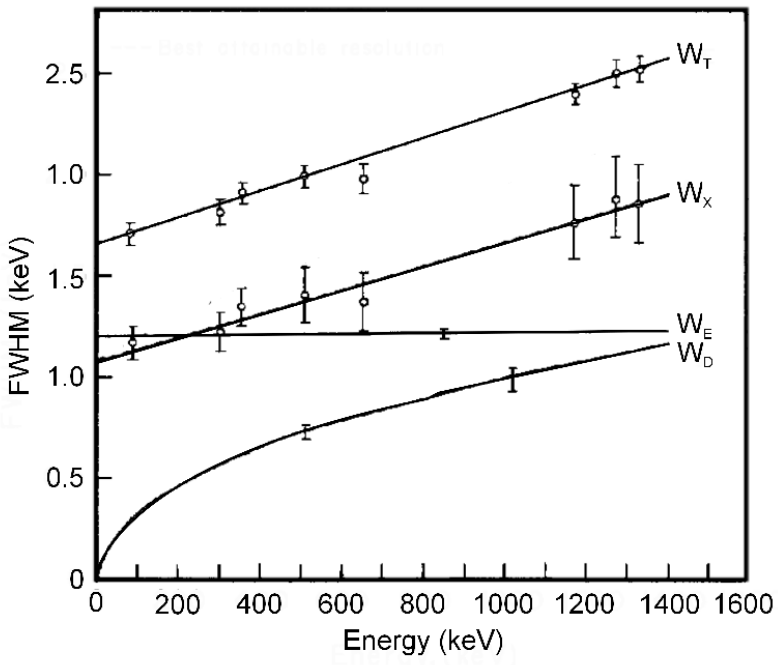

Figure 2.12: FWHM as a function of energy for an 86 cm^2 coaxial HPGe detector. W_T shows the total FWHM while W_D, W_X and W_E are the contributions from statistical broadening, incomplete charge collection and electronic noise respectively. Reproduced from [50].

$$p(T) = CT^{3/2} exp\left(-\frac{E_g}{2kT}\right), \tag{2.16}$$

where T = absolute temperature, E_g = bandgap energy, k = Boltzmann constant and C = proportionality constant. It can be seen that while a small bandgap energy allows e-h pairs to be created from incident radiation it also allows thermal pairs to be more frequently created independent of any incident radiation. These will contribute to a *leakage current* that deteriorates the energy resolution of the detector. In the case of germanium that has a bandgap energy of around 0.645 eV at room temperature, it is important to reduce this leakage current by cooling the detector to a suitable temperature[2] [27].

[2]The operational temperature of Germanium semiconductor detectors is 77 K, cooled mechanically or using liquid Nitrogen.

2.3.2 Efficiency

Efficiency is essentially a measure of the number of detected gamma rays compared to the number emitted from a gamma-ray source and is typically represented as a fraction or percentage. Displayed mathematically this is

$$\text{Efficiency} = \frac{\gamma_{Detected}}{\gamma_{Emitted}}. \tag{2.17}$$

It is a critical parameter that determines how long it takes to accumulate statistics and ensuring high detection efficiency is an important part of detector optimisation. The absolute efficiency of a detector is dependant on the material, size and position of the detector and the energy and distance to the source of the measured gamma rays. It can be obtained using Equation 2.17 which can be shown more practically for the case of gamma-ray spectroscopy as

$$\text{Absolute Efficiency} = \frac{\gamma_{detected}}{LT(s) \times A_{\gamma} \times P_{\gamma}}, \tag{2.18}$$

where LT is the 'live time' the detector has been counting for (omitting 'dead time' when the system is unable to detect incoming gamma-rays), A_{γ} is the source activity and P_{γ} the branching ratio of the measured gamma ray. As absolute efficiency is dependent on so many parameters it can be useful to break it down into *geometric efficiency* and *intrinsic efficiency*. The former is the fraction of emitted gamma rays that are incident on the detector material while the latter is the fraction of incident gamma rays that are detected. Industrially, detector efficiency is quoted relative to a 3" $\times$ 3" coaxial Sodium Iodide scintillation detector measuring gamma rays from a ^{60}Co source at a distance of 25 cm. A fixed-time measurement is taken with the detector in the same setup as that of the NaI detector and the efficiency measured using to the 1332 keV ^{60}Co peak. This is known as *relative efficiency* and can be calculated by

$$\text{Relative Efficiency} = \frac{\gamma_{Detected}}{\gamma_{Emitted}} / 1.24 \times 10^{-3}, \tag{2.19}$$

where 1.24×10^{-3} is the *Absolute Efficiency* of the 3" $\times$ 3" NaI detector at the same

position [51]. A final efficiency parameter of interest to this project is the *absolute photopeak efficiency*, which adds the condition that only events in the photopeak of interest are considered to be detected events. This is imperative in imaging systems where only photopeak events are considered useful.

Chapter 3

Imaging Systems

This project aims to fuse two imaging modalities that would allow one system to combine radiometric and stereoscopic images. To understand the system as a whole it is a prerequisite that the modalities are understood separately. This chapter will outline the theory, operation and advantages of both systems. This will be followed by detailed descriptions of the specific detectors used for both imaging modalities in this project.

3.1 Glossary of Experimental Terms

In order to accurately describe the imaging systems and experiments a number of words are used to succinctly reference complex terms. These are detailed here:

- **Event** - A set of energy and position information from the detector system in a single sample time. This would typically consist of the interactions of a single gamma-ray, but if two (or more) gamma-rays interact in a timeframe such that they cannot be distinguished, this is also classed as a single event.
- **Gate** - A set of conditions imposed on events to select only those of interest. A typical example would be an energy gate, where only interactions that deposit a certain energy are selected.
- **Depth, z** - The axis perpendicular to the crystals of the Compton camera.
- **Standoff distance** - The distance from the scatterer crystal to the radioactive source along the axis perpendicular to the crystal face.

- **Voxel** - Strictly speaking, a voxel is one of an array of discrete elements into which a three dimensional space is divided. In this case, the detectors are divided into spaces that are uniquely covered by two electrodes. As there are two sets of 12 electrodes on each side of the detectors arranged orthogonally to each other this creates 144 voxels in each detector.

- **Fold** - The number of interactions measured by unique channels on one detector face from a single event. This is commonly written as Fold #, where # specifies the number of interactions. This can be extended to Fold(#,#,#,#) to show fold values for the four detector faces of both detectors.

3.2 Compton Cameras

The Compton camera is not a new concept but one that has benefited from increasing detector quality, electronic improvements and computer advancement. The idea was originally developed for use in astronomical imaging but proposed for use in nuclear physics in the 1970s [52]. It harnesses position and energy sensitive detectors to yield such information about radioactive sources. There has been significant research in this field and a range of configurations exist, from silicon arrays [53] to CZT crystals [54]. They have found applications in medical imaging [55], homeland security [56] and beyond. The Compton camera system used in this project is comprised of two HPGe planar detectors coupled with digital electronics and subsequent background information will be based on this setup.

3.2.1 Compton Camera Theory

The Compton camera system presents a solution to the limitations of mechanical collimation used in other gamma-ray imagers such as coded aperture systems. As shown in Chapter 1, coded aperture systems gain their positional information by placing a coded grid over the detection medium but this causes a huge drop in sensitivity, limits the operational energy range and restricts the detection field of view. The Compton camera gains positional information by using gamma rays emitted from the source that Compton scatter in an initial detector and are photoelectrically absorbed in a second detector (commonly known as the *scatterer* and *absorber* respectively). A schematic diagram of a Compton camera

comprised of two planar detectors is shown in Figure 3.1 with such an event highlighted. In the figure E_1 and E_2 are the energies deposited in the scatterer and absorber. This makes it simple to recover the energy of the source, as

$$E_\gamma = E_1 + E_2 \tag{3.1}$$

where E_γ is the source energy.

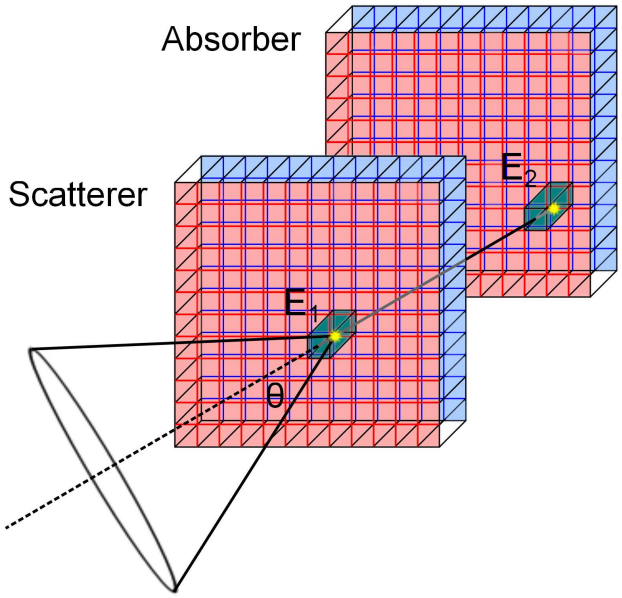

Figure 3.1: Schematic diagram of a Compton camera. A gamma ray is shown Compton scattering in the scatterer depositing energy E_1 and being absorbed in the absorber depositing energy E_2, back projecting a cone of solid angle θ.

Less straightforward is the ascertainment of source position; by using the Compton scattering formula (Equation 2.5) and the energies of the original and Compton scattered gamma ray the angle through which it was scattered θ can be calculated. This angle does not reveal from which direction the scatter occurred, so instead of a single line a cone is back projected from the scatterer on which the source of the gamma ray must lie. There is research into tracking the electron that is ejected in the Compton scattering process to

yield improved information on the direction of the incoming gamma ray through momentum conservation [57, 58]. Unfortunately this requires highly segmented detectors with small active volumes in which the ejected electron path length is long enough to track across multiple detector elements; this approach was not suitable for this project. A single back projected cone as shown in Figure 3.1 is of little use as the source can be located on any part of it. It is through collecting multiple events that these cones overlap and each gamma-ray emitted from the source should lead to a back projected cone that intersects at a certain point. A source image is thus built up from a collection of these intersecting cones. As these cones are backprojected in 3D space the resulting image is inherently 3D.

3.2.2 Project Compton Camera System

The system chosen for this project was built following previous Compton camera research at the University of Liverpool. Harkness *et al* developed ProSPECTus, a Compton camera detector head that allowed SPECT imaging to be carried out simultaneously with MRI [55]. Preliminary measurements for the ProSPECTus system utilized two planar HPGe detectors previously used in the SmartPET system, a project applying the advantages of semiconductors, digital electronics and Pulse Shape Analysis to small animal PET imaging [59]. The SmartPET detectors are two Double Sided Germanium Strip Detectors (DSGSD) the n-type detector was reused as the absorber detector in this project. The crystals have dimensions of 74 mm × 74 mm × 20 mm and an active volume of 60 mm × 60 mm × 20 mm (the extra germanium acts as a guard ring). They are housed in the centre of a 50 mm wide (1 mm thick) aluminium casing with a 15 mm gap between the detector and each side of the casing. The crystal was cut such that the <100> crystal axis is parallel to depth and there is a 5% variation in the 5×10^9 atoms/cm^3 impurity concentration along this axis. There are 12 AC contacts (AC01-12) and 12 DC (DC01-12) contacts on opposite sides of the detector both 5mm in width and 0.3 μm and 50 μm thick respectively, with the sets arranged orthogonally. This provides electronic segmentation of the crystal, creating 144 voxels with dimensions 5 mm × 5 mm × 20 mm that represent the raw position resolution of the detector. It is fully depleted at -1300 V and has an operational voltage of -1800 V applied to the AC contacts, while the DC contacts are grounded. Both detectors are connected to a LN_2 dewar via a cryostat that facilitates cooling to 77K operational

temperature. The preamplifiers have a gain of 300 mV/MeV and a rise time of 30 ns as defined from 10% to 90% of pulse height [60].

The p-type crystal was removed from the second detector and replaced with another p-type HPGe crystal but of dimensions 74 × 74 × 5 mm. This was due to the fact that while SmartPET was a project specifically designed for detecting 511 keV gamma-rays, this project needs a much wider operational energy range as explained in Chapter 1. A thinner scatterer crystal allows a higher transmission of low energy gamma-rays, whereas a thicker crystal has a much higher chance of completely absorbing the incident gamma ray so it cannot be used as an imaging event (in this case; it is possible to backproject cones from two interactions in the same crystal [61] but the closeness of the interactions leads to larger angular uncertainties so this approach has been avoided in this project). In practice, the casing, electrodes, cooling and preamplifiers are the same as the SmartPET set up but there are 144 voxels of 5 × 5 × 5 mm and the system has a depletion voltage of around -150 V and an operational voltage of -300 V. The crystal is only 5 mm thick but the gap between the AC side of the crystal and the casing remains 15 mm, meaning the gap between the DC side and the casing is now 30 mm. During experimental measurements the DC12 electrode of this detector was not instrumented as it had to be grounded to eliminate ringing noise in the other channels. This ringing was a result of signal reflections in the preamplifiers due to a manufacturing error, where a part of the cryostat wasn't earthed correctly. Figure 3.2 shows the new detector with the preamplifier casing off so the preamplifiers are visible. Experimental images of the Compton camera system as a whole are shown in Chapter 4.

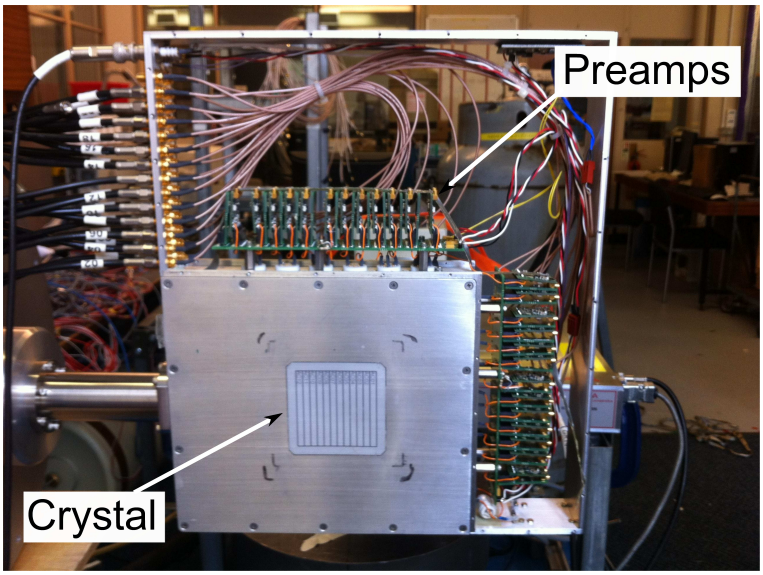

Figure 3.2: Image of the scatterer detector used in this Compton camera project. The absorber has an identical appearance as its thicker crystal is inside the vacuum sealed casing.

3.3 Stereoscopic Cameras

Stereoscopy is the method of gaining 3D information from two or more 2D images. It is the system by which the human brain perceives depth and the artificial mimicry of our natural depth extraction algorithms has been a keen area of research for over thirty years [62]. Stereo vision is of particular interest in the field of robotics to allow depth information to be collected when people cannot directly view an environment themselves; this has wide ranging applications from industrial inspection [63] to planetary exploration [64]. This project aims to combine the radiometric information from a Compton camera with the 3D information of surroundings produced by a stereoscopic camera, allowing such a fused device to be operated robotically in high radiation environments and in real-time. There are several ongoing projects aiming to combine visual and radiometric data, including the CdZnTe based Polaris system developed at the University of Michigan [65] and a Si/Ge system developed at UC Berkeley [56]. These gain their depth information using *contour imaging* however, a technique that employs a pulsed laser system to ascertain object distance by measuring the time between pulses and measured reflections [66]. This system has limitations when performing image segmentation of the scene into individual objects, necessary

to locate radioactive sources in a given volume. It requires an active scan of the area of interest prior to any radiometric measurements which is time consuming, requires repeated measurements if the area changes and has problems mapping reflective surfaces [67]. These limitations will be highlighted in comparison to the advantages gained by using a stereoscopic camera over the course of this section and in doing so justify this research into the first Compton/stereoscopic fused system.

Note that the theory in this section is a very basic description of some select challenges faced in stereoscopic imaging and the means by which systems such as the one used in this project overcomes them. Machine vision is a topic of substantial depth and further information can be found in [68].

3.3.1 Stereoscopic Camera Theory

The stereoscopic camera gives at least two images of the same scene but from different viewpoints. Depending on their position in 3D space, details in these images will appear in different places. If two matching pixels can be found in each image two 3D ray paths can be drawn between each camera and the pixel in question. The point at which these two paths intersect gives the position of this pixel in 3D space. This is presented schematically in Figure 3.3 (reproduced from [67]). Two optical rays are shown reflected from an object at a point of interest P to cameras at point p_L and p_R. They both have focal lengths of f and so the rays pass through their respective focal points at C_L and C_R, while the distance between cameras (known as the *baseline*) is b. Taking the distance along the axis of depth between the focal point of the left camera and point of interest as Z and the distance along the lateral axis between the same points as X, it can be shown using similar triangles that

$$\frac{x_L}{f} = \frac{X}{Z} \tag{3.2}$$

and

$$\frac{x_R}{f} = \frac{X+b}{Z}. \tag{3.3}$$

The change in image point location between cameras is known as *disparity* and can also be deduced to be

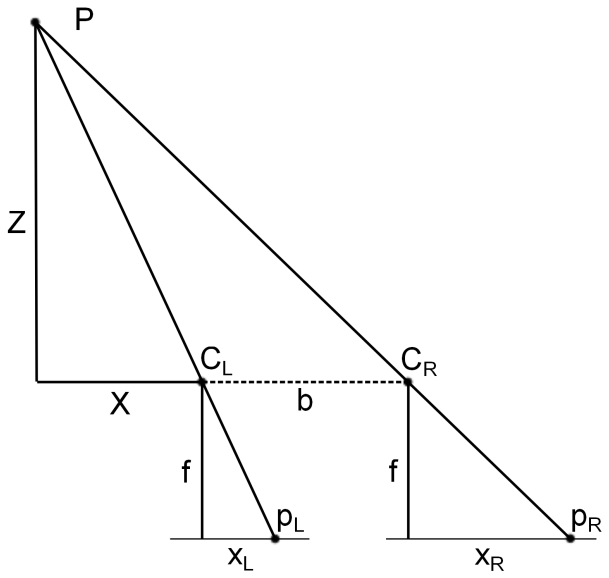

Figure 3.3: Schematic diagram of a stereoscopic system. Reproduced from [67].

$$d = x_R - x_L = \frac{fb}{Z}. \tag{3.4}$$

As disparity is inversely proportional to depth, it is clear that for fixed focal distance and baseline values the disparity is the key to gaining depth information. The inverse relationship between disparity and depth can be easily demonstrated by moving your finger closer to your face while looking at it through one eye at a time; as the distance gets smaller the difference between the images increases.

From this approach there are two prominent challenges to attain 3D information: finding matching pixels in each image, known as the *correspondence problem* and accurately projecting the path of the 3D ray, known as the *calibration problem* (also known as the reconstruction problem [69]). As shown previously, extracting depth information from two cameras requires the ability to project a line from an image to a pixel of interest through 3D space. Camera calibration requires the focal length and aperture size are known to a high degree of accuracy, alongside the positions of each camera in the stereo system; without this

information the projection of the 3D ray will be miscalculated leading to disparity errors. With this information the optical parameters of each camera can be calculated allowing the system to correctly construct the triangles necessary to generate accurate disparity maps. The calibration problem thus tends to be a technical challenge that is overcome by the manufacturers with no input by the end user. Considering the correspondence problem gives a greater understanding of stereoscopic vision as a whole, while problems in disparity generation are likely to be caused by it. To this end the correspondence problem is explained in greater detail below.

The Correspondence Problem

The stereoscopic camera approach hinges on finding the same pixels in both camera images. This is not a trivial process; there is no guarantee the pixels will have the same intensity due to varying lighting conditions between images and areas visible in one image may be obscured in another (this is known as *occlusion*). Furthermore, an area of repetitive intensity such as a bland wall or a repeated pattern such as wallpaper can lead to incorrect matches and errors in depth calculation. It is a case of finding pixels that contain enough information to allow high quality matching and algorithms tend to fall into either *feature* or *area* based approaches [70]. Feature matching localises disparity map generation on distinctive objects in the scene which is useful if it is these areas that are of most interest, but in projects such as this where radiation hot spots are of interest the most visually distinctive regions may not be those of importance. The Triclops disparity generation software provided by Point Grey [71] allows both feature and area based matching depending on the application allowing the algorithm to be tailored to the environment of interest. Area based matching is required to generate a disparity map at all points (known as a dense disparity map) and there are a large number of approaches to this. For the purposes of this introduction to the problem the widely used epipolar constraint is highlighted alongside the Sum of Absolute Differences (SAD) matching algorithm used by the stereoscopic camera employed in this project [72]. There are other constraints such as uniquness where only one match is found in each camera and continuity where disparity must change gradually across surfaces but these concepts are difficult to implement and their explanation would be excessive for this introduction.

The epipolar constraint can be ascertained by considering a stereoscopic system with two cameras where both are held at a parallel height. This is a common configuration for stereoscopic cameras as it significantly reduces the difficulty of the correspondence problem and a schematic diagram of this case is shown in Figure 3.4. Worth noting is that as in Figure 3.3 the image plane in real cameras is behind the focal point and an inverted image is recorded, whereas in this case a *virtual* image plane is placed the same distance in front of the focal point. This would theoretically show an unrotated image and makes the logic of the epipolar constraint easier to comprehend, though it still holds true for a real camera [73]. When a pixel is identified in the left camera, it is known the position of the object P is somewhere on the line that can be drawn between its position on the image plane p_L and the focal point C_L. If this ray was visible it would leave a line across the image plane of the right camera on which this object must lie. This is known as the *epipolar line* (e_R for the right camera) and by using two cameras held parallel on a given axis the resulting epipolar lines will be parallel as well. This turns a problem that was initially two dimensional into a single dimension, making matches more robust and computationally easier which in turn makes generating disparity maps a quicker process.

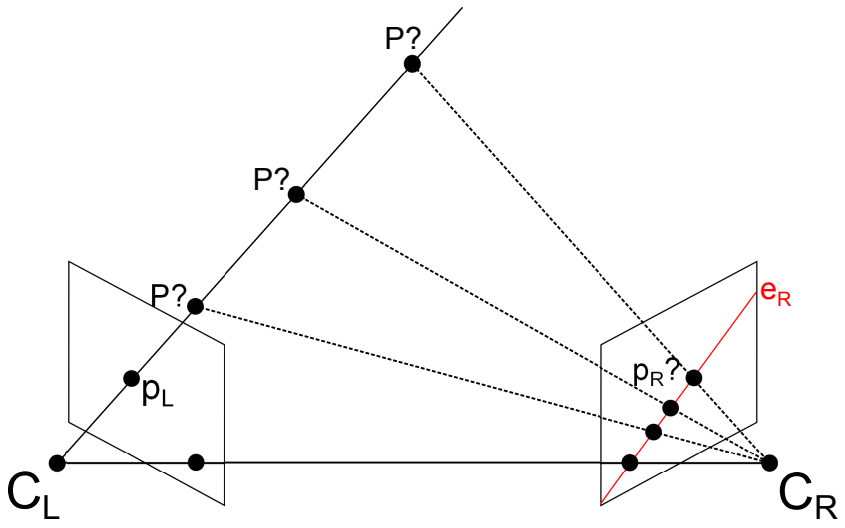

Figure 3.4: Schematic diagram of a stereoscopic system with two cameras held at a parallel height to demonstrate the epipolar constraint.

While holding pinhole cameras with the same focal length parallel introduces the epipo-

lar constraint automatically, there are times when such a setup may not be practical. In these cases, parallelism can be achieved by means of *image rectification*. This is the case of translating the images from the left and right cameras onto a single plane along which the epipolar lines are constrained to a single dimension. It can only be achieved once a stereo system has been calibrated and creates a virtual image plane where differences between camera rotation, lens used and focal length in differing cameras are accounted for [74]. This is also necessary for modern digital cameras that due to lens curvature do not conform to a pinhole camera model.

Sum of Absolute Differences

While the epipolar constraint makes stereo matching simpler the matching process is still a challenging problem and there are a number of commonly used algorithms. The camera used in this project employs the Sum of Absolute Differences algorithm, a widely used approach preferred for its simplicity allowing fast disparity generation [72]. For a chosen pixel in the left camera a larger window of pixels (say 5x5 pixels) around it is taken and compared to an identical window of pixels in the right camera moved through a larger window (say 50x50 pixels). This method is necessary as comparing the similarity of single pixels in each camera will lead to mismatches far more often than comparing a number of pixels, leading to a low quality disparity map. As this matrix is moved through the right camera and each pixel compared to its corresponding pixel in the left camera matrix a number for each pixel pair is generated corresponding to the difference between them. By summing the absolute differences of each pixel a value for each matrix comparison is generated; the lowest number corresponds to the closest match and the distance between the middle pixel of this match and the initial pixel is taken as the disparity. Mathematically this process is represented as

$$SAD(x, y, d) = \sum_{i,j=n}^{n} |L(x + j, y + i) - R(x + j + d, y + i)|, \tag{3.5}$$

where (x, y, d) is the disparity between point $L(x, y)$ in the left image and point $R(x + d, y)$ in the right. The value of d that minimises the SAD is taken as the true disparity. The speed of the match depends on how quickly the algorithm converges to the lowest SAD. The specifics of the matching algorithms used by proprietary stereoscopic software

are closely guarded secrets and so cannot be discussed further.

3.3.2 Project Stereoscopic Camera System

While the Compton camera and associated software was developed at the University of Liverpool, the nuclear imaging department had no experience in stereoscopic camera fabrication. As a result it was decided that this equipment would be purchased from a third party with complete functionality to allow focus on the radiometric and imaging fusion aspects. Research into available systems was undertaken with a view to finding the most suitable for this project based on a number of criteria. The chosen system would need to be calibrated out of the box and come equipped with its own accurate, efficient matching algorithm. It must have a baseline camera separation that allows accurate disparity map generation from the order of centimetres to metres. Furthermore, it must allow access to the code pipeline generated by the matching software and have compatibility with codes used to generate radiometric data (namely C/C++ and Matlab). On these grounds, the Bumblebee XB3 produced by Point Grey was chosen [71].

Figure 3.5: The Bumblebee XB3 stereoscopic camera developed by Point Grey Research. [71].

The Bumblebee XB3 is a stereo system comprised of three Sony 1.3 megapixel, 6.08 mm sensor cameras (ICX445, measured diagonally, 1/3 type). Individually, the monochromatic cameras have a resolution of 1280×960 pixels, each square pixel with dimensions of 3.75 μm. The cameras are spaced 12 cm apart, giving possible configurations of both 12 cm and 24 cm baselines. This results in a stereo resolution of 1280 $\times$ 960 pixels with a calibration to within 0.1 pixels Root Mean Squared error carried out before shipping, with a frame rate of

15 FPS. The dimensions of the unit as a whole are 277 × 37 × 41.8 mm with a weight 505 g and a power consumption of 4 W at 12 V. The cameras have focal lengths of 3.8 mm chosen over 6 mm options to give a larger 66 degree horizontal field of view, allowing the huge field of view of the Compton camera to be harnessed at the expense of a manageable degradation in depth accuracy at increasing depths. Figure 3.6 highlights the tradeoff between depth accuracy and field of view for possible baseline and focal length configurations (reproduced from rough guideline functions provided by [71]). As can be seen the error on depth is greatest when using the 3.8 mm focal length though this is negated somewhat by using the 24 cm baseline setup if the error is large enough to affect source location. Conversely, the 24 cm baseline shows a reduced field of view below depth ranges of 10 m while the 6 mm focal length cameras comparatively reduce the field of view by over 20 degrees for all depths. This means that while the 3.8 mm focal length was the preferable choice for this project both the 12 cm and 24 cm baselines may be advantageous to employ depending on the environment.

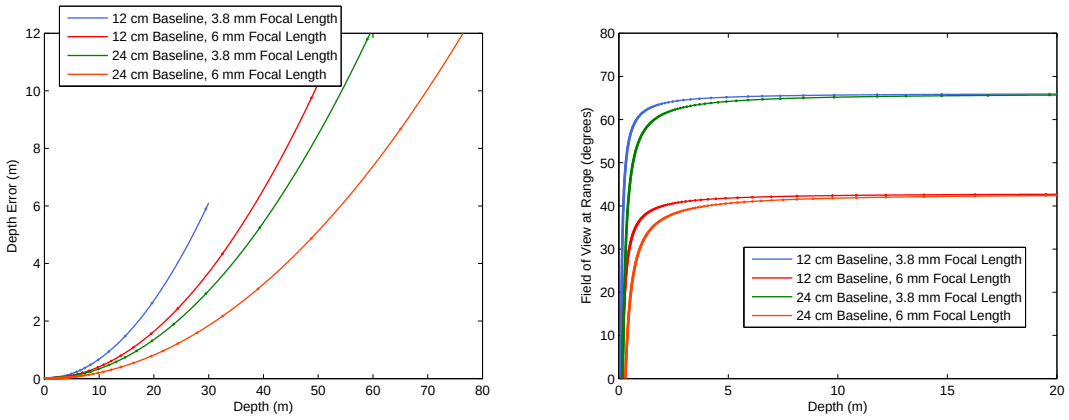

Figure 3.6: Guideline graphs showing differences in accuracy of depth calculation (left) and field of view (right) for configurations of the Point Grey Bumblebee XB3 stereoscopic camera. Shown are all combinations of 12 cm and 24 cm baselines and 3.8 mm and 6 mm focal lengths.

With their stereoscopic cameras Point Grey provide two software packages to provide maximum functionality and ease of use. Flycapture SDK is provided with all Point Grey products and handles image acquisition and camera control. The application programming interfaces (or APIs) are provided through Flycapture so radiometric C++ data can be ap-

plied to generated depth images through this software (though image fusion was actually handled in MATLAB for this project). The depth images are first generated by the Triclops SDK software that handles the image rectification and generates depth images. The processing speed examples provided by Point Grey show that a computer with an Intel Pentium IV processor of 2.8 GHz and 1 GB of RAM can generate 102 million disparity calculations per second from a three camera stereoscopic system. These figures are from 2004 and computer power now far exceeds this so there were no concerns about processing limitations hindering depth map generation. Point Grey claim full field-of-view depth images can be generated at speeds up to 30Hz [71] which, while only providing a potential video frame rate of 0.5 fps, is sufficient in most cases to provide real-time depth information.

Lastly, it is worth noting that while the specifics of the camera and associated software were the prominent factors in opting for the Point Grey Bumblebee XB3, their experience in collaborating on academic projects such as this was also encouraging. Their stereoscopic systems have notably found applications in long range rover autonomy [75] but of particular interest is the MicronTracker vision-guided surgery system [76]. Harnessing the two camera Bumblebee2 model, the MicronTracker uses real time generated depth maps to track a surgeon's instrument inside a patient and relay this information to him. The noteworthy feature of the system with regards to the nuclear decommissioning project is the ability to overlay previously collected imaging data such as CT or MRI scans onto the depth maps. This allows any incisions to be made with enhanced care and precision but critically displays the ability to combine external imaging data with that produced by the stereoscopic system. Such examples support the belief that a radiometric and stereoscopic fused imaging system can be developed using this equipment.

Chapter 4

Experimental Procedures and Analysis

Developing a radiometric and optical stereoscopic fused imaging system required a number of experimental measurements to collect raw data of high quality and subsequent analysis to ensure precise and accurate fusion would be possible. This chapter details each stage of work carried out to achieve proof of concept of this system and highlights analytical results to illustrate the knowledge gained from each experiment.

4.1 Compton Camera Experiments: February 2012

The Liverpool Nuclear Instrumentation group has significant experience in the setup and analysis of Compton camera experiments such as SmartPET [59] and the PorGamRays spectrometer [77]. The first stage of this project would be to produce a Compton camera system that could give the best possible energy resolution and efficiency, before optimising the algorithms that process this data to secure the highest quality radiometric images. This experimental run commenced in February 2012 using the 5 mm + 20 mm germanium Compton camera described in Chapter 3.

4.1.1 Setup

The February 2012 experiment was the first of three Compton camera experiments, the others developing systems for homeland security and nuclear structure applications. The

aim of each experiment was to build up a collection of datasets from radioactive sources in known positions. This would allow the difference between image and source location as x,y and z distances were increased to be investigated.

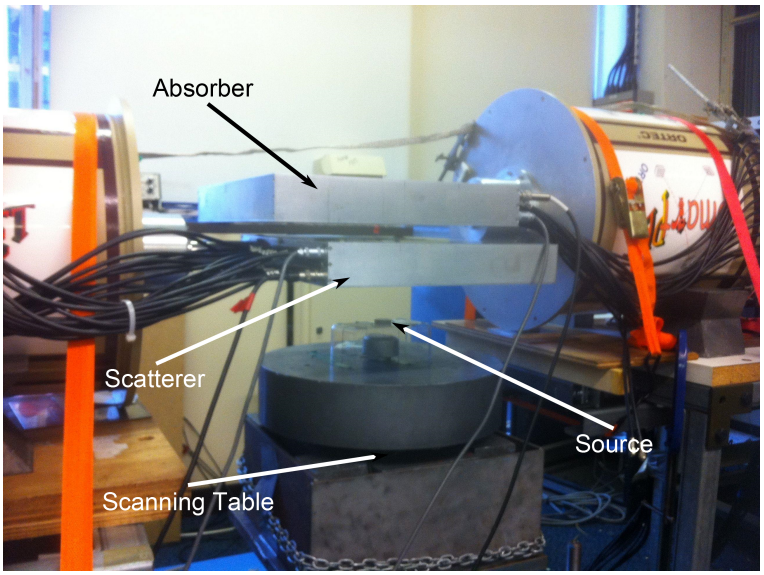

Figure 4.1: Image of the 5 mm + 20 mm germanium Compton camera as setup for the February 2012 experiment.

In past Compton camera projects the radioactive sources would be located in known positions and as such the Compton camera could be moved so that it focused on this particular area. In Nuclear Decommissioning radioactive sources will likely be located in a large number of places and the system must be able to image them correctly no matter where it is pointed towards. In this scenario it is important the system can image sources at large standoff distances and viewing angles. An investigation into how accurately the reconstructed image position reflects the true source position had never been carried out so it was imperative this was measured so it could be accounted for before stereoscopic fusion could take place. To realise this the system was set up as shown in Figure 4.1 and schematically in Figure 4.2. The DC side of the scatterer and AC side of the absorber faced the sources, with a crystal separation of 5 cm.

While this is a common setup for a Compton camera, a novel approach was used to achieve this source positioning. Instead of moving the sources by hand which can introduce

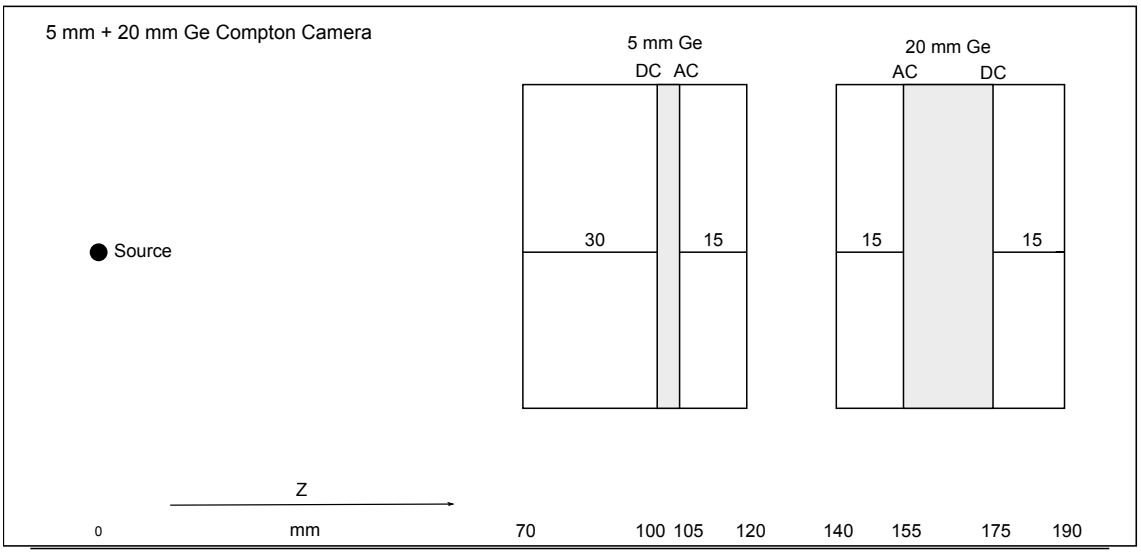

Figure 4.2: Schematic diagram of the 5 mm + 20 mm germanium Compton camera as setup for the February 2012 experiment.

human error and make multiple position measurements difficult, point sources were mounted on the scanning table used to characterise AGATA HPGe crystals at the University of Liverpool [78]. The scanning table allows sources to be moved through a set of predefined coordinates for fixed times, making precise position measurements obtainable. After careful deliberation it was decided a 6 x 6 grid of 36 source positions in x and y directions would be taken, with 20 mm between each position. This creates an x-y grid as shown in Figure 4.3 where the black square shows the x-y position of the detector. This grid gives a good number of position measurements with a rigid shape that will make any discrepancy between image and true source position apparent. While usually the detectors are aligned using a custom built gantry that ensures the crystals have the same lateral positions it was not possible to incoportate the scanning table into this setup. As such, it was necessary to align the detectors by hand and confirm this by scanning the detectors with a collimated beam from the 1 GBq ^{137}Cs scanning table source. The beam is scanned in 1 mm steps through x and y dimensions and any detector misalignments become apparent and can be corrected.

Each dataset was comprised of 36 measurements at differing x-y positions but all at the same standoff distance using the same radioactive point source. To investigate the system's

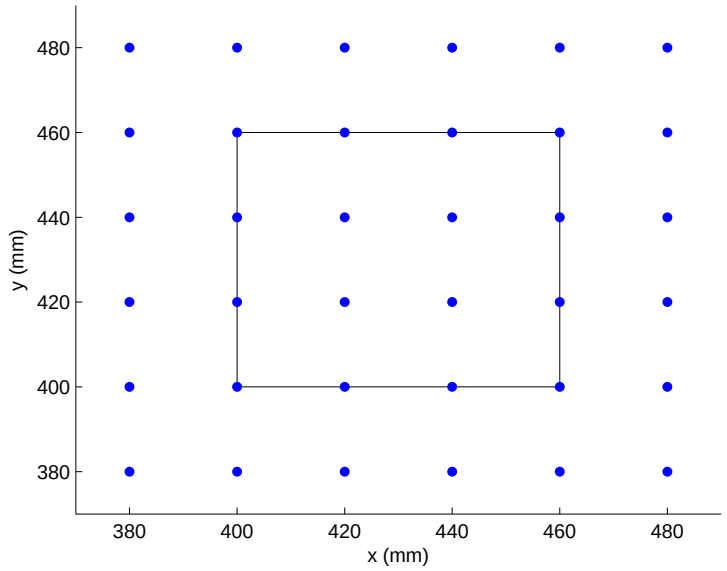

Figure 4.3: Schematic diagram of the source positions in x and y for datasets taken during the February 2012 experiment. The black square shows the position of the detectors.

response to γ-ray energy and depth a number of datasets were taken using ^{137}Cs, ^{152}Eu and ^{60}Co point sources at a number of different standoff distances. The collimated beam under the scanning table was attenuated using a lead block and the point sources placed on top of this, allowing the precise positioning of the scanning table to be used. Details of each dataset as well as a summary of relevant detector and source details can be found in Appendix A.1.

The electronics to process the collected charge pulses were setup as shown in Figure 4.4. This is the electronic component chain that allows the data of interest to be extracted from the collected charge in the detector, in this case energy, time and the charge collection as a function of time (pulses used in Pulse Shape Analysis). The preamplifiers of each detector collect charge as explained in Chapter 2, creating voltage pulses of 300 mV/MeV with rise times in the order of nanoseconds and decay times in the order of microseconds. These pulses are passed to Gain/Offset boxes (known as GO boxes) that allow the pulses to be amplified by fixed gain values and offset by variable voltages. The offset allows the baseline of each channel to be changed and by having a negative baseline when processing

positive pulses (or positive baseline when processing negative pulses) the dynamic range of the DAQ cards can be maximised. The amplification of the pulses was vital to record pulses large enough to perform PSA on and this was achieved using a gain factor of 10. These amplified pulses are then sent to the CAEN V1724 digitizer cards [79], state of the art Analogue-to-Digital conversion cards that digitise and save 1280 ns of each pulse (more than sufficient for this application).

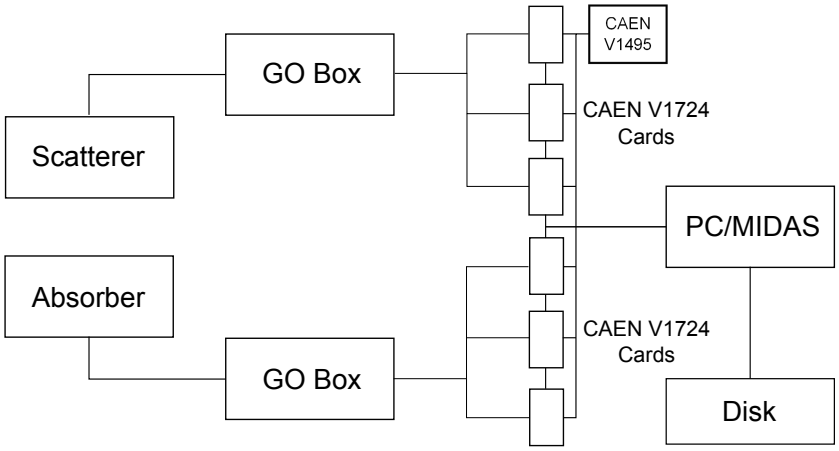

Figure 4.4: Schematic diagram of the electronic signal processing chain used in the February 2012 Compton camera experiments.

The CAEN V1724 cards have an input range of 2.25 V and a sample rate of 100 MHz. The energy deposited in the detector is calculated by the inbuilt Moving Window Deconvolution method [80] (MWD) or by taking the difference between the baseline values before and after charge collection. Arguably more useful is the fact that the triggers (logic pulses that are generated when charge values exceed a given threshold) are synchronised to a universal clock, made possible as all the cards are connected through a trigger chain as shown in Figure 4.4. As the time of all interactions are known it is easy to set trigger logic digitally, so for this project a gate was set that only accepted events where there was an interaction in the scatterer and absorber within a coincidence time window of 75 ns. The triggers are controlled by the V1495 trigger card which accepts a trigger pulse from each card and sends an acceptance signal back to each card if the required trigger logic is met. Furthermore, the energy thresholds for these triggers can also be set from the computer; for this experiment

it is vital that the scatterer triggers on the smallest energy values possible above the noise level as this will allow for the optimal low energy limit. The MWD algorithm and digital trigger can be explained in greater depth by referring to the schematic diagrams of the pulse processing chains illustrated in Figure 4.5. A typical pre-amplifier pulse is shown at 'MWD a', and 'MWD b' shows how this pulse is made into a 'step function' by removing the exponential decay of the pulse, keeping it at the fixed maximum pulse height for its duration. The step function is smoothed by using a fixed window to take the average pulse height in this range of samples and moving this window through the pulse. This gives a trapezoidal pulse shape as seen in 'MWD c', from which the pulse height is measured. The size of the moving window and flat top of the step function are user controlled, and in this case were 5.5 μs and 2.5 μs respectively. 'DTP a' shows a pre-amplifier pulse over a much shorter timescale so the leading edge is visible. 'DTP b' shows the double differentiation of the pre-amplifier pulse and it is this pulse that is used for triggering. Once a user set threshold is crossed (1) the trigger is 'armed', meaning it is ready to trigger when the pulse crosses the zero crossing point (2). The zero crossing point corresponds to the maximum of the pre-amplifier pulse height and once this is reached the CAEN V1495 card sends back a trigger request to the corresponding V1724 card to accept this pulse.

The new 5 mm HPGe detector requires a smaller bias voltage to fully deplete, leading to a smaller capacitively generated noise and allowing the thresholds to be set lower than any previous experiments at around 7 keV. The threshold on the absorber was also set to a similar energy of around 7 keV; though this is not a major problem it will lead to a greater number of random coincidences and in typical practice a higher absorber threshold well out of the range of noise is preferable. This system will ultimately operate in high radiation backgrounds that generate a large number of random coincidences so it is important it can function with this setup. Finally, the raw data is passed to a PC using the MIDAS package [81]. This software processes the raw data and provides a coding framework whereby it can be manipulated to generate spectra and perform other analysis.

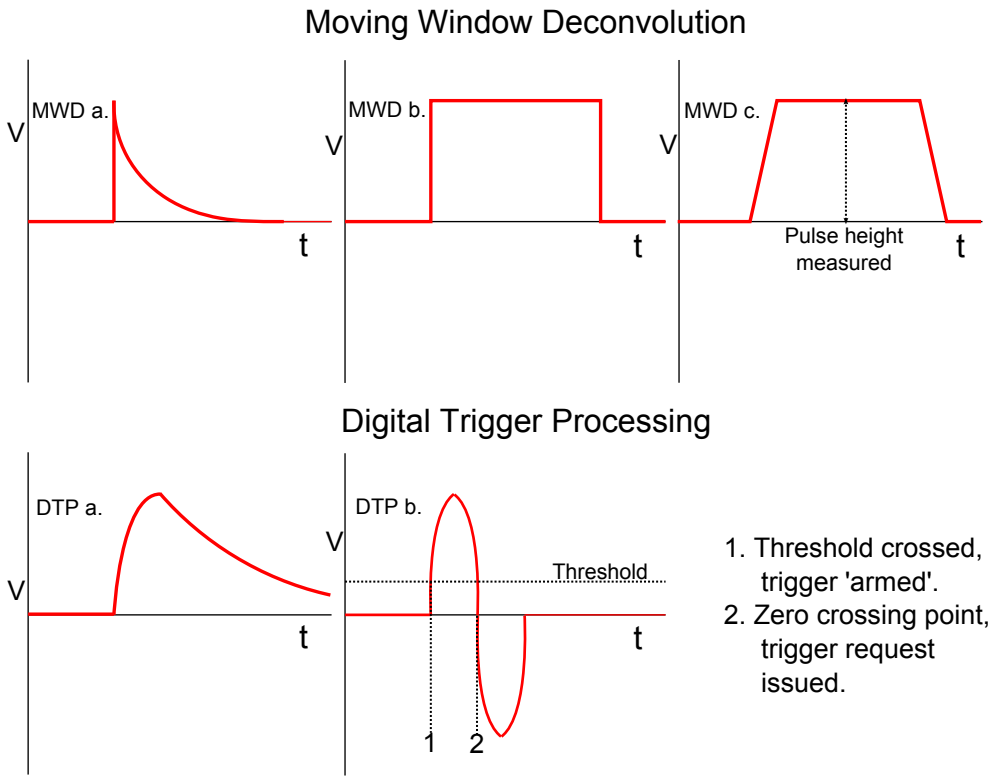

Figure 4.5: Schematic diagram of the pulse processing involved in the Moving Window Deconvolution algorithm used to measure pulse height and the digital trigger employed in this experiment.

4.1.2 Analysis

Using the setup outlined, the datasets detailed in Appendix A.1 were collected. To ensure the quality of the collected data basic preliminary spectra and images were produced. They highlight the basic properties of HPGe and the Compton camera system while providing a basis upon which more detailed analysis is performed. The first step to check is the energy spectra as they give a clear indication of the energy resolution, dynamic energy range and efficiency of the system, though methods for improving efficiency will be presented later so the former two will be focused upon here. Summing the energy spectra from the scatterer and absorber gives full photopeak energies for the events that fully deposit their energies. Figure 4.6 shows an addback energy spectrum from a full ^{152}Eu dataset (Run 68/69/70 as detailed in Appendix A.1) with superimposed energy resolution information on many of the prominent peaks. The wide energy range of the system is apparent with all significant peaks

from 122 to 1408 keV clearly visible and as this spectra represents the imaging range of the system it is clear that this is sufficient for this project. The resolution may seem initially poor, as 20 mm HPGe SmartPET detectors can typically have a 1.5 - 2.5 keV FWHM of energy peaks in this range [82] and the 5 mm detector should achieve even lower than this. However, these measurements were taken for single detector measurements while this spectra shows the summation of measurements from the scatterer and absorber detectors giving two sources of error. The combination of these errors leads to degraded FWHM values between 3.1 and 4.4 keV. The FWHM values for a single channel on the AC side of the 20 mm detector (AC06) is also shown for comparison. The singles resolution gives FWHM values between 2.3 - 2.9 keV, slightly worse than in previous experiments using this detector. This may be due to electronic noise or degradation of the detector crystal between experiments.

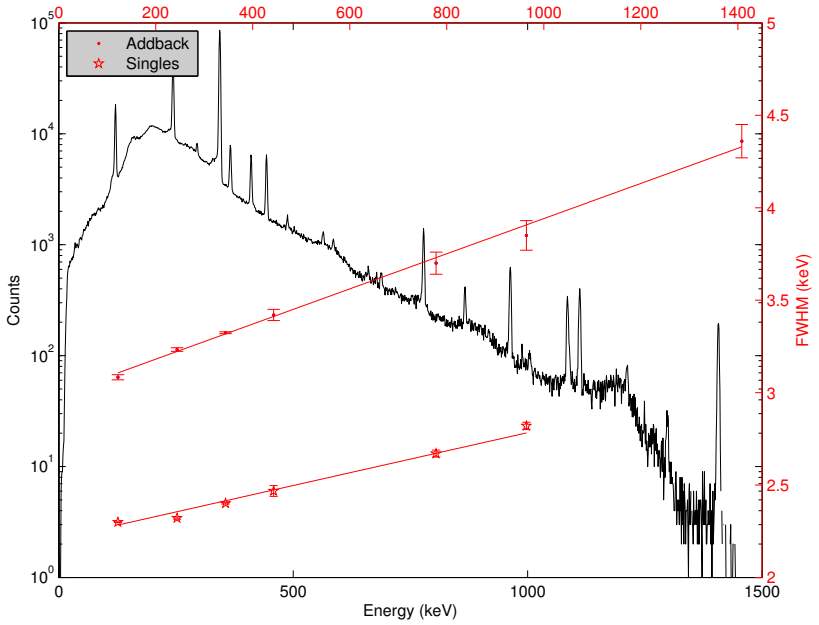

Figure 4.6: A ^{152}Eu addback energy spectum taken from the February 2012 Compton camera system (black), with associated addback FWHM values for several main peaks (red dots). Singles FWHM measurements also shown (red stars), singles energy spectrum not shown.

Plotting the energy spectra from the scatterer and absorber against each other in a 2D

matrix gives further insight into the nature of coincident timing systems and this is shown in Figure 4.7. The z axis represented by the colourmap is reduced to a maximum value of 100 as this is necessary to make many of the features of the image visible, though it means relative intensities between counts over 100 are lost and as such this figure provides only qualitative information. The diagonal lines represent energy peaks and as can be seen the energy depositions in each detector can significantly vary, which translates to a large variation in potential scattering angles. In addition there are 'hot spots' on these lines that correspond to the most likely energy depositions in each detector. This leads to a probable scattering angle as predicted by the Klein-Nishina formula and as you move through the energy peaks the 'hot spots' move closer to the top-left of their respective lines; This translates to ever smaller energy depositions in the scatterer and is proof of forward scattering with increasing energy as predicted by Klein-Nishina. The horizontal and vertical lines show random coincident events where a gamma ray from the source is absorbed in one detector and an unrelated energy deposition occurs in the other detector within the coincidence time window. This is more likely to occur for lower energy gamma-rays that have a higher probability of photoelectric absorption and the figure shows a strong vertical line at 122 keV because of this. The final feature of interest is the large 'cloud' of low energy coincidences, which simply corresponds to a number of low energy random coincidences between two unrelated energy depositions. As they seem to be energy deposits in the region of 40 keV in the scatterer and a spread of energies in the absorber this could be caused by x-ray and gamma-ray coincidences. They form the low energy background in the energy spectra and as seen in Figure 4.6 are easily distinguishable from true peak coincidences.

By taking the information on which strips collected the charge carriers each gamma-ray interaction can be deduced to have occurred in a 5 mm x 5 mm x 5 mm voxel in the scatterer and 5 mm x 5 mm x 20 mm voxel in the absorber. This should correspond to energy collected on a single strip on each side of both detectors, known as a Fold(1,1,1,1) event. The relative probability of a Fold 1 event on the AC side of the absorber is illustrated in Figure 4.8. You can see that while Fold 1 events are the most prevalent there are still a significant number of higher fold events and a number of Fold 0 events; this is when the cards register an energy deposit above threshold limits but further analysis finds the energy

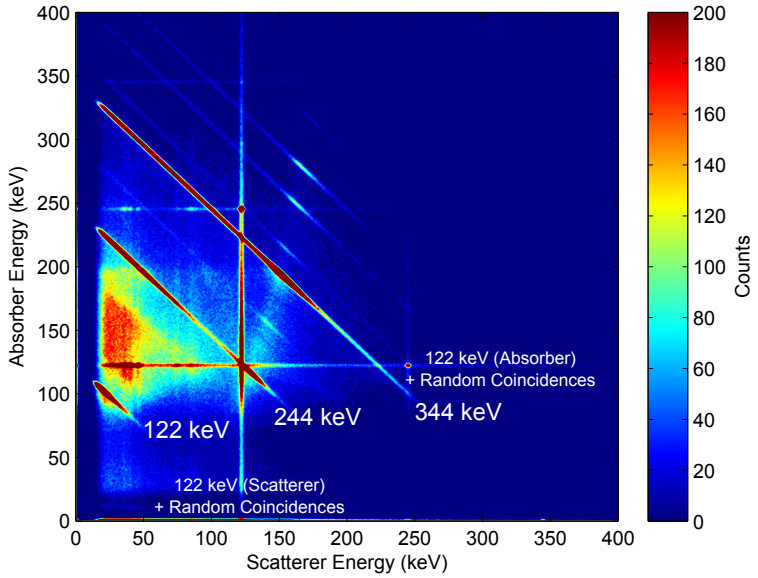

Figure 4.7: Energies deposited in the scatterer against energies deposited in the absorber for the same ^{152}Eu data as Figure 4.6.

to be statistically insignificant when compared with background fluctuations.

By taking these interaction positions with their respective energy deposits a back-projected cone can be constructed for each true Compton scatter and subsequent absorption. These cones are calculated by a code created by Dr Judson, a Post-Doctorate researcher at the University of Liverpool [83]. By calculating only the ellipses created by intersecting these cones at planes of interest the code quickly builds up 2D matrices of cone intersections. The 2D plane of interest is split up into pixels where the pixel size is controlled by the user; larger pixels creates more intersections and so images can be created from less data but at the cost of degrading achievable image resolution. Controlling the pixel size is known as phase space compression and must be chosen carefully according to the standoff distance of the imaging source and number of counts used in image reconstruction. Radiometric images are formed from these matrices and taking intersections as a function of x and y direction allows image resolution to be extracted for a given z plane. The code is C++ based, employing the ROOT toolkit libraries for peak fitting [84]. These images are gated on photopeaks to ensure a large number of true counts relative to the background

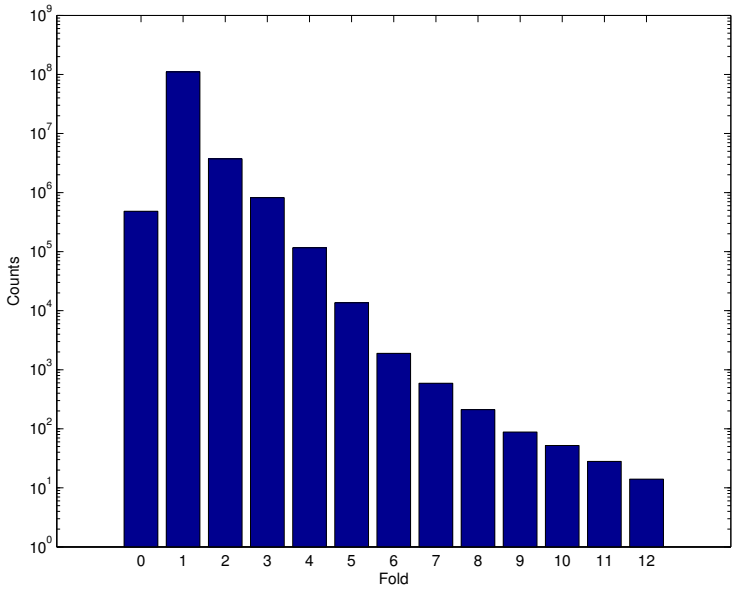

Figure 4.8: Absorber event fold for ^{137}Cs point source data placed 5 cm from the scatterer crystal face.

and the code is known as a *back-projection* algorithm with similarities to those used in medical imaging [85]. Figure 4.9 shows a 2D and 3D contour image of a ^{137}Cs point source 5 cm from the scatterer crystal face and 1 cm in x and y from the centre of the detector (90 mm in x and y on the image plane). The images are reconstructed from the known z plane in which the source lies with a phase space compression of 1 mm and the position and shape of the sources are clearly visible. By fitting a Lorentzian function to the counts as a function of x and y positions image resolution can be attained. Lorentzian fitting was chosen empirically by the developer as the most accurate reflection of the data trend. This particular image has a FWHM of 14.26 mm $\pm$ 0.97 in x and 14.00 mm $\pm$ 0.79 in y.

The position resolution of an image depends on the accuracy of the intersection between back-projected cones. This is governed by the energy resolution of the detectors used as explained in Chapter 2 but also the position resolution of the detectors; if the interaction positions can be ascertained to a greater degree of accuracy then the resulting cones will also more accurately reflect the true source position. While the energy resolution of the detectors is a fixed property of the detector and DAQ system the position resolution can

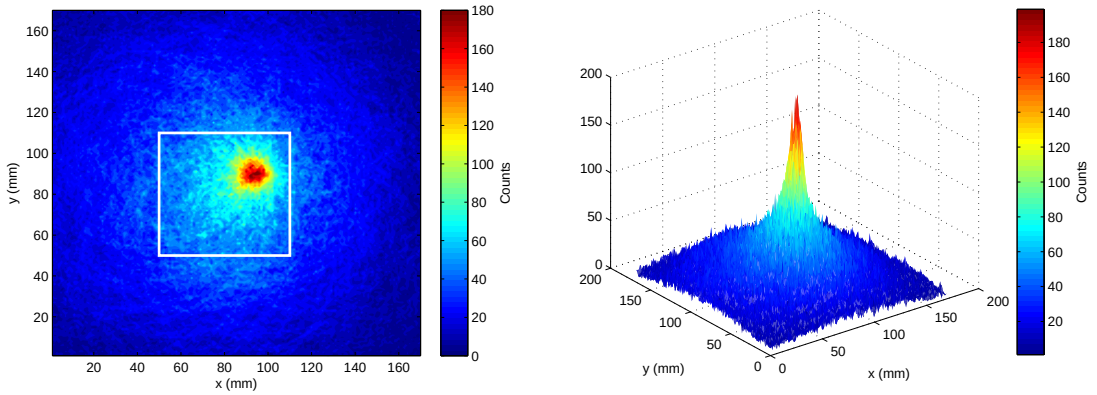

Figure 4.9: 2D and 3D contour images of a ^{137}Cs point source from matrices generated by the analytical back-projection imaging code. The white square on the 2D image shows the lateral dimensions of the detector crystals.

be improved by studying the charge collection as a function of time. Once the data had been analysed on a basic level and found to be of sufficient quality (by creating accurate radiometric images), the next step was to perform Pulse Shape Analysis to obtain the highest standard of generated radiometric images.

Pulse Shape Analysis

As shown in Chapter 2, the interaction position of a gamma ray has a marked effect on shape of the collected charge pulse. This is highlighted qualitatively in the left plot of Figure 4.10, which shows 22 charge pulses at a fixed lateral position but with 1 mm changes in depth through the SmartPET detector. They were taken as part of previous SmartPET charcterisation measurements in an alternative approach to PSA that can be found in [86]. The red pulses show the interactions closest to the electrode while the blue pulses show those furthest away. The differences in charge collection time (known as risetime) are apparent but this has to be quantified to be of use and the method used for doing so is detailed in the right hand plot of Figure 4.10. This plot shows the closest interaction to the charge collecting electrode from the left hand plot and highlights two time measurements: t30 and t90. These correspond to the time taken to collect a further 20 and 80 percent of the charge pulse respectively from an initial 10 percent. The measurement begins at 10 percent

rather than 0 to avoid errors due to baseline noise, while 30 and 90 percent are chosen as measurements as the values allow pulses to be confidently distinguished. As can be seen the t30 values directly correspond to the interaction distance from the electrode, while the t90 values can overlap and take a wider range of values. This is important when trying to ascertain positional information from these values as will be discussed later. As previously stated the CAEN V1724 cards have a sampling rate of 100 MHz giving charge samples at 10 ns intervals. These points are passed to a interpolation algorithm which smoothes the data with a five point moving average, giving interpolated charge values at 2 ns intervals.

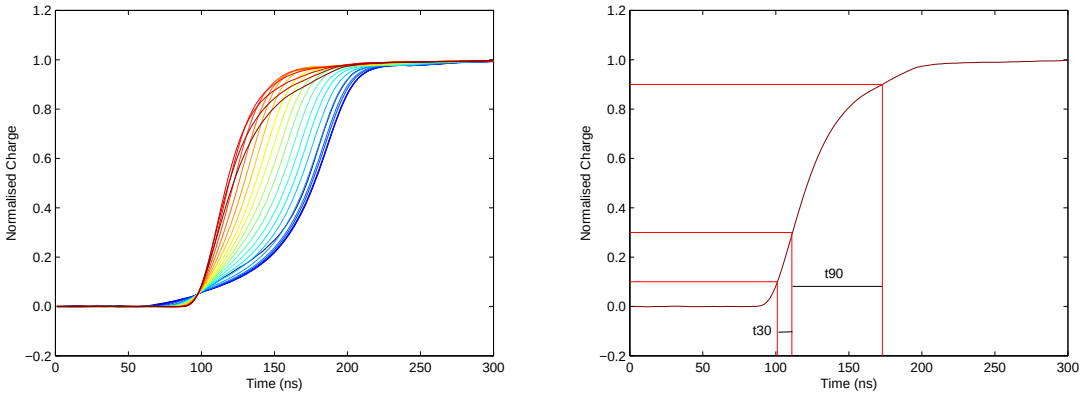

Figure 4.10: A series of charge pulses at a fixed x-y position and at 1 mm steps through depth in the SmartPET detector, where red is the closest and blue the furthest pulse from the charge collecting electrode (left). The closest pulse shows the time difference from 10 to 30 % and 10 to 90 % of the pulse height, measurements known as t30 and t90 respectively (right).

Before the risetime values can be used to extract positional information pulses must be analysed to ensure only single interactions in each voxel are used. If there are two or more interactions then PSA cannot be used to find a more accurate interaction as the resulting charge pulse is far more complicated to interpret and more obviously cannot be resolved to a single position. The multiple interaction pulses can be identified by changes in gradient corresponding to the collection of more than one set of charge carriers at each electrode; the pulse appears to have several 'stages' where each corresponds to an interaction. To identify these the pulses the derivative of the pulse is calculated using a simple three point moving average. The gradient changes are displayed as peaks in the derivative pulse plots and these

are measured between 10 and 90 % of the pulse height to eliminate baseline noise effects. Any noise ringing on the pulse will cause small gradient changes in the derivative, so any changes of less than 20 % of the maximum gradient change are not taken as true interactions. This value was chosen after a visual inspection of the gradients of true interactions and noise but a more thorough investigation may be necessary in the future. Figure 4.11 shows two interpolated pulses in black with their derivates in red. The left is a single and the right is a double interaction; the gradient changes are clearly visible in each. The single interactions are gated on using this method and only these pulses are used in the next stage of PSA. By applying these gates 16.3% of the Compton events of interest are omitted but this drop in efficiency should be justifiable if it leads to a significant improvement in image resolution.

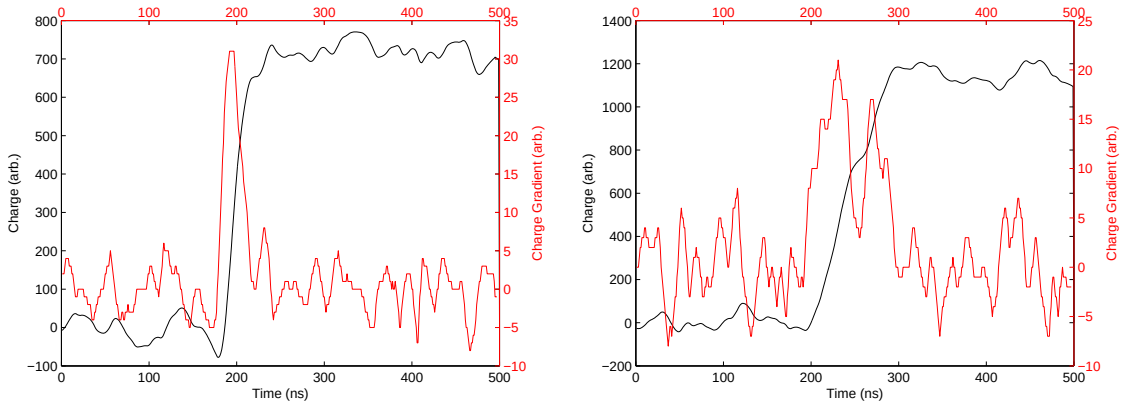

Figure 4.11: Interpolated charge pulses (black) with their respective derivatives (red). The left pulse is from a single interaction as shown by its single gradient peak, whereas the right is a double interaction pulse as shown by the two gradient peaks.

The t30 and t90 values of the single interaction pulses are calculated using the method highlighted in Figure 4.10. The values are plotted against each other for each pulse and as can be seen in Figure 4.12 the differences in risetimes between pulses are emphasised by doing so. This figure shows t30 against t90 plots from the 20 mm absorber for the same ^{137}Cs dataset used to generate Figure 4.9, with and without single interaction derivative gates applied. They show the total response from all strips of the detector but the results are indicative of single strip response. There is a reduction in counts of 16.3% by applying the single interaction gates. This highlights the improvements made by gating on single

interactions in this way; the counts around the edges of the 'tick' shape are visibly reduced and these are likely to be caused by multiple interactions as their t30/t90 values do not follow this expected trend seen in previous risetime measurements using this detector [59]. It is clear that there are still counts accepted as single interactions that lie far away from the expected values and this is likely due to multiple interactions being wrongly accepted as singles. While the interaction gates in place are helpful they are not completely accurate and further investigation is required to improve them.

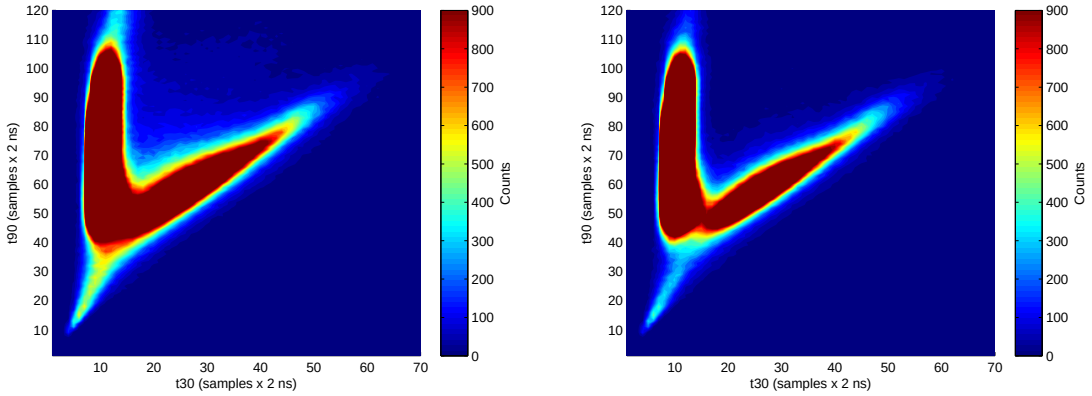

Figure 4.12: t30 against t90 plot for the 20 mm(right) HPGe crystal, before (left) and after (right) single interaction gates are applied

Figure 4.13 shows the t30/t90 gates applied to infer interaction depth. The left plot is from the thinner 5 mm crystal and the quicker risetimes reflect this, while the right plot shows the thicker 20 mm crystal with comparatively longer risetimes. Both show the charge collection times from the electrodes nearest the source, the DC side in the 5 mm and the AC side in the 20 mm crystal as it is these electrodes that were used in PSA calculations. The 'tick' shape seen in both plots is typical of t30 against t90 comparisons [59]; interactions far from the electrode of interest have long charge collection times and thus large t30/t90 values (the diagonal part of the tick). Interactions close to the electrode have small t30 values and small differences in position are apparent in a spread of t90 values (the vertical part of the tick). The black rectangles show gates initially applied on this tick that correspond to the assumed interaction depth in each crystal. The gates are first constructed from equally spaced gates on t30 values, 5 in the 5 mm crystal and 10 in the 20 mm crystal

corresponding to 1 mm and 2 mm depth positions respectively. The t90 gates ensure the gates only accepted events inside the 'tick' as it is these that are assumed to be true single interactions. Inspecting pulses from events outside this area shows them to be multiple interactions that were unable to be picked up by the first gate and other outliers that could be due to noise or cosmic events. This is an approach used in previous Compton camera work that made significant improvements to generated images [59]. The gates used here would later turn out to be preliminary as they were chosen by eye; future experimental work included a closer investigation into these gates and will be discussed later. While an approach to potentially improve depth position has now been established by analysing the charge collection at the electrode of interest, PSA can be developed further by considering the image charges in the adjacent electrodes.

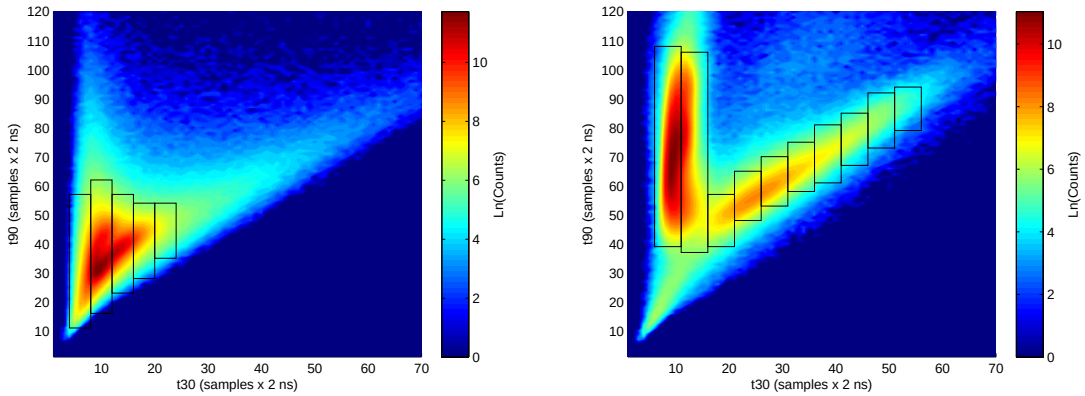

Figure 4.13: t30 against t90 plots for the 5 mm(left) and 20 mm(right) HPGe crystals. The rectangles show the t30 and t90 gates corresponding to 1 mm and 2 mm positions through depth in the 5 mm and 20 mm crystals respectively.

Image charges were introduced by contemplating the Schockley-Ramo theorem in Chapter 2. It was shown that the magnitude of the image charge on a given electrode was proportional to the distance between the interaction and that electrode. It follows that by considering the magnitude of the two adjacent electrodes relative to each other the lateral position resolution can be improved. As the electrodes on each side of both crystals are arranged orthogonally this process can be applied to both sides to improve position resolution in x and y. A value known as the image charge asymmetry parameter (denoted ICA)

is calculated using the equation:

$$ICA = \frac{A_r - A_l}{A_r + A_l}, \tag{4.1}$$

where A_r and A_l are the respective areas of the right and left image charges. The ICA takes a value between -1 and 1 where 0 represents an interaction in the middle of the strip, -1 is an interaction to the far left of the strip and +1 an interaction to the far right. The strips in both detectors are 5 mm across, so if the range between -1 and +1 is split into twenty steps of 0.1, each step represents a change in lateral position of 0.25 mm. Figure 4.14 shows a charge pulse from an electrode on the DC side of the 5 mm detector with respective image charges. It is clear that the right image charge exceeds the left in magnitude; by integrating across the length of each pulse (determined by the charge collection time of the true pulse) and using the Equation 4.1 an ICA value of 0.218 is obtained, confirming this. This is rounded to an integer value of 2 and taken as an interaction position of 2 x 0.25 mm = 0.5 mm to the right of the middle of the strip.

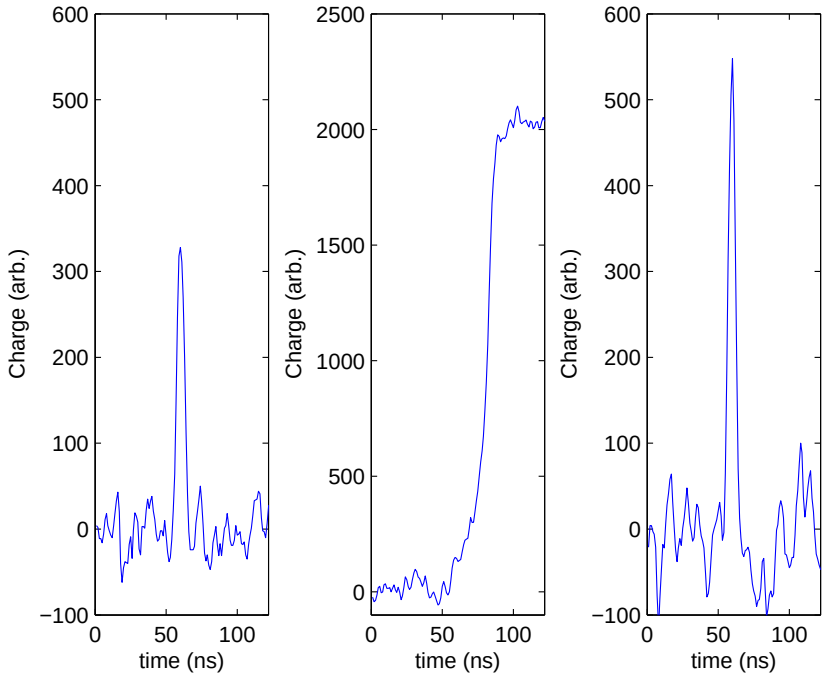

Figure 4.14: A real charge (centre) with its respective left and right image charges.

There are concerns about the noise level on the image charge pulses, highlighted in Figure 4.15. The real charge and its adjacent image charges are again shown, but in this case the image charges are too small to be identified against the background. The area of image charges are compared to the average baseline shifts to determine whether there is a significant charge deposit and statistically these image charges are considered viable, but it would appear accurately determining the asymmetry in them would be difficult.

The measured sizes of left and right image charges are compared in Figure 4.16. The 5 mm image charge areas were divided by 100 and the 20 mm areas by 300 to reduce the spread of the values and fill the bins with more statistics to give a greater indication of the plot shapes. In addition the 5 mm plots have 200 added to each image charge value and the 20 mm have 300 added; this ensures all the values are positive which is necessary for mtSort (the data sorting toolkit which is part of the MIDAS data acquisition system) to display the values. This measurement was carried out for the 20 mm detector as part of the SmartPET project by [60] and these figures show a similar response to this project, though the previous

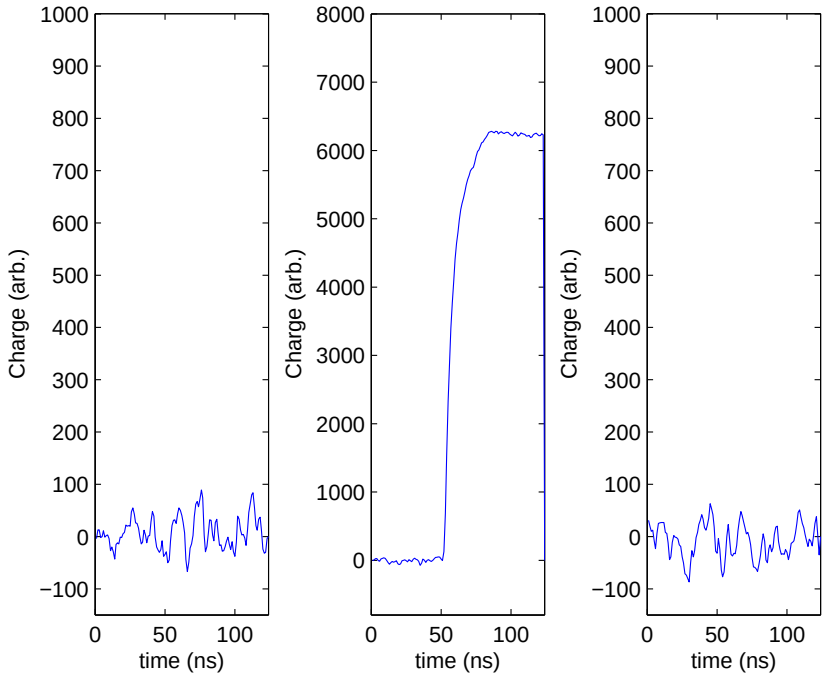

Figure 4.15: A real charge pulse (centre) with its respective left and right image charges.

measurements were taken using a collimated source aimed down the middle of the detector in Z, meaning there would be no effect on the ICA size as a function of interaction depth. In this work standard point sources placed in front of the scatterer crystal are used, as a result the detector face closest to the source generally collects large, positive image charges while the face furthest away collects smaller, negative image charges. The increased thickness of the 20 mm crystal means its electrodes show marked differences in response while the differences in the 5 mm crystal electrodes are less pronounced. Of note is the 'cross pattern' around 200 (essentially 0) that is due to the fact the image charges are not collected if they are below a threshold that means they are not significantly greater than noise. Image charges just above this threshold were shown in Figure 4.15 and an investigation into their size in relation to this threshold (and the energy of the original pulse) was undertaken to see how frequently these small image charges occur.

The threshold level at which an image chage is considered statistically significant is determined by considering the number of image charges relative to the number of true

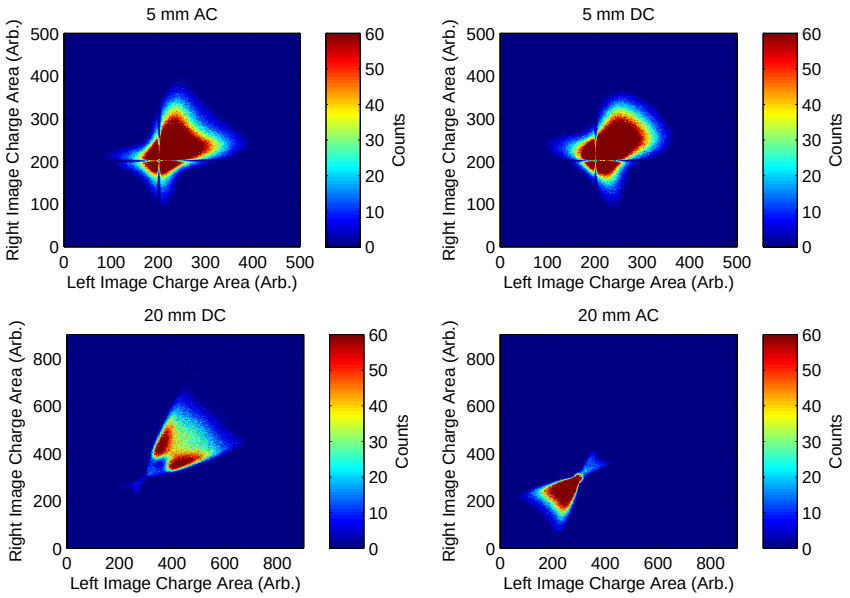

Figure 4.16: Plots of left against right image charges for each detector face of the Compton camera.

pulses. The threshold is set at the level that gives two image charges for every true pulse, the fractions that should be occuring in the detector. If it is set higher than this real image charges will be rejected, too low and noise will be accepted. This threshold is higher for the 20 mm crystal than the 5 mm as the larger depletion region leads to larger charge pulses and thus larger image charges. Figure 4.17 shows the sum of the left and right image charge magnitudes as a function of energy for the AC side of the scatterer and DC side of the absorber. What can be seen is that while there is a maximum limit to image charge size as a function of energy the minimum is close to 0 for most of the energy range; higher energy pulses can still have small image charges if the interaction occured far from the electrode of interest in depth which, as previously shown, may be difficult to determine against the noise. This figure highlights that it is not an option to simply throw away counts with small image charges as they occur for a large range of energies, particularly in the 5 mm scatterer. However the fact that the measured values follow an expected trend of general increase in image charge magnitude with energy that can be explained physically is a good indication they are correct. The best way to judge how well the image charges are being measured is to investigate the resulting Compton images produced with and without PSA.

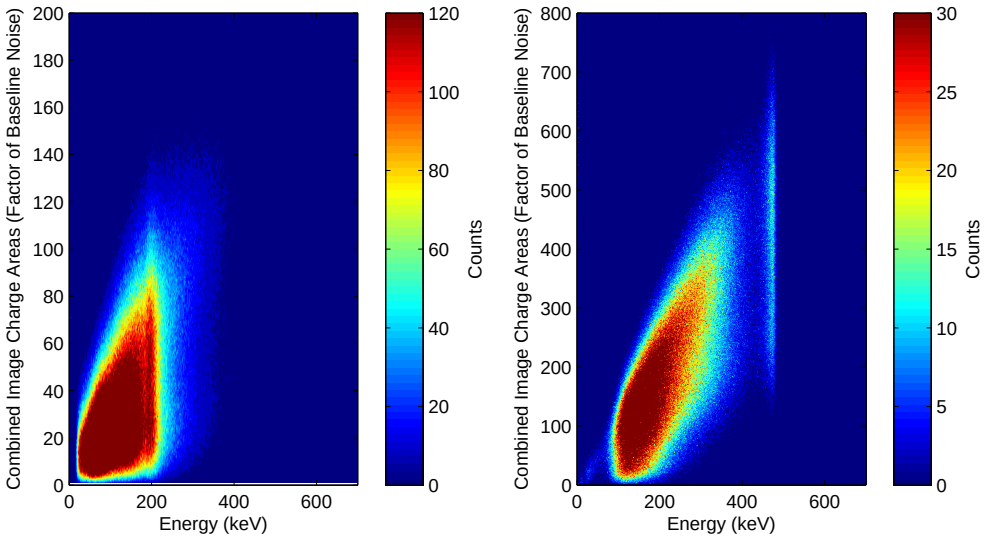

Figure 4.17: Sum of left and right image charge magnitudes as a function of energy for the AC sides of the 5 mm scatterer (left) and 20 mm absorber (right) detectors from ^{137}Cs point source data placed 5 cm from the scatterer crystal.

The image charge asymmetry can be studied further by considering the ICA values for all single interaction pulses above the energy threshold on a given side of a crystal. Figure 4.18 shows the collective ICA values for the DC side of the 5 mm scatterer from a ^{137}Cs dataset, though the response shown is typical for individual strips. The ICA values are more likely to be close to 0 as interactions close to the edges of the strips can share charge across the strip boundaries; in these cases the event is recorded as a fold 2 event and not considered for Compton imaging. The DC side of the scatterer has been highlighted to show the two larger than expected columns of -1 and -0.9. These are a result of DC12 not being instrumented for these experiments, leading to ICA calculations in DC11 automatically favouring the side towards DC10 as there is no image charge collection on the opposing side. As the ICA values were not related to source position in this case these interactions were rejected. As image charge asymmetry can only be used for strips that have adjacent electrodes the active region in each detector is reduced by 10 mm in x and y in both detectors, while the problems with DC12 reduce it even further in this case.

Once both stages of PSA have been performed the improved positional information is passed to the imaging code. The analysis code retains the ability to produce image files

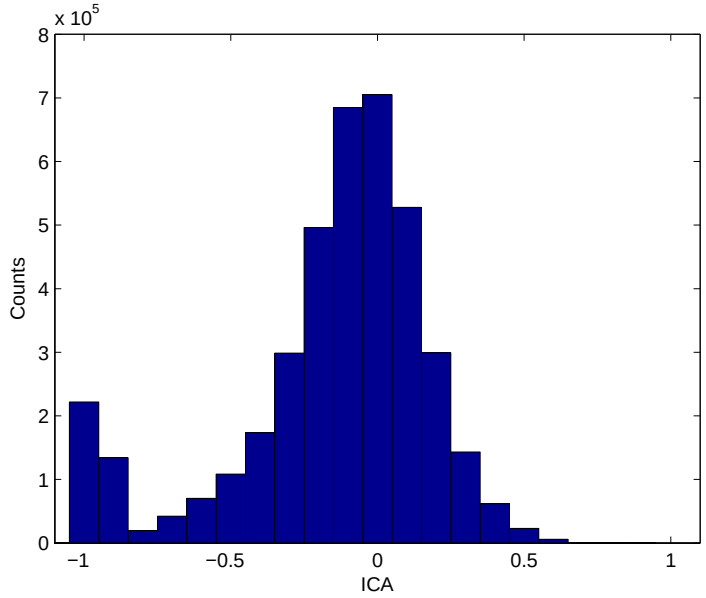

Figure 4.18: Total ICA values from the DC side of the 5 mm scatterer from a full ^{137}Cs dataset.

with and without PSA applied for comparison and six of these are shown in Figure 4.19. All images are produced from ^{137}Cs datasets using only the data from the position +10 mm in x and y from the centre of the detectors. The top two images are from a point source 5 cm from the scatterer crystal, the middle two 10 cm from the scatterer crystal and the bottom two 14 cm from the scatterer crystal (the largest distance this setup would allow). The FWHM values in x and y for each image shown are in Table 4.1. Viewing the images gives the impression that as the source to detector distance is increased the effectiveness of PSA increases and the FWHM values prove this to be the case. This is a logical consequence, as the back projected ellipses from Compton camera events increase in size as distance increases. The interaction positions affect the position and orientation of the ellipses, so improvements in interaction position have a greater effect on them as they increase in size. This leads to improved accuracy in ellipse intersections and ultimately improved resolution in resulting radiometric images. The current source to detector distances are far shorter than those in the eventual decommissioning scenario, so it is expected PSA will provide a huge improvement to the images produced in a practical application. The FWHM values appear to be slightly worse in y than in x for most cases; this has been seen in previous

Compton camera work [87] so may be a result of the reconstruction algorithm as opposed to a specific problem with this experiment. Worth noting also is that in the imaging code used, an intersection is counted if two (or more) ellipses lie across the same pixel. In the 5 mm distance images this pixel size is 1 mm^3 and this leads to higher resolution images, but for longer stand off distances the reduced counts means the number of intersections is drastically reduced. This can be counteracted by compressing phase space into a smaller number of pixels, increasing the chance of intersections and allowing images to be produced with fewer counts. The tradeoff is a reduction in achievable image resolution and a larger error on the fitted resolution. Pixel sizes of 2 mm^3 were used for the 10 mm images and 3 mm^3 pixels were used for the 14 cm image. The reduction in image quality is apparant from the images themselves and this is supported by the larger errors on the Lorentzian fits, but phase space compression is necessary to create accurate, usable images in reasonable timeframes.

Standoff Distance (cm)		No PSA	PSA Applied
5	FWHM x (mm)	14.26 ± 0.97	13.09 ± 0.78
	FWHM y (mm)	13.99 ± 0.79	12.37 ± 0.75
	FWHM x (θ)	15.92 ± 0.27	14.67 ± 0.26
	FWHM y (θ)	15.63 ± 0.23	13.90 ± 0.28
10	FWHM x (mm)	27.98 ± 3.58	23.24 ± 2.56
	FWHM y (mm)	31.49 ± 5.42	17.72 ± 2.86
	FWHM x (θ)	15.69 ± 0.26	13.08 ± 0.27
	FWHM y (θ)	17.48 ± 0.31	10.05 ± 0.52
14	FWHM x (mm)	52.82 ± 12.97	17.89 ± 2.76
	FWHM y (mm)	63.62 ± 8.03	19.21 ± 3.97
	FWHM x (θ)	20.67 ± 0.27	7.28 ± 0.49
	FWHM y (θ)	24.44 ± 0.11	7.81 ± 0.61

Table 4.1: Full Width Half Maximum values of Gaussian fits applied in x and y to the PSA comparison images from Figure 4.19.

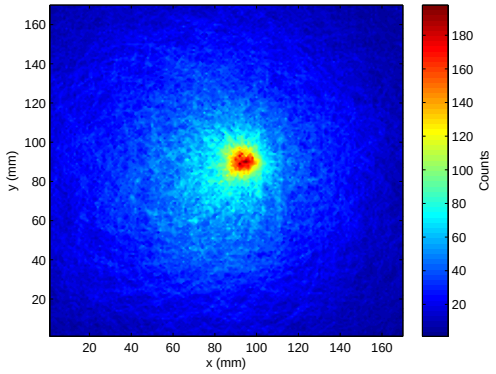

(a) 5 cm from scatterer, no PSA

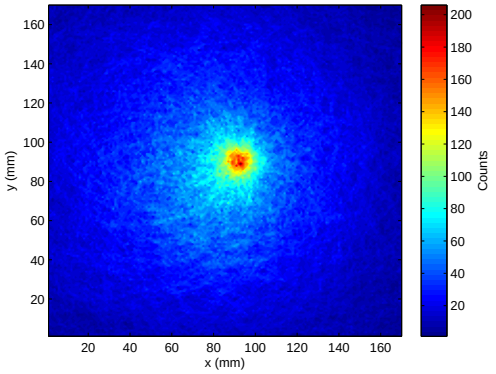

(b) 5 cm from scatterer, PSA applied

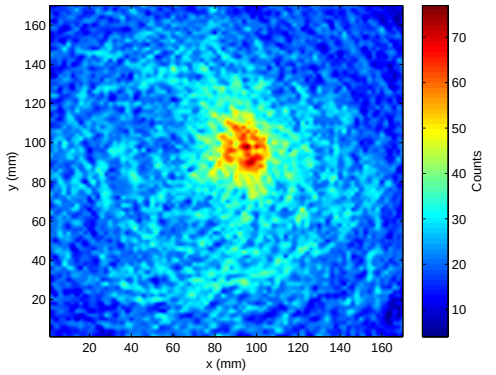

(c) 10 cm from scatterer, no PSA

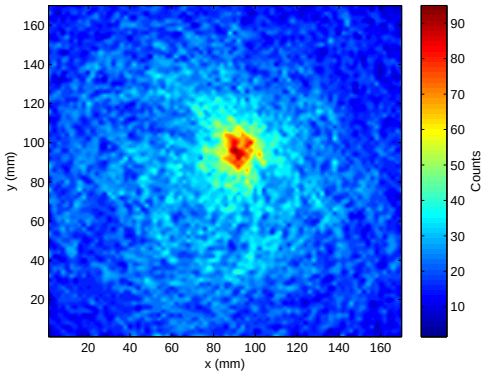

(d) 10 cm from scatterer, PSA applied

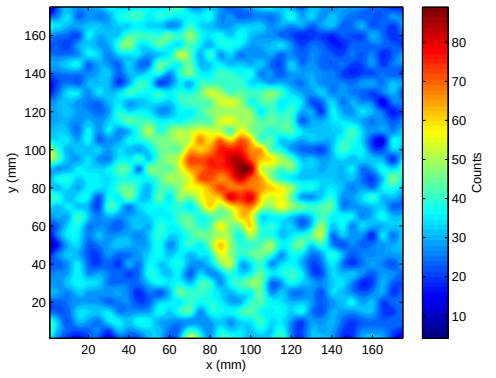

(e) 14 cm from scatterer, no PSA

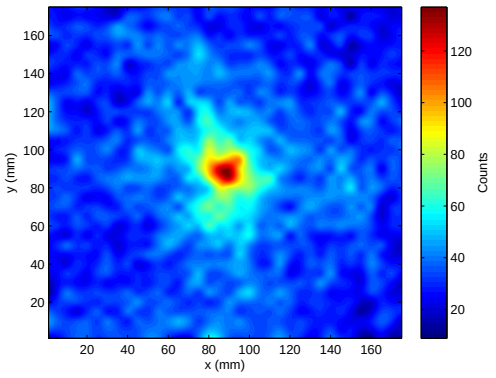

(f) 14 cm from scatterer, PSA applied

Figure 4.19: Images of ^{137}Cs point sources at several distances, with and without PSA applied.

.

The results shown demonstrate the merits of PSA and justify the necessity of implementing it to optimise image quality. However, it has also been qualitatively indicated that the number of rejected events that do not qualify for PSA will have a negative effect on the detector efficiency, as will be quantified later. The depth PSA could be improved by recording pulses at known depths using a collimated beam and collecting scattered gamma-rays in coincidence with a second detector. This would allow t30/t90 values to be measured experimentally as opposed to simply judging likely values as has been applied here. While lateral PSA appears to be working it could likely be improved by keeping noise in the detectors to a minimum and an investigation into ICA values produced from interactions at known locations would help confirm its effectiveness.

Efficiency

As has been touched upon in previous sections the gates required to achieve PSA imaging mean that otherwise image-worthy events are excluded and this has a marked effect on the efficiency of the system. A basic check of the produced energy spectra show an expected distribution of peaks and the drop in counts with each analysis gate is to be expected. Explicit efficiency characterisation of the system was performed alongside a Monte Carlo simulation using the Compton camera functionality of the GAMOS toolkit [88]. The efficiency measurements have been validated using SmartPET data and with the only change between the experiment and this validated simulation being the scatterer thickness its output can be trusted. Unfortunately there is a large discrepancy in the calculated efficiencies between experimental and simulation data as highlighted in figure 4.20, the figure showing absolute efficiency data as a function of energy for a single position dataset 5 mm from the scatterer crystal in depth and 10 mm in x and y from the crystal centre. This accounts to a difference between calculated efficiencies of over a factor of 20. The figure also shows a ^{137}Cs point source measurement 5 cm from the scatterer taken in a following experiment (June 13) that will be presented later in this chapter. This experiment had the same setup but increased the coincidence time window for an interaction in both detectors to be an accepted event from 75 ns to 250 ns. This gave a substantial increase in efficiency but it is still significantly lower than what is predicted by simulation. As noted in Appendix A.1 the count rate of accepted events was lower than expected but it is unclear what has caused

this huge drop in sensitivity; there is no significant pile up in the system but other problems with the CAEN V1724 cards suggest that it was likely something about the electronics that isn't fully understood. This is the first experiment to use the digital trigger so it is possible events are being incorrectly rejected in this case. There is also the discrepancy between events accepted by the trigger but rejected when analysed in the sort code, creating the 'Fold 0' events. To recover these events either the noise must be reduced to ensure true energy deposits are seen as statistically significant or a new approach to determining real charge must be employed. The gradient of the fits is different from experiment to simulation so the energy dependence of efficiency has also changed. Previous work suggests the experimental efficiencies should be similar to simulation and further measurements with this system will clarify whether it was an ADC card problem and if these lost counts can be recovered. It is critical that the Compton camera sensitivity is optimised as if it cannot outperform current systems it is hard to justify its implementation.

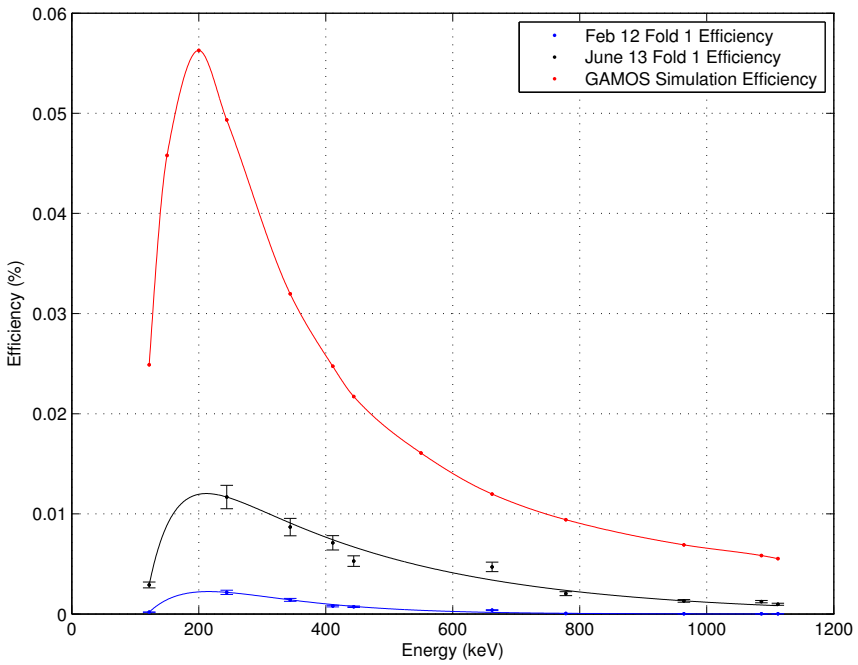

Figure 4.20: Fold 1 absolute efficiency measurements as a function of energy for the February 2012 experiments, June 2013 experiments and GAMOS simulations (5 cm from the scatterer crystal).

While the efficiency information collected may not accurately reflect the potential sensitivity of the system, it can still provide insight into the difference in absolute efficiencies when using PSA imaging techniques. Figure 4.21 shows these efficiencies against the standard Fold 1 imaging approach. Both efficiency curves show a response expected from a Compton camera; the efficiency is largely governed by the Compton scattering cross section, with a sharp rise from 122 keV to 200 keV followed by a typical exponential decrease at higher energies. The figure shows a maximum drop in counts of around 40% between Fold 1 and PSA approaches at energies around 244 keV. This difference reduces significantly as energy increases and beyond 778 keV there is only a negligible decrease in counts from applying PSA. This suggests that at lower energies it is more likely there will be more than one interaction in a single voxel and this follows from the increased interaction cross section at lower energies. The upshot of these results is that at higher energies (beyond 778 keV) PSA should always be applied as it provides improvements in image resolution with little loss in sensitivity. At lower energies in cases where detector sensitivity is more important than image resolution there may still be a place for raw Fold 1 imaging.

Radiometric Image Disparity

Beyond image optimisation, the main focus of these experiments was to quantify the difference between reconstructed and true source location as a function of source position. It is vital that the reconstructed images reflect true radioactive source positions but there was no previous work undertaken to see if this is the case or to quantify any disparity between image and source location. To achieve this each dataset image file was split into the 36 measured positions corresponding to scanning table positions and images were reconstructed using a simple back projection image code [83]. The reconstructed position for each source position was compared to the known true positions. Figure 4.22 shows a comparison of a ^{137}Cs dataset 5 cm in depth from the scatterer in the form of a quiver plot; the arrows start at the true source positions and point towards their respective reconstructed image positions. The point source used in all measurements were encased inside plastic casing and as such their exact position was unknown leading to a possible systematic error in each image. The image positions were all shifted by -3 mm in x and -1 mm in y in software to create this quiver plot on the basis that it gave an expected symmetric response in all direc-

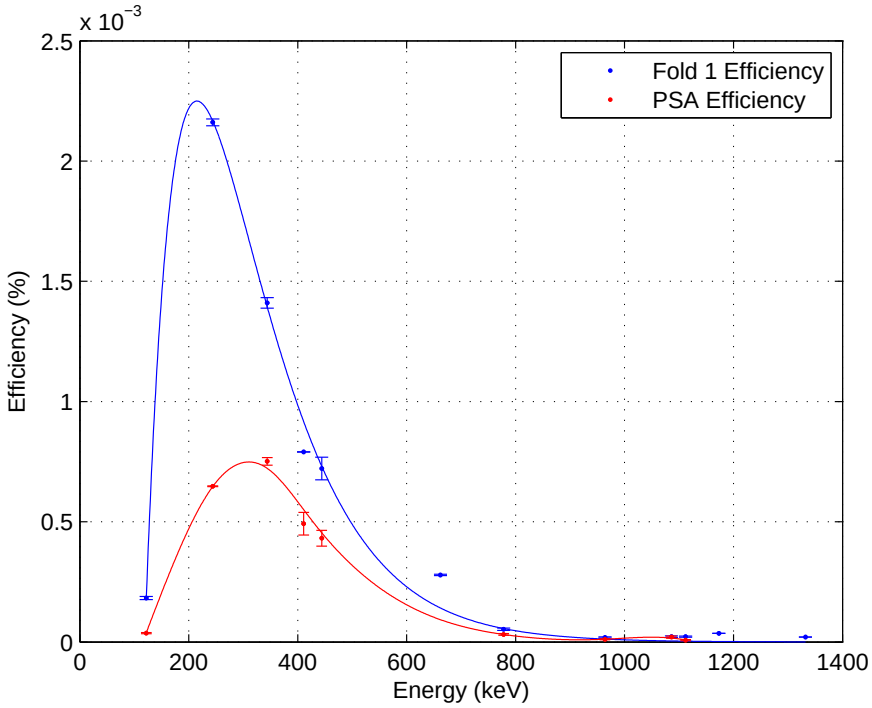

Figure 4.21: Absolute efficiency values of accepted Fold 1 and PSA events for a ^{137}Cs source positioned 10 mm in x and y and 5 mm in depth from the scatterer crystal.

tions of x and y, but while this is likely a systematic error this will only be confirmed with further measurements. The innermost images were reconstructed using around 5500 cones, while the outermost images were reconstructed using around 3300 cones. This resulted in far more accurate fits for the centre images; The FWHM measurements are around 13 mm in x and y for the centre images compared to around 30 mm for the outer images. This discrepancy in counts and resolution could contribute to the discrepancy between experimental and simulated results, something to be considered in future experiments. The figure confirms that there is a disparity between source and image location dependent on source position that must be accounted for and that it is a symmetric radial distortion as found in many computer vision systems [89].

The simulation of the data point grid 5 cm from the scatterer led to the quiver plot shown in Figure 4.23, using raw interaction positions that mimic standard experimental image reconstruction without PSA applied. As can be seen it also displays a symmetric

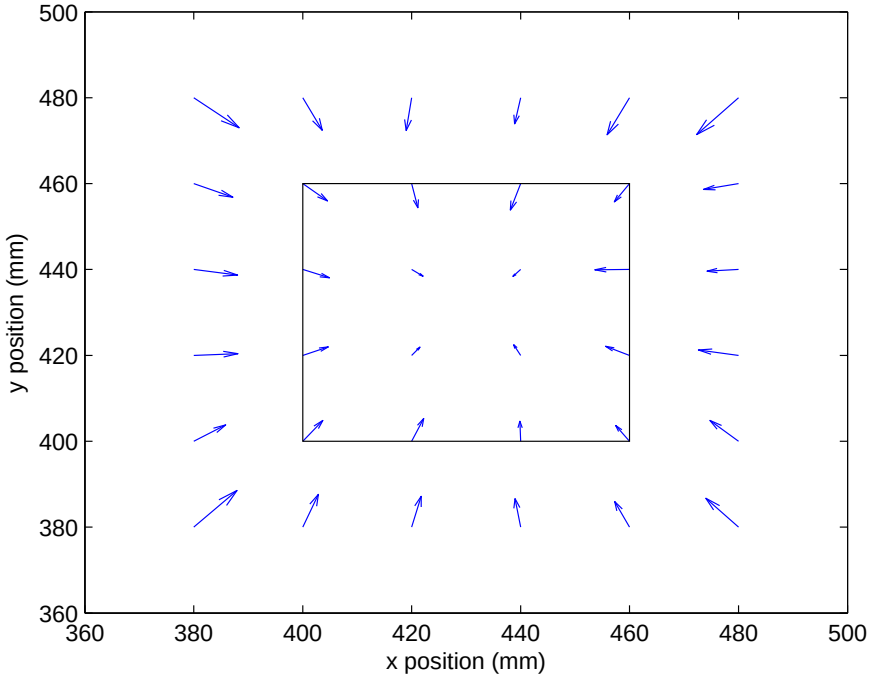

Figure 4.22: Quiver plot showing the direction and difference between the imaged and true source positions for a grid of sources 5 cm from the scatterer in depth. At this close source-to-detector distance there is significant disparity between these positions, particularly for the outer source positions of the grid. The square shows the position of the detector face.

radial distortion but the effect is far less pronounced than that discovered experimentally. While this helps to justify the systematic error added to the experimental dataset in order to create a symmetrical quiver plot, the still significant discrepancy between real and simulated disparity values means the simulations are not currently sufficiently accurate to calculate real world disparities.

It would be beneficial to improve the accuracy of this simulation to the point where the disparity measurements are validated against experimental results, thus allowing disparity values to be confidently reproduced from simulation. The simulation may differ due to an inherent process it uses to simulate Compton camera data or it may be an input error whereby the simulated properties are different to the experiment. While every care was taken to ensure source and detector positions were accurate the placement of the crystal

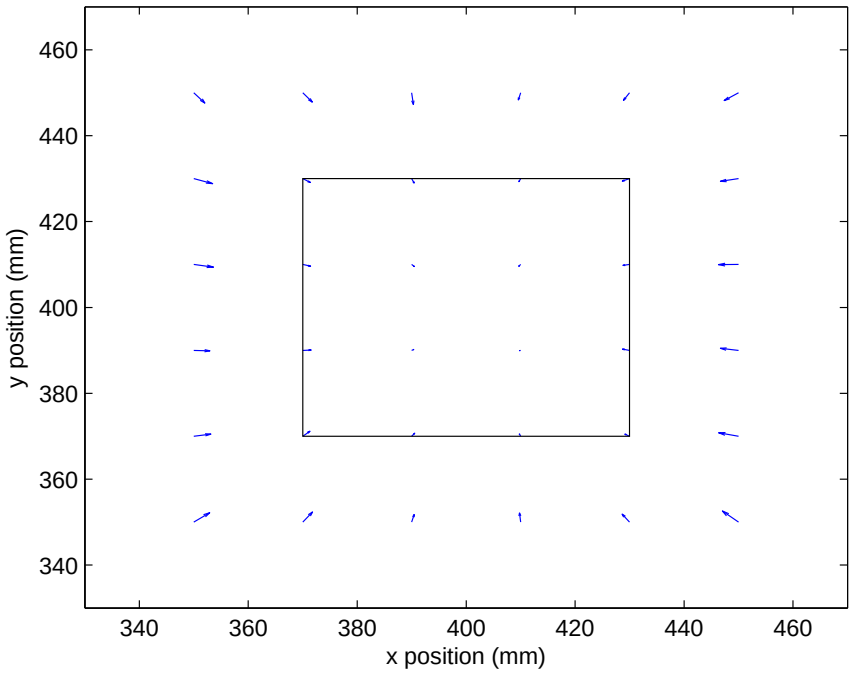

Figure 4.23: Quiver plot showing the direction and difference between the imaged and true source positions for a simulation of grid of data points 5 cm from the scatterer in depth.

in the detector casings cannot be absolutely known and small differences may have a huge effect on simulated results.

To investigate this, further simulations were produced while changing the source standoff and detector separation distances. Figure 4.24 shows two different standoff distances of 3 cm and 1.5 cm (left and right respectively), both significantly smaller than in experiment. The 3 cm distance still shows smaller source-image disparity than experiment in all positions, as such it is unlikely a systematic error on source placement greater than 2 cm is causing the simulation differences. The 1.5 cm quiver plot is shown to highlight the effect that source distance has on image disparity. As can be seen the outer points have a far larger disparity compared to previous measurements while the inner points have barely changed. This is likely due to the fact that the distortion appears to be radial; at outer positions with small source distances the lateral component of the distance between the points and the center of the scatterer will be relatively large and so a change in radius will have a larger effect

laterally. This lateral component changes far less as depth changes for the middle points so little difference is seen in the distortion. Of final note is the top left point as it appears artificially large due to a bad fit of the data.

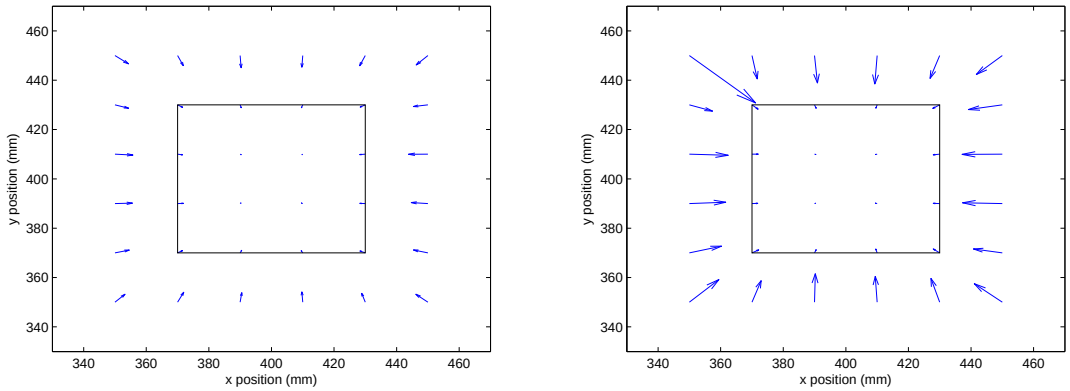

Figure 4.24: Quiver plots showing the direction and difference between the imaged and true source positions for simulations of two grids of data points, 3 cm (left) and 1.5 cm (right) from the scatterer in depth.

Figure 4.25 shows two quiver plots that demonstrate the effect of changing detector separation. The experimental separation is 5 cm, while the left and right images show source-image disparity with a 2.0 cm and 1.0 cm separation respectively. More simulations were processed over a wide range of separation distances but these show that at 2.0 cm there is little change to the disparity compared to the original simulation with a 5 cm detector separation. With a 1.0 cm reduction the right image shows a larger increase in disparity, with a similar magnitude compared to experimental results. There is a disparity increase to all positions and it would least appear that the pattern more closely matches experiment than those achieved by altering source-scatterer distance. This would make detector separation a possible cause of the differences between simulation and experiment but the systematic error required is 3.8 cm, making it unlikely.

To further justify the claim that the distortion is a function of radius, an image disparity quiver plot for a ^{137}Cs dataset 10 cm in depth from the scatterer crystal is shown in Figure 4.26. The increased radius between the source locations and the center of the scatterer detector leads to reduced image disparity, leading to a reduction of the perceived 'pin-

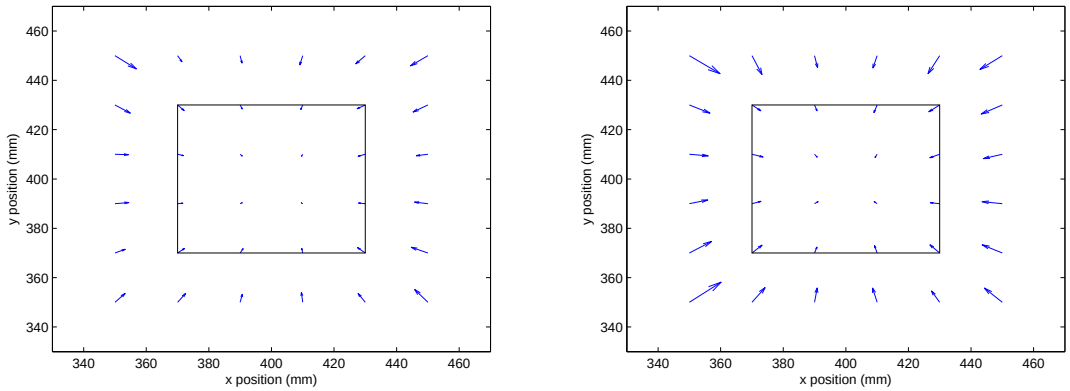

Figure 4.25: Quiver plots showing the direction and difference between the imaged and true source positions for simulations of two grids of data points with detector separation distances of 2.0 cm (left) and 1.0 cm (right).

cushion' effect. As can also be seen, the decrease in image resolution at this larger standoff distance has led to greater uncertainty in the image positions and rendered the 'pin-cushion' effect less defined. Due to DAQ problems the first three data points in the top row are missing but there is still enough data to see the effect.

Now that the radiometric image distortion has been confirmed (to the extent possible from this data), the next step is to attempt to correct it. It is important that the image distortion can be quantified such that images can be corrected mathematically in real time. As noted previously radial distortion is a long standing problem in computer vision and there has been extensive research undertaken to correct it. A simple, widely employed method of correction was developed by Tsai [90] and the application of this technique to the radiometric image distortion was investigated. This method shows that any radial distortion can be approximated using the Taylor expansion

$$\breve{r} = r + k_1 r^3 + k_2 r^5 + k_3 r^7 ..., \tag{4.2}$$

where $\breve{r}$ is the observed radial distance between the origin and the image, r is the actual radial distance and $k_{1,2,3...}$ are *distortion parameters*. For most applications it is sufficient to use only the first three terms (and so two distortion parameters), so to keep calculations

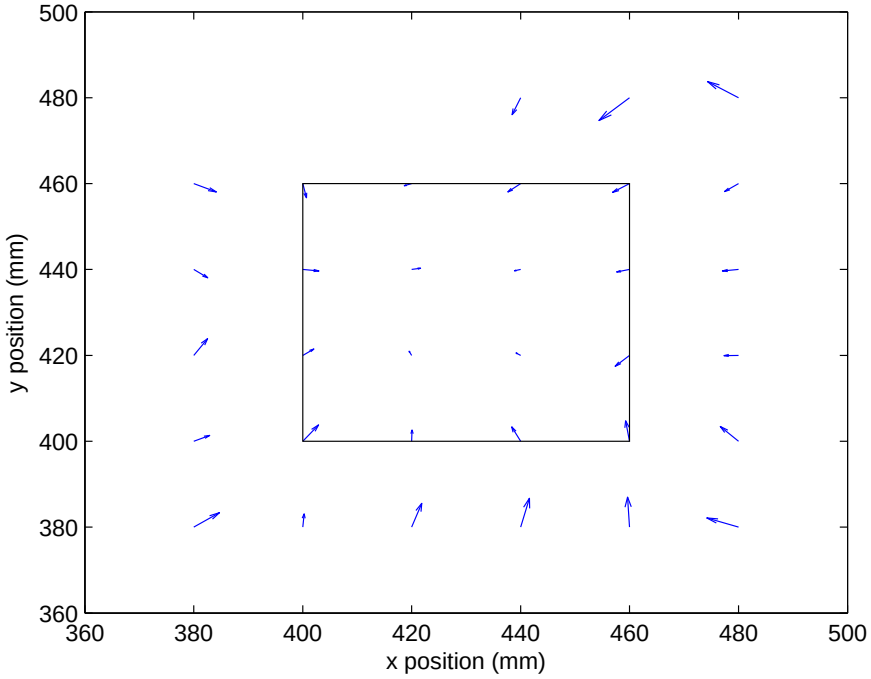

Figure 4.26: Quiver plot showing the direction and difference between the imaged and true source positions for a grid of sources 10 cm from the scatterer in depth. At this increased source-to-detector distance disparity is significantly reduced compared to closer measurements.

and thus computer processing speed to a reasonable timescale this approach was applied. The optimum distortion parameters were found by creating an iterative optimisation script, whereby the difference between image and source positions was measured and the distortion parameters incrementally changed until the parameters that minimised the position differences were found.

Figure 4.27 shows the source and image locations of the grid dataset 5 cm from the scatterer in depth, with the source locations in red and image locations in black. The left plot shows positions before distortion correction is applied, the radial distortion still clearly visible. The blue dot represents the centre of the detectors in x and y which is the radial origin. The distortion correction script was applied to this data and the k_1 and k_2 distortion parameters were successively iteratively optimised until the total difference between source and image locations was minimised. The right plot shows the image location after the

distortion correction has been applied and the images now more accurately reflect the source locations. Unfortunately there are still discrepancies between many of the positions meaning the distortion has not been completely accounted for. This is due to the image resolution causing an error in position co-ordinates that in turn means the image and source locations do not lie on the same radial lines. As this correction is only applied radially the positions can never completely align in this case so there will always be a discrepancy. To reduce this and improve calibration accuracy an increase in statistics is required to improve positional accuracy and as has been discussed these datasets suffered from a lack of statistics. However the data was sufficient to prove the radial distortion of the Compton camera's field of view and show that radial correction is possible.

The distortion parameters yielded for the dataset shown above were

$$k1 = -7.44 \times 10^{-5}, k2 = 8.09 \times 10^{-9}, \theta = 1.59\, mm, \tag{4.3}$$

where θ is the average difference in respective corrected and known positions, essentially the standard deviation. θ provides a good measure of how well the distortion correction is performing; as statistics improve the error in the measured source positions should reduce and θ should also. It is likely this can provide an indication of the confidence to which the distortion correction can be trusted; without any radial correction θ is 42.4 mm so this method currently improves average reconstructed image positioning by over a factor of 26. As there are still large discrepancies between many of the positions it would seem likely that the value 1.59 could be greatly improved upon.

The correction above treats each position equally, trying to create the closest average match for all positions. The middle positions have far greater statistics and consequently there is a far greater accuracy on these image locations. By weighting the matching algorithm so it seeks to make closer matches for images that have smaller position errors the resulting distortion parameters should be more accurate. This method of distortion correction is shown in Figure 4.28 with the image position points now displaying error bars.

The distortion parameters calculated when taking errors into account are

$$k1 = -8.73 \times 10^{-5}, k2 = 1.09 \times 10^{-8}, \theta = 1.62\, mm. \tag{4.4}$$

The θ value has increased slightly but this is to be expected as by focusing on the

positions with the smaller errors there are going to be much larger discrepancies for the positions with larger errors. While it is important to include these errors as they should lead to a better distortion correction in future distortion experiments all position errors should be kept to a minimum by collecting a significant number of counts for each position ($>$ 10000 cones per image would be a safe number, based on observed imaged quality compared to the number of cones used to generate them).

Applying the same approach to a simulation of this work yielded more accurate distortion correction, as can be seen in Figure 4.29. As the simulations contained similar counts to those that hope to be achieved by the experimental system it is hoped that similar distortion correction will be experimentally achievable in the future. The distortion parameters for the simulation were

$$k1 = -1.50 \times 10^{-5}, k2 = 1.09 \times 10^{-9}, \theta = 0.63. \tag{4.5}$$

The standard deviation between positions is far smaller than in the experimental results and both distortion parameters are smaller. This is probably affected by the fact that source position can be controlled with complete accuracy in simulations and the greater number of counts has led to improved position resolution. Even taking these differences into account the simulation images seem far less distorted than the respective experimental images and it may be a feature of the simulation that requires further investigation to give a more accurate reflection of experimental results.

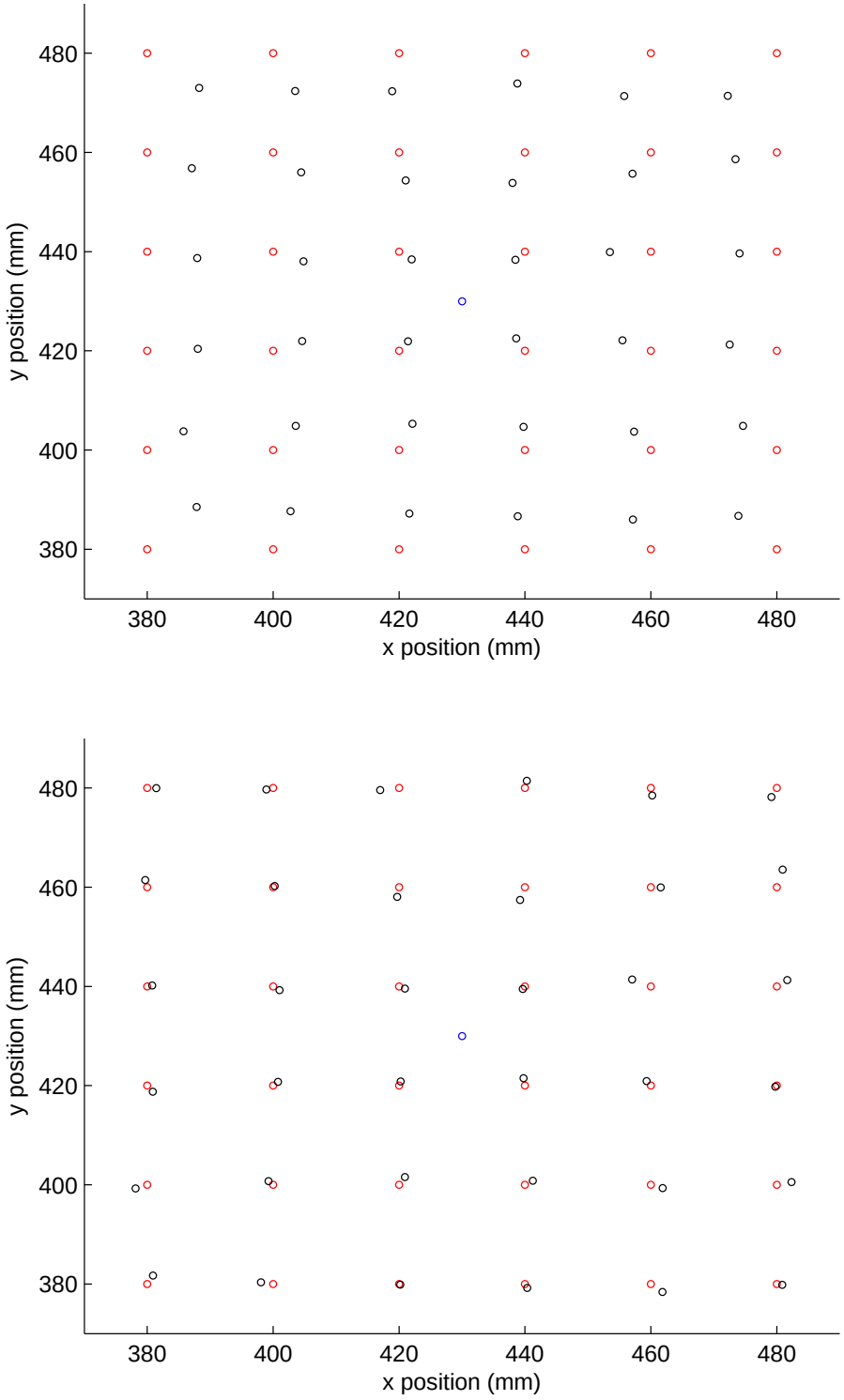

Figure 4.27: Scatter plot of source locations (red) and experimental image locations (black) with and without radial distortion correction applied (right and left respectively), 5 cm from the scatterer crystal.

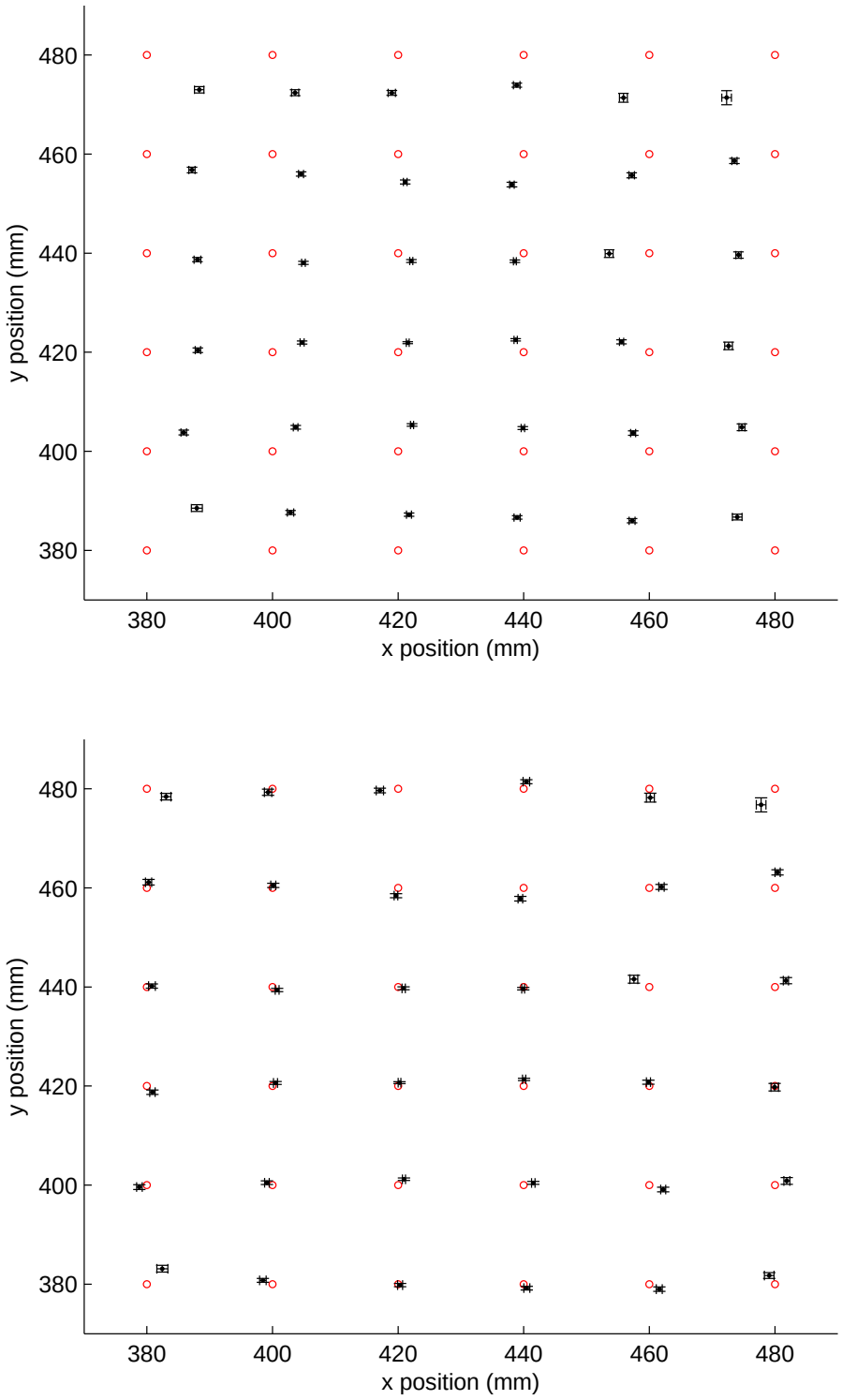

Figure 4.28: Scatter plot of source locations (red) and experimental image locations (black) with and without weighted radial distortion correction applied (right and left respectively), 5 cm from the scatterer crystal.

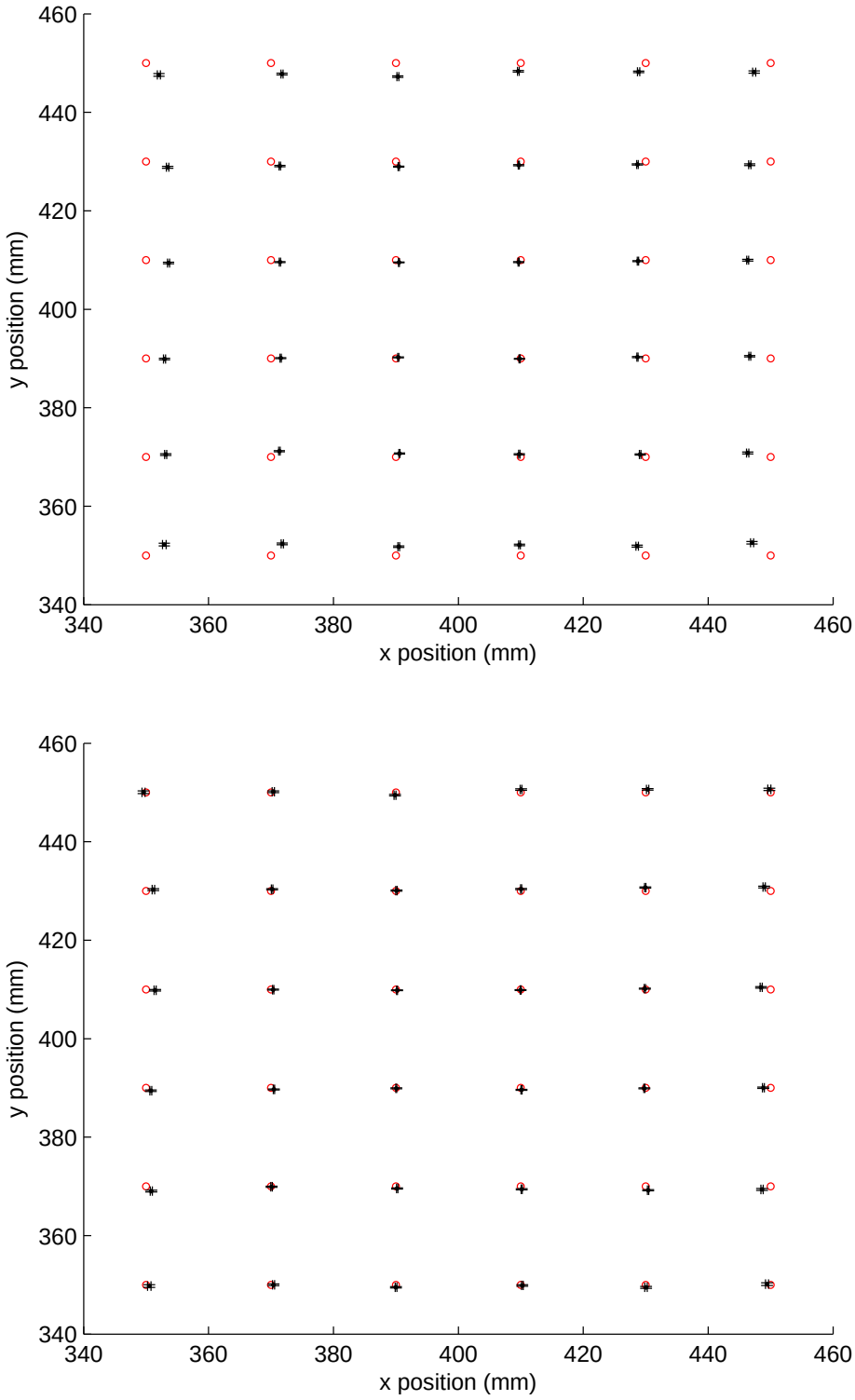

Figure 4.29: Scatter plot of source locations (red) and simulation image locations (black) with and without radial distortion correction applied (right and left respectively).

4.2 Radiometric and Stereoscopic Fusion

Having ensured that it will be possible to faithfully represent gamma-ray source locations using Compton camera images, the experimental focus was to create fused radiometric and stereoscopic images. As radiometric images have already been shown to be producible, initial work concentrated on the setup of the stereoscopic system. While the camera and its associated algorithms are proprietary it was important to ensure the camera performed as expected and the algorithms could be easily implemented to generate the desired images. Once this was assured, experimental measurements at increased distances could be collected and the first fused images created that would be indicative of the ultimate functionality of the fused system.

4.2.1 Initial Stereoscopic Camera Tests

The Bumblebee XB3 arrived with a PCI card and 4.5 metre cable for connection to a controlling PC. Once installed and connected the stereoscopic camera powered up without problems (as shown in Figure 4.30) and was ready for image grabbing tests. While Point Grey provide more comprehensive support for Windows based developments, their cameras can still be used in a Linux environment and as the radiometric Digital Acquisition software is Linux based it followed that the stereoscopic applications should also be developed on this platform.

The camera is controlled by harnessing the C++ libdc1394 libraries that allow for basic control of IEEE 1394 based cameras (such as the Bumblebee XB3). This allows raw images to be captured and passed to the Triclops stereo libraries, algorithms provided by Point Grey that perform the camera calibration, image rectification and stereo matching. Camera calibration allows the path of rays used in depth extraction to be correctly projected and results in rectified images free of distortion, as shown in Figure 4.31. As can be seen images at each stage of stereo processing are accessible.

Once rectified the Sum of Absolute Differences stereo matching algorithm (as explained in Chapter 3.3.1) is applied along with further proprietary validation methods to ensure the generated depth maps are as accurate as possible. Figure 4.32 shows a rectified image and the resulting generated depth map that conveys many of the features of stereo matching. The images show a man holding a paper ball in a laboratory environment. The depth

Figure 4.30: The Bumblebee XB3 stereoscopic camera.

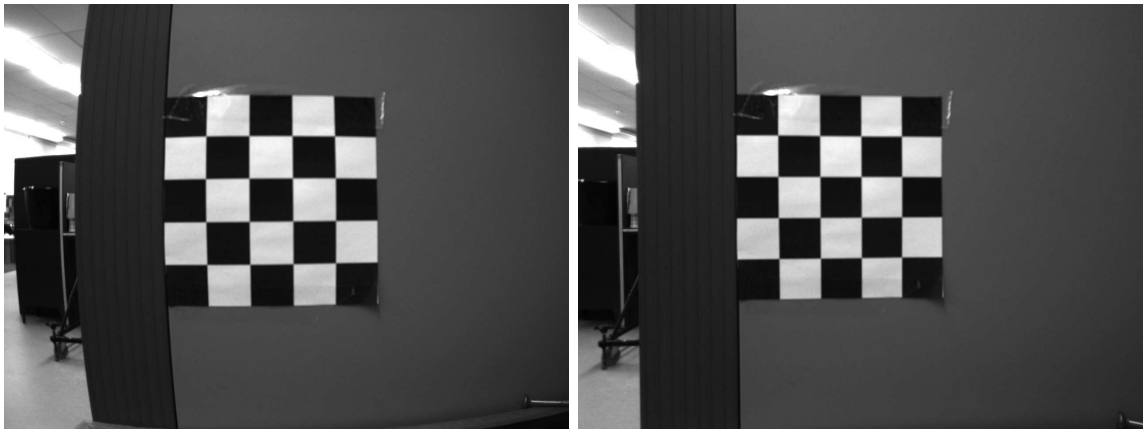

Figure 4.31: An image before and after rectification, left and right respectively. The radial distortion apparent in the first image is corrected in the second and the straight lines now appear so.

image has a black and white colour scheme where lighter objects are closer to the camera and darker objects are further away. The most well defined objects are those of complex shape such as the paper ball and the man's torso; this is due to the fact that these objects are unique and so their pixels are easier to match between the two cameras. These are in

contrast to the less distinct objects in the images such as the computer monitor and the cupboards that are only visible due to their distinct edges. They are single coloured and without any notable patterns or textures making a given pixel indistinguishable from any other, while their edges are unique and can thus be matched. Using the rectified and depth images it is simple to pick out the depth of each object but the difficulty in matching plain objects may have to be addressed if this causes a problem locating radioactive waste in practice. From the depth image x, y and z coordinates can be extracted for each pixel.

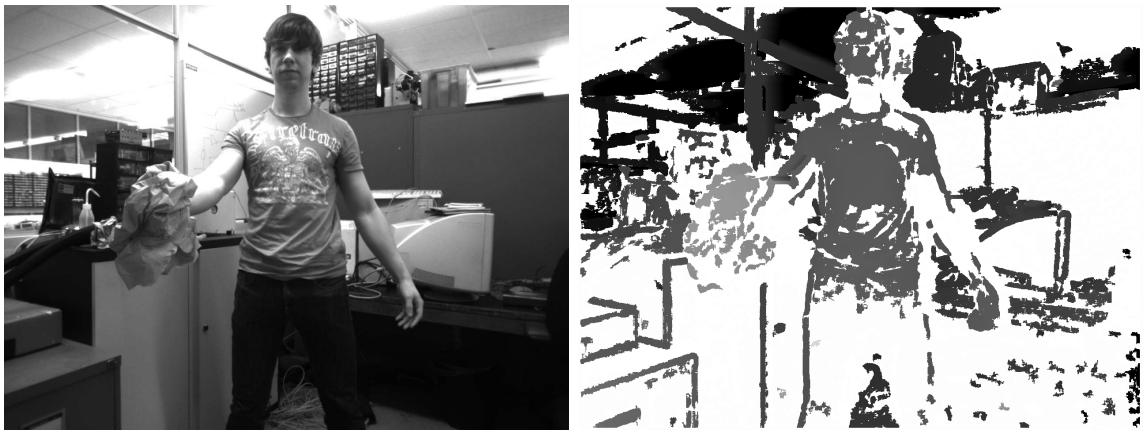

Figure 4.32: A rectified image and its corresponding depth map, left and right respectively. Complex objects and edges are well defined where contrast is high, bland surfaces are not.

As this section shows, the camera is in full working order and can produce the necessary images that provide positional information of objects in a given environment. The next step was to take radiometric data at increased standoff distances that mimic the imaging that will eventually take place at nuclear decommissioning sites. Taking depth images with objects at identical distances to the imaged gamma-ray sources will allow fused images to be created that prove the concept of offline radiometric and stereoscopic image fusion.

4.2.2 Compton Camera Experiments: June 2013

As aforementioned, the goal of the June 2013 Compton camera experiments was to create the first experimental radiometric and stereoscopic fused images. To give the best conceptual proof of the fused image system without site tests it was important to image the strongest sources available in the laboratory environment. In this case this was a 20 MBq

^{137}Cs point source typically used to produce a collimated beam for Compton scattering teaching experiments. The imaging standoff distances would also have to be as large as reasonably practical given the time to collect enough data to create usable images from a source of this strength. These were chosen to be between 0.8 - 1.5 m, distances that could be accurately determined by the stereoscopic camera. These measurements represent the strongest activities and largest standoff distances ever imaged by the Liverpool Imaging group.

The detector setup of this experiment largely mirrors that of the February 2012 experiments (Section 4.1.1). The same planar HPGe detectors were used with an identical electronics setup, but in this case the Compton camera was not mounted above the scanning table but instead housed in a custom built gantry as shown in Figure 4.33. The scanning table allows for datasets accurately separated in x and y, but this was not required for this experiment so the gantry could be used that makes the delicate task of aligning the detectors much easier. This figure also shows the stereoscopic camera mounted on top of the scatterer and the lead housing that holds the radioactive source to be imaged. Mounting the stereoscopic camera on the scatterer was the most practical solution to combining the two cameras as it kept the offset of their respective origins to a minimum, allowing the cameras to share the greatest field of view proportion and keeping the coding required to fuse their respective images as simple as possible. It is worth noting that the coincidence time window had been widened from 75 ns to 250 ns following time resolution measurements made in another Compton camera project using the same DAQ setup and absorber but a different (Si(Li)) scatterer crystal [87]. It was seen that timing resolution between crystal interactions was worse than previously thought and by increasing this time window the efficiency of the system may be increased. Also the energy threshold of the absorber detector was increased to 30 keV (the scatterer threshold remained 7 keV). This is acceptable as it is in the scatterer where small energy deposits are expected and so the threshold must be as low as possible, while the absorber will typically have large energy deposits and so a threshold further from the noise is beneficial. This should give a reduction in random coincidences with a negligible decrease in efficiency.

The lead housing consists of an old coaxial detector housing turned on its side, held in place by two lead blocks and strapping. The strength of the source to be imaged required a

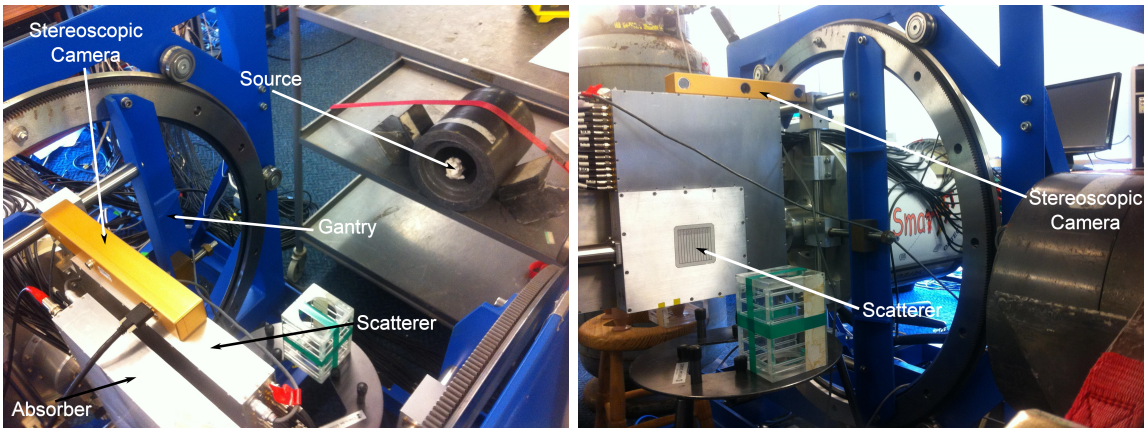

Figure 4.33: Images of the Compton camera setup used in the June 2013 experiments.

strong shielding structure and the housing provided this while not encroaching on the solid angle between the source and detector. The housing was strapped to a trolley so that the distance between detector and source could be easily changed with no alterations to the shielding.

A list of measurements taken alongside detailed source and rate information can be found in Appendix A.2.

Analysis

While the goal of these experiments was to create the first experimental fused radiometric and stereoscopic images, for the project to progress beyond this it was important to develop codes that allowed others to create fused images; with these codes as a starting point future researchers will be able to develop software that fuses data in real time and allows the fused system to be operated by end users with no coding experience. With this in mind the image fusion General User Interface (GUI) was developed in Matlab, incorporating the back-projection algorithms with fusion algorithms that take the processed radiometric images and correctly fuse them with chosen stereoscopic images. The Matlab environment was chosen to develop this GUI as it has powerful image manipulation functions that make fusion quicker and easier to process. It is also cross platform (Windows, Linux and Mac) making it easier for end users to eventually setup and use the GUI. The prominent features of the software are explained below, alongside the specific challenges faced whilst developing

it.

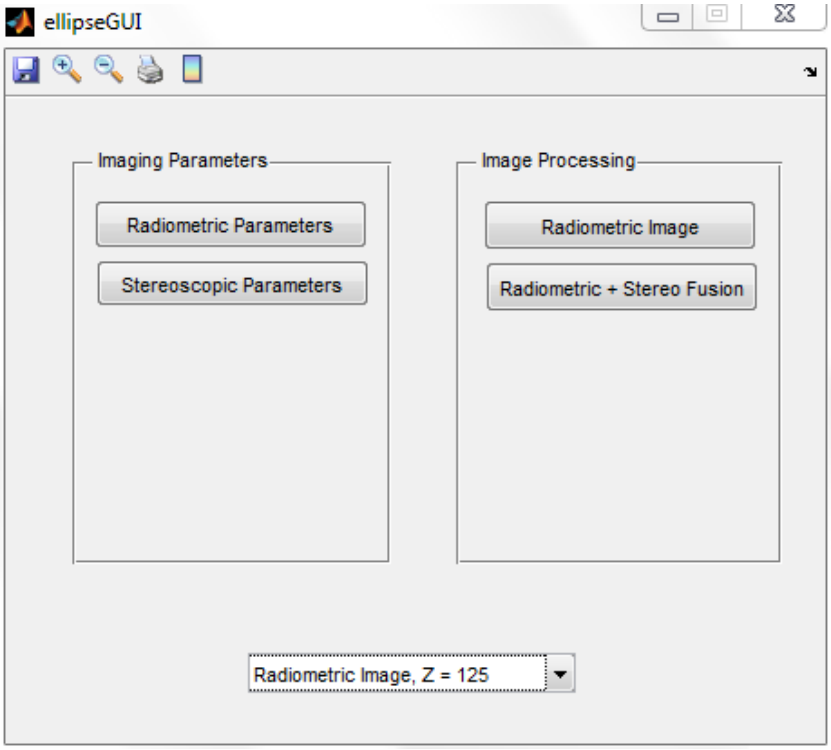

Figure 4.34: The Matlab image fusion GUI.

The main menu of the image fusion GUI is shown in Figure 4.34. It is a small program that has four buttons: two to enter parameters for the radiometric and stereoscopic data and two to process the respective images. The radiometric parameters can be seen in Figure 4.35 and it is clear that many of the features of the original radiometric imaging program have been incorporated. The program processes the interaction positions and energy deposits in each Compton camera detector to generate cones and it is possible to set energy gates, interaction gates, control the number of events processed and more. The image processing is handled using a C++ code incorporated into the Matlab environment (this is known as a MEX file); C++ is far more efficient at processing programming loops and by doing so processing speed is drastically improved to a comparable level with the original program. It takes less than 5 seconds to process 5000 events using this method, while processing exclusively in Matlab takes around 50 seconds. Comparing the output the Matlab code to

the orginal C++ code shows a nearly identical response. There are small discrepancies in fit values but this is probably due to slightly different approaches to fitting functions between ROOT and Matlab.

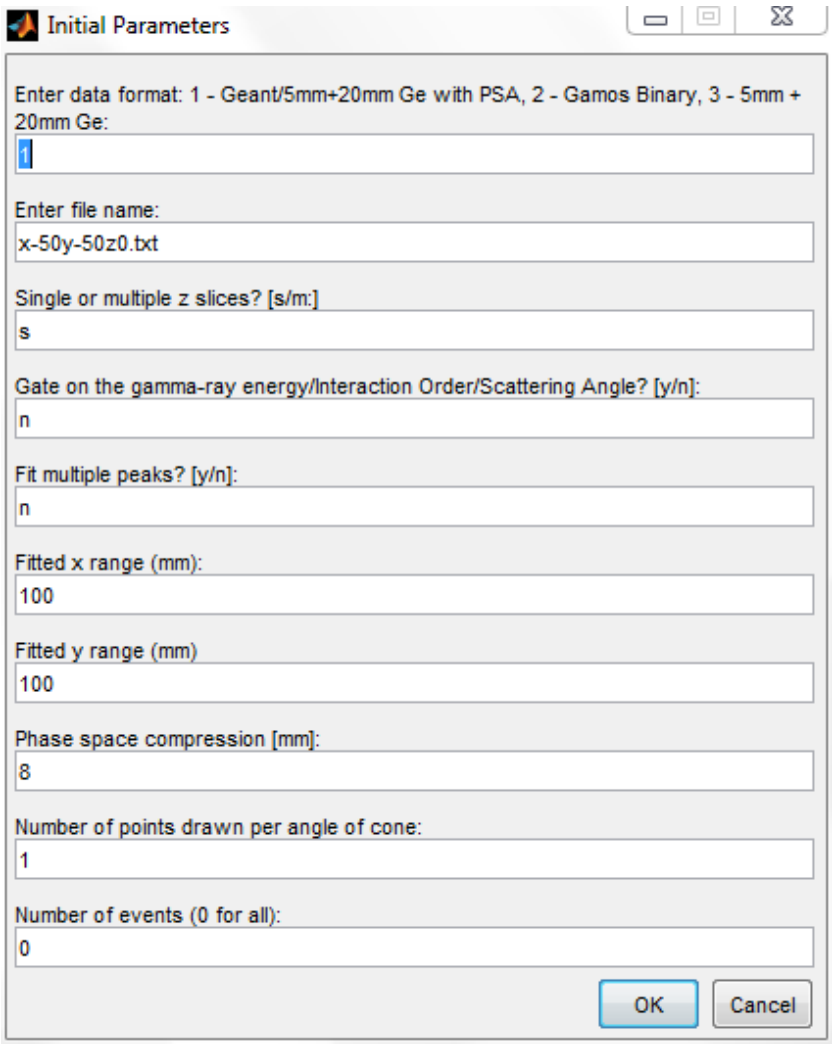

Figure 4.35: The parameters menu of the Matlab image fusion GUI.

The original code used the ROOT toolkit [84] to create its figures, a powerful set of C++ libraries that are heavily used in particle physics data analysis. Matlab has its own methods for displaying data that have been exploited for use in the image fusion GUI and Figure 4.36 illustrates an example of these. It is simple to create and align multiple figures

allowing the radiometric image to be displayed alongside 2D fits of the maximum value, displaying a great deal more information than the image alone. The Figure displays the image of a ^{137}Cs point source 1 m from the scatterer crystal without PSA applied and the source is clearly visible, though the resolution has significantly decreased compared to images of closer sources. Even so, this image demonstrates the Compton camera's ability to image sources at the kind of standoff distances required for use in nuclear decommissioning.

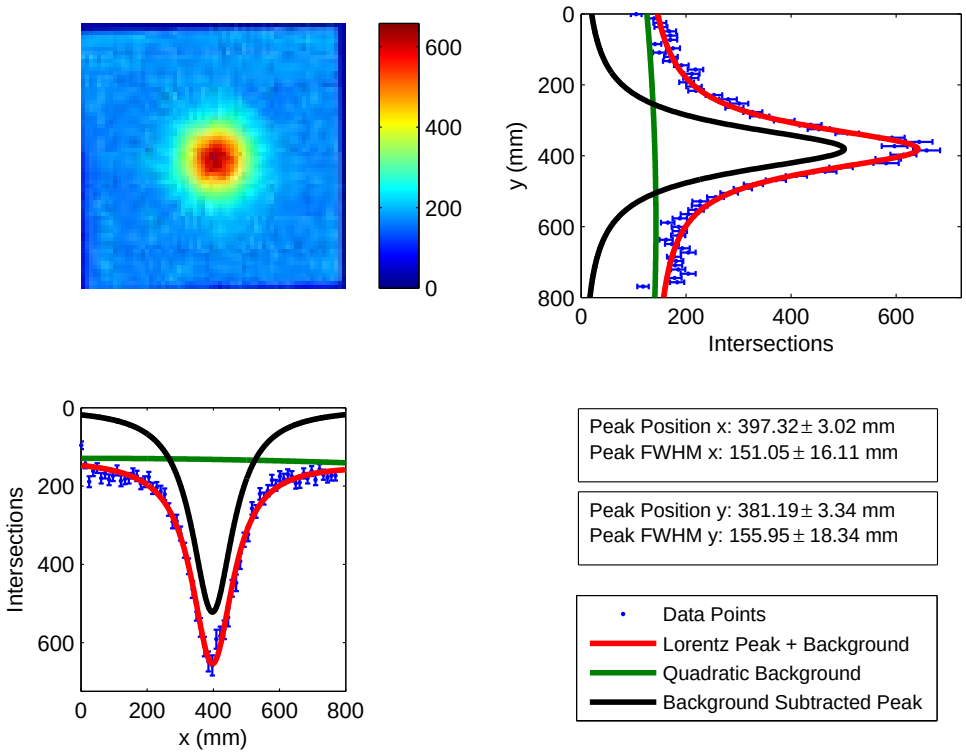

Figure 4.36: A radiometric image of a ^{137}Cs point source 1 m from the scatterer crystal, with x and y fits of 2D slices through the maximum value. Created using the image fusion GUI.

As the radiometric images can be correctly produced, the next step is to fuse these images with stereoscopic data. The stereoscopic images are collected by the Bumblebee XB3 and these are manually loaded by the GUI user into Matlab. Matlab has extensive image processing and camera control libraries so the project will likely gear towards developing an interface in Matlab that can directly communicate with the stereoscopic camera. This

will lead to the potential implementation of a stereoscopic video stream that can be used with radiometric data collected in real time.

The only other parameters required by the user are the co-ordinates of the stereoscopic camera in relation to the Compton camera, but it is vital that these are measured correctly. The GUI uses these to fuse the images in the correct positions; any error in the camera offsets will result in an error in the resulting images. The offsets are measured from the centre of the right camera sensor in the stereoscopic camera to the centre of the Compton camera's scatterer crystal and for this experiment were 0.000 m in x, −0.314 m in y and −0.030 m in z.

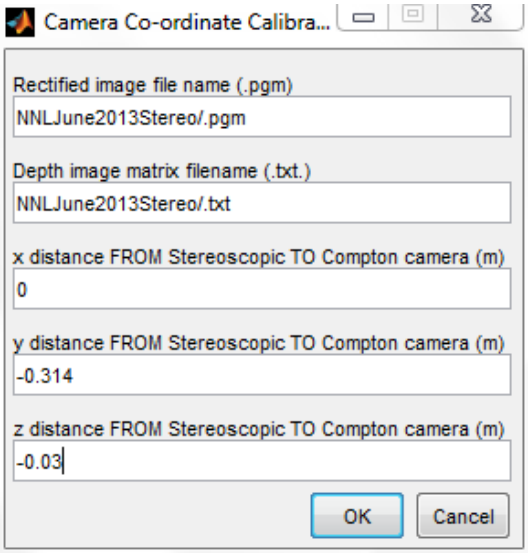

Figure 4.37: The stereo parameters menu of the Matlab image fusion GUI.

Once the stereoscopic images and parameters have been entered, image fusion can begin. The biggest challenge is ensuring the pixels of both images are of the same dimensions; once this is achieved the images can be simply overlapped but the size of the stereoscopic pixels changes with respect to depth. As depth increases the camera's field of view increases but the number of pixels remains the same, so it stands to reason that a pixel in an image will represent a greater dimension as the object in the image moves further away. Mathematically this can be represented as

$$x = \frac{uz}{f} \tag{4.6}$$

and

$$y = \frac{vz}{f} \tag{4.7}$$

where u and v are the pixel dimensions in the 2D image, x, y and z give the real 3D coordinates and f is the focal point of the camera [91]. To calculate the dimensions of one pixel in either dimension u and v are 1 and can be omitted from the equation. The pixel dimensions in the radiometric image are user-controlled and correspond to the size of the bins on the 2D matrix the projected cones are drawn on to. Larger radiometric bins means there will be a greater number of cone intersections and more counts in an image, but the cones will be less accurately defined and the resulting image resolution poorer. It is currently a user defined choice to decide the pixel size that gives the best tradeoff between image counts and resolution, but future research may lead to an automated pixel decision based on the pixel size needed to reduce the chi-squared fit values below a given value. This means that the ratio between stereoscopic and radiometric image pixels can be calculated by

$$Pixel\ Ratio = C\,\frac{f}{z}, \tag{4.8}$$

where C is the dimensions of the radiometric pixel (often referred to as the phase space compression). Matlab has a useful image resize function (imresize) that takes an image matrix and enlarges it by a given factor, interpolating between data points to fill any empty spaces. Resizing the radiometric image using the pixel ratio ensures the pixels in both images are now the same size for a given depth of interest. Using Equation 4.6 and 4.7 the correct pixel shift in the image from the offset of the cameras can also be calculated.

The first experimental fused radiometric and stereoscopic images are shown in Figure 4.38. As well as the steps explained above, the radiometric image has been subject to a linear background subtraction as fusing the background counts unnecessarily hides sections of the stereoscopic image. On the computer, the cursor returns the depth value in a given pixel and using Equation 4.6 and 4.7 true x and y coordinates are also displayed. The

radiometric counts in a chosen pixel are also displayed, though these are interpolated so the number in a given pixel may just be a fit between the nearest pixels as opposed to a true measurement.

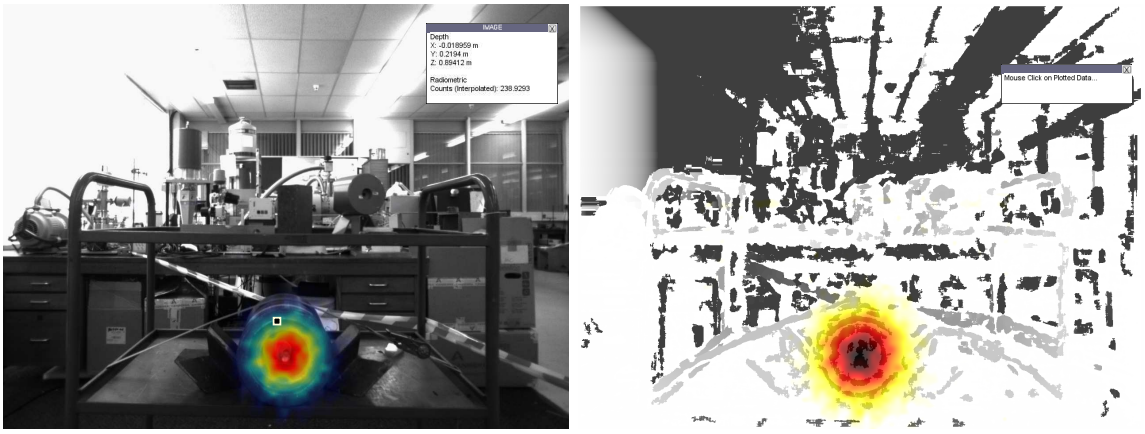

Figure 4.38: Fused radiometric and stereoscopic images of a ^{137}Cs point source 1 m from the scatterer crystal.

Data at distances of 80 cm and 1.5 m was also collected and their fused images are shown in Figures 4.39 and 4.40. The 1.5 m standoff distance represents the longest distance ever imaged using a Compton camera in the University of Liverpool's laboratory environment.

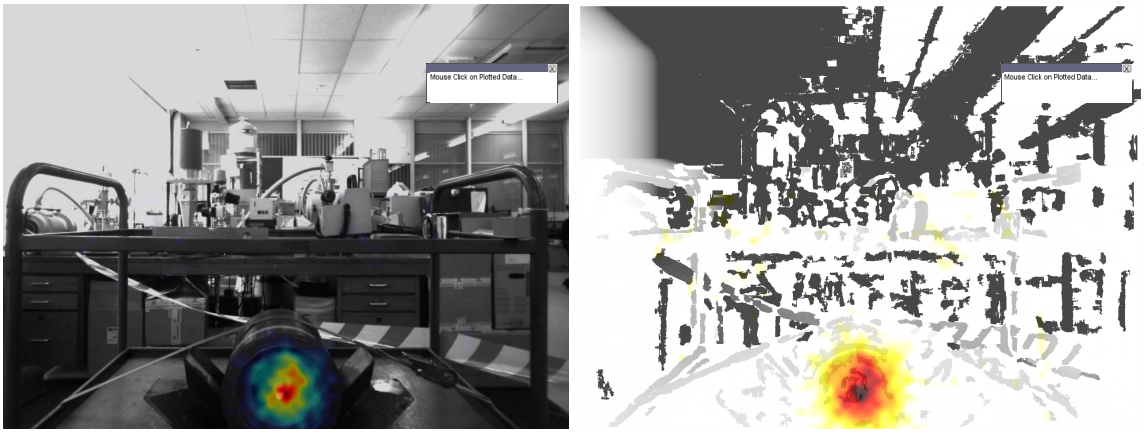

Figure 4.39: Fused radiometric and stereoscopic images of a ^{137}Cs point source 80 cm from the scatterer crystal.

Figure 4.40: Fused radiometric and stereoscopic images of a ^{137}Cs point source 1.5 m from the scatterer crystal.

Distance From Scatterer (cm)	FWHM x (mm)	FWHM y (mm)	FWHM x (θ)	FWHM y (θ)
80	100.57 ± 10.02	136.81 ± 12.25	7.17 ± 0.06	9.70 ± 0.04
100	163.65 ± 6.61	169.07 ± 7.93	9.29 ± 0.01	9.60 ± 0.02
150	277.61 ± 23.15	271.61 ± 23.15	10.49 ± 0.02	10.26 ± 0.02

Table 4.2: Full Width Half Maximum values of Gaussian fits applied in x and y to the radiometric images from Figures 4.38, 4.39 and 4.40.

The resolution of the radiometric images from the figures above are shown in Table 4.2. These images were created using standard Fold(1,1,1,1) events with raw interaction positions. It is worth noting that the stereoscopic information accurately locates the physical radioactive source object; for example the 1 m source distance is measured by the camera as 0.984 m, where the 0.116 m difference could be due to systematic error as it was measured by hand. Furthermore the radiometric images correctly overlap this physical object thus proving that calibrating the position differences between the two detectors is sufficient to ensure the images are fused correctly. Applying Pulse Shape Analysis to the images should give an improvement in image resolution and with the large number of datasets collected at a range of positions for this experiment, the potential improvement of using PSA could be more thoroughly investigated.

Pulse Shape Analysis

Pulse shape analysis was previously shown to give an improvement in radiometric image resolution when applied, so it was important to use it in this experiment to give the highest quality fused images. As mentioned in the previous pulse shape analysis section, the t30/t90 gates were chosen by eye and while PSA as a whole was shown to improve image resolution this is not enough to prove these gates were correct. Before applying PSA to the fusion data a quick investigation was carried out using the image disparity data to determine the relative contribution to image resolution of depth and lateral PSA. Table 4.3 compares image resolution values from ^{137}Cs point source images reconstructed using both PSA approaches. The source is positioned 5 cm from the scatterer crystal and it is readily apparent that while the image charge PSA improves image resolution, depth PSA degrades it. As there were previous concerns about the choice of t30/t90 gates when deducing interaction positions, it was hoped more detailed consideration of these gates could correct the problems of depth PSA and lead to improved image resolution.

	FWHM x (mm)	FWHM y (mm)
All PSA	13.10 ± 1.05	12.37 ± 0.75
Depth PSA Only	17.55 ± 1.09	15.85 ± 0.92
Image Charge PSA Only	12.95 ± 0.66	12.20 ± 0.79

Table 4.3: Comparison of PSA approaches applied to ^{137}Cs point source data positioned 5 cm from the scatterer crystal in depth.

For the 20 mm scatterer there was greater scope for investigation as a dataset containing pulses of known interaction positions has been created [86]. Figure 4.41 shows traces at 1 mm positions through depth beside their respective t30/t90 values.

The obvious mistake made in previous gates was the decision to use the t30 values as the primary basis for deciding interaction position; as the figure shows the first four positions have very similar t30 values and this was previously assumed to encompass a single interaction position. The gates must follow the tick shape and to this end it is not viable to use simple rectangle gates, more complex shapes are required to split the t30/t90 values into correct interaction positions. The left plot of Figure 4.42 shows the experimental

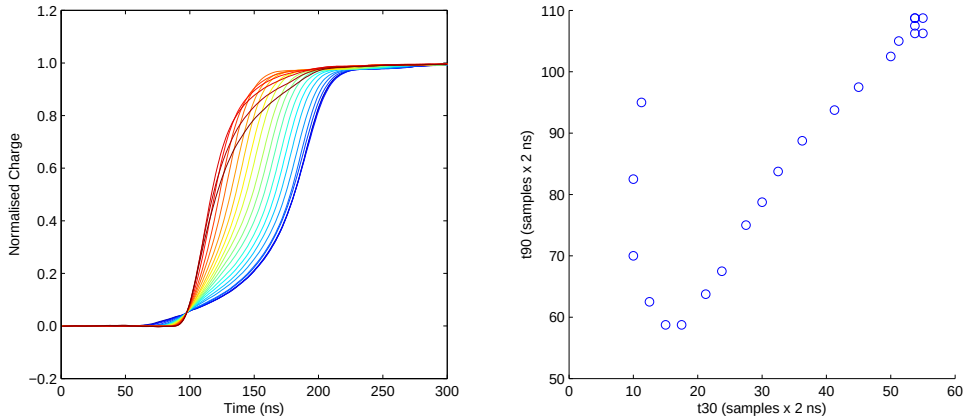

Figure 4.41: Traces from known interaction positions through depth in the 20 mm absorber detector (left), t30/t90 values of the respective interaction positions (right).

t30/t90 values measured in this work with the known interaction position values from [86] overlaid as black circles. There are slight discrepancies between the two datasets, this may be due to the fact that the known position values were recorded from the centre of the electrode in x while all x positions are recorded in the experimental values leading to discrepancies. It may also be due to changes in detector response over time and the change in digitizers used between experiments. Because of this the gates could not be based on the exact t30/t90 values from the known positions but instead be made to follow a similar trend. The polygon gates are marked in white and as can be seen are well suited to dividing the complex tick shape.

The right plot of Figure 4.42 shows the t30/t90 values of the AC side of the 5 mm detector. The 5 mm scatterer is much thinner than the absorber and this has a marked effect on the measured t30/t90 values as seen in previous experimental data. As this detector was acquired far more recently than the 20 mm there has not been an opportunity to build a pulse database of known interaction positions so it is more difficult to place accurate t30/t90 gates. The challenge is further increased by the fact that the reduced t30/t90 values have made the expected tick shape response difficult to distinguish. The gates used have attempted to follow an assumed trend but with the small risetime values and 2.5 ns the gates are hard to trust. It was expected that the shape of these gates would be an improvement on the previous approach and an improvement in image resolution would

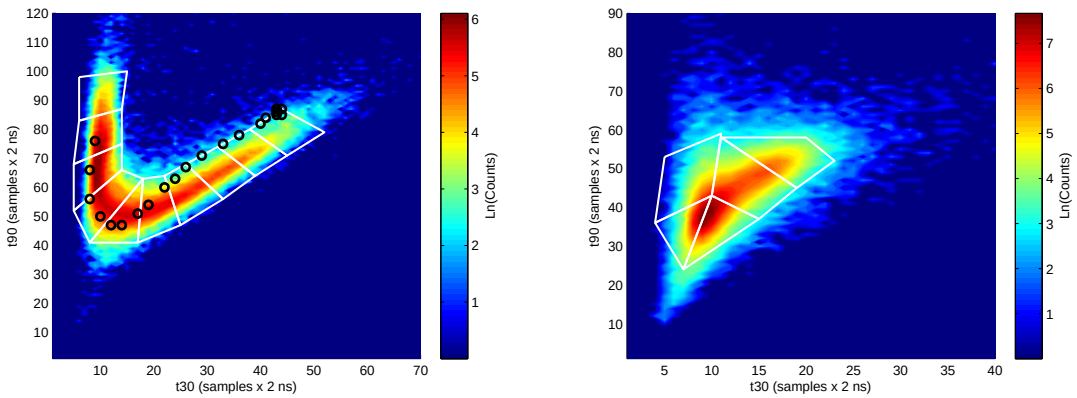

Figure 4.42: A plot of t30 against t90 values for the 20 mm absorber detector, with previously recorded known t30/t90 values overlaid as black circles (left) and interaction position gates in white. The same features are shown for the 5 mm scatterer detector but without previous t30/t90 values as there are no previous measurements (right).

justify the change.

Table 4.4 shows the comparison between ^{137}Cs datasets at distances between 5 - 150 cm for a number of PSA configurations. For a given distance the counts are kept constant throughout all images to ensure a direct comparison of PSA effects and the numbers are detailed in Table 4.5. Note that it is the number of 'Energy Gated Cones' that is kept constant throughout each backprojected image to ensure a direct comparison of each PSA approach. While PSA has previously been shown to work for close imaging distances it was of particular interest to see if these improvements continued as standoff distances increased. The new polygon shaped gates were also compared to previous approaches to see their effect on resulting images. The configuration 'Both Polygon Gates' refers to new gates used on the scatterer and the absorber, 'Absorber Polygon Gate' refers to a new gate on the absorber and the original on the scatterer, 'Old Gates' refers to using old gates on both detectors and 'No PSA' means no PSA has been applied to the resulting images.

The important result is that all forms of PSA largely produce images with better resolution than those without PSA applied, consistently so if only the PSA approaches using new polygon gates are considered. This is evident in the smaller FWHM values, reduced errors on those values and higher counts in the largest bin. There is strong evidence that

Distance (cm)		Both Polygon Gates	Absorber Polygon Gate	Old Gates	No PSA
5	FWHM x	11.30 ± 0.34	12.15 ± 0.30	14.07 ± 0.37	13.42 ± 0.32
	FWHM y	11.51 ± 0.29	11.75 ± 0.32	15.97 ± 0.59	13.84 ± 0.48
	Max Counts	666	577	526	645
15	FWHM x	18.22 ± 1.47	22.95 ± 2.26	20.22 ± 1.61	27.23 ± 2.19
	FWHM y	22.24 ± 1.84	23.24 ± 2.46	20.25 ± 2.20	28.97 ± 2.44
	Max Counts	128	95	91	103
25	FWHM x	25.07 ± 2.60	23.55 ± 2.75	33.98 ± 4.03	37.96 ± 4.00
	FWHM y	22.45 ± 2.42	19.13 ± 2.41	31.20 ± 4.35	47.74 ± 6.92
	Max Counts	117	97	88	115
80	FWHM x	67.19 ± 8.79	92.31 ± 12.23	94.89 ± 12.62	93.77 ± 14.30
	FWHM y	96.34 ± 11.98	85.65 ± 13.31	104.25 ± 18.59	162.50 ± 25.62
	Max Counts	117	97	88	115
100	FWHM x	98.66 ± 6.19	122.40 ± 8.89	143.71 ± 11.20	158.44 ± 11.16
	FWHM y	119.61 ± 6.86	120.66 ± 8.16	178.20 ± 16.53	156.29 ± 12.26
	Max Counts	299	242	231	266
150	FWHM x	170.02 ± 12.49	193.39 ± 16.04	258.75 ± 22.90	258.93 ± 20.36
	FWHM y	198.65 ± 12.50	190.98 ± 14.45	251.30 ± 23.92	260.70 ± 22.56
	Max Counts	184	151	135	168

Table 4.4: Full Width Half Maximum values of Lorentzian fits applied in x and y to the PSA comparison images from Figure 4.19. FWHM values are given in mm.

Distance (cm)	5	15	25	100	150
Total Events	299904	238483	144319	1140248	859540
Fold (1,1,1,1) Events	115430	94678	58842	457548	347541
PSA Events	45061	33619	20340	159000	119146
Energy Gated Cones	4665	1367	805	6921	5067

Table 4.5: Counts used in comparison images at each distance detailed in Table 4.4.

Distance (cm)	PSA improvement in x (%)	PSA improvement in y (%)
5	19.2	19.6
15	31.0	25.8
25	40.4	49.5
80	25.9	30.1
100	40.0	29.2
150	23.5	23.0
Average	30.0	29.5

Table 4.6: Counts used in comparison images at each distance detailed in Table 4.4.

the polygon gates on both detectors lead to improved images; there is a general trend of improved resolution as polygon gates are applied (though there are discrepancies) and the highest count bin is always largest when both polygon gates are applied. The improvements in image resolution are highlighted as percentages in Table 4.6 and the angular resolution with and without full polygon gated PSA shown in Table 4.7

As a percentage the improvements vary between 19.2% and 49.5%, with the FWHM in x and y at 25 showing the largest improvements of 40.4% and 49.5% respectively. On average, PSA improves image resolution by 30.0% in x and 29.5% in y. Even the lower limits of image resolution improvement are justification for the implementation of pulse shape analysis and this is supported by the clear visual improvement in resulting fused images. This is also well illustrated in Table 4.7 that shows a PSA image resolution comparison in degrees.

The improvements outlined in the table are easier to comprehend when plotted as shown in Figure 4.43. While the individual points are quite disparate, particularly in the long

Distance (cm)		No PSA	PSA
5	FWHM x	15.02 ± 0.11	12.74 ± 0.15
	FWHM y	15.47 ± 0.14	12.96 ± 0.12
15	FWHM x	10.29 ± 0.17	6.93 ± 0.25
	FWHM y	10.93 ± 0.17	8.43 ± 0.21
25	FWHM x	8.63 ± 0.16	5.73 ± 0.24
	FWHM y	10.81 ± 0.17	5.13 ± 0.28
80	FWHM x	6.69 ± 0.09	4.80 ± 0.11
	FWHM y	11.48 ± 0.06	6.87 ± 0.07
100	FWHM x	9.00 ± 0.03	5.64 ± 0.04
	FWHM y	8.88 ± 0.03	6.82 ± 0.03
150	FWHM x	9.79 ± 0.02	6.47 ± 0.03
	FWHM y	9.86 ± 0.02	7.54 ± 0.02

Table 4.7: Full Width Half Maximum values of Lorentzian fits applied in x and y to the PSA comparison images from Figure 4.19. FWHM values are given in degrees.

distance images, the overall trends show a clear PSA improvement. The benefits of the new gates are evident in a marked resolution improvement when they are used and as this system is developed these new gates must be employed to produce the highest quality radiometric images.

The resulting fused images of the radiometric data outlined in Table 4.4 are shown in Figures 4.44 and 4.45. There are clear visual improvements gained by applying PSA as the radiometric images become smaller and more defined as a result.

A final note on PSA concerns a comparison of the relative improvements in image resolution offered by the individual detectors that comprise the Compton camera system. It is important to know which detector has the greatest influence on image resolution as this can influence choices on the material, shape and granularity of detectors used in future systems. For the same ^{137}Cs point sources between 5 - 150 cm source-to-scatterer distances, PSA applied solely to the scatterer or absorber crystals and Table 4.8 shows the FWHM fit

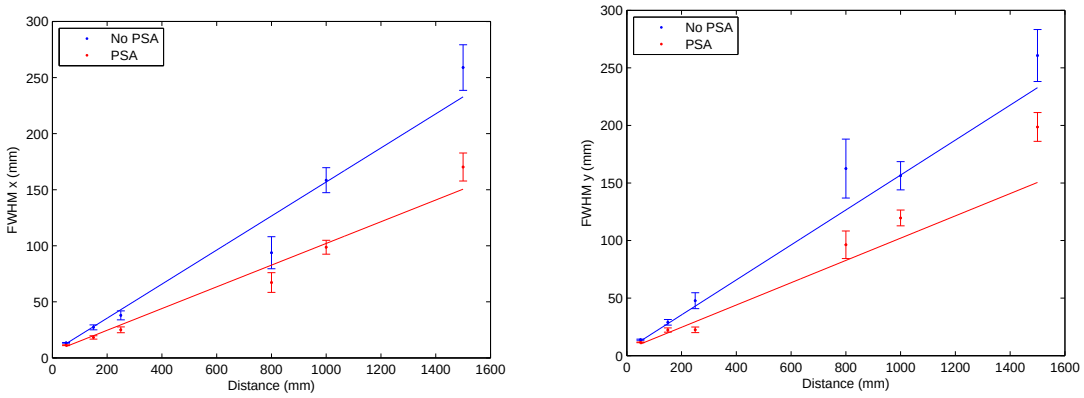

Figure 4.43: Percentage improvements in image resolution as a result of using PSA.

Figure 4.44: Comparison of fused radiometric/rectified stereoscopic images of a ^{137}Cs point source imaged at a standoff distance of 1 m.

values of the reconstructed images.

Over the range of distances there is a clear trend that applying PSA to the absorber gives a greater improvement to image resolution than applying PSA to the scatterer. This may be an inherent feature of this Compton camera setup but it will be affected by the fact that the absorber is four times as large in depth, meaning the improvement to interaction position resolution afforded by PSA is far greater. It has also been shown previously that there were difficulties in choosing the t30/t90 gates that control the chosen interaction positions in the scatterer detector. In the current Compton camera setup however, it can be said that

Figure 4.45: Comparison of fused radiometric/rectified stereoscopic images of a ^{137}Cs point source imaged at a standoff distance of 1.5 m.

optimising the absorber interaction position is more important to image resolution than the scatterer.

PSA improves image resolution at the expense of detection efficiency by gating on events where interactions can be accurately located. An alternative approach was investigated where efficiency could be improved by imaging events with two interactions in the absorber crystal.

Imaging Fold Two Events

For an event to be accepted for use in basic Compton imaging, it must Compton scatter once in the scatterer and be fully absorbed in one interaction in the absorber. This corresponds to one true charge pulse collected at one electrode on each side of both detectors. This is known as a Fold 1 event or can be referred to as Fold(1,1,1,1). In reality any number of interactions can occur in each detector leading to a large number of events that are rejected due to the difficulty in correctly back projecting the cone as it is unclear which interaction occurred first. A typical range of event fold in the absorber detector is shown in Figure 4.46, a reproduction of Figure 4.8.

It is proposed that Fold 2 events in the absorber can also be imaged provided assumptions are made about the order in which the two interactions occurred, thus potentially increasing the efficiency of the system. The method is highlighted schematically in Figure 4.47, which

Distance (cm)		Scatterer PSA Only	Absorber PSA Only
5	FWHM x	12.89 ± 0.31	12.35 ± 0.39
	FWHM y	11.60 ± 0.31	13.17 ± 0.36
	Max Counts	683	630
15	FWHM x	26.48 ± 2.89	22.72 ± 2.12
	FWHM y	25.39 ± 2.97	20.52 ± 1.80
	Max Counts	156	176
25	FWHM x	43.69 ± 6.15	29.00 ± 3.61
	FWHM y	44.53 ± 6.95	27.97 ± 3.79
	Max Counts	90	123
80	FWHM x	135.27 ± 21.67	83.55 ± 8.71
	FWHM y	205.92 ± 38.26	103.33 ± 17.94
	Max Counts	55	76
100	FWHM x	152.69 ± 11.98	111.57 ± 6.74
	FWHM y	174.16 ± 12.67	139.61 ± 8.36
	Max Counts	222	304
150	FWHM x	245.95 ± 17.95	170.63 ± 11.02
	FWHM y	222.01 ± 22.21	194.98 ± 13.41
	Max Counts	139	186

Table 4.8: Full Width Half Maximum values of Lorentzian fits applied in x and y. FWHM values are given in mm.

considers a Compton camera consisting of two detectors with three electrodes each. The left diagram shows a typical Fold(1,1) event with one interaction in one strip of each detector, while the centre shows a Fold(1,2) event with one interaction in the scatterer and two in the absorber. The energies deposited from the first, second and third interactions are denoted E_1, E_2 and E_3 respectively. The right diagram shows that in an ideal case more energy was deposited in the second interaction than in the third of the Fold(1,2), so the third interaction is ignored and the second interaction is taken as the single energy deposition in the absorber. The energy of this deposition is recovered by summing E_2 and E_3 and this event can now be imaged.

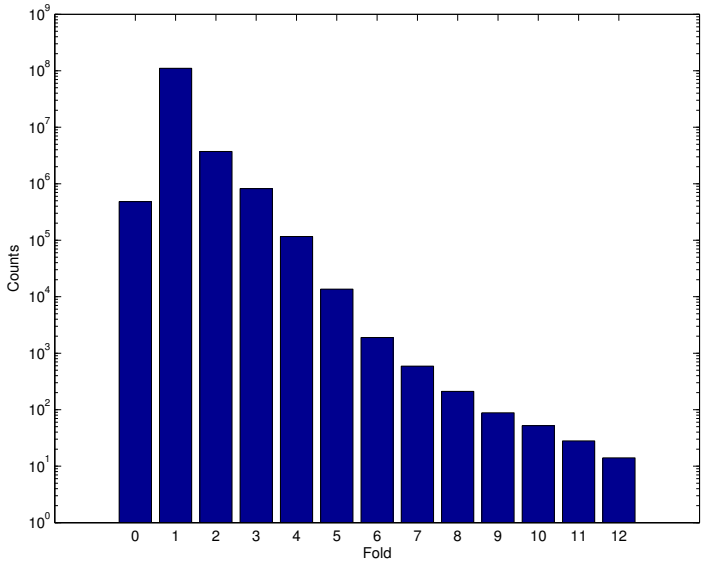

Figure 4.46: Absorber event fold for ^{137}Cs point source data placed 5 cm from the scatterer crystal face. Reproduced from Figure 4.8.

Even small mistakes in interaction position in the scatterer can have a large effect on the back projected cones so Fold 2 events in the scatterer cannot currently be imaged using this method. It was decided to focus on recovering Fold 2 events on either side of the absorber, or Fold(1,1,1,2), Fold(1,1,2,1) and Fold(1,1,2,2) events. Using the method outline above, three sets of images were created from a ^{137}Cs dataset 5 cm from the scatterer. These were comprised of Fold 1 events only, Fold 2 imaging events only and a combination of Fold 1 and Fold 2 imaging events. Preliminary analysis was undertaken to investigate whether only Fold 2 events involving adjacent strips should be used or if interactions involving any two strips can be imaged. A possible image improvement by using adjacent Fold 2 events only was hypothesised following work into the AGATA γ ray tracking algorithm [92]. Two figures have been reproduced from this Thesis in Figure 4.48 that are a result of a GEANT4 [93] simulation into energy distribution and interaction separation in Fold 2 HPGe events. It states that correctly reconstructing the γ event depends on identifying the first interaction in the crystal and as the figure shows, the chance of the first interaction having the largest energy deposition varies as a function of energy. By only accepting adjacent strip events, it

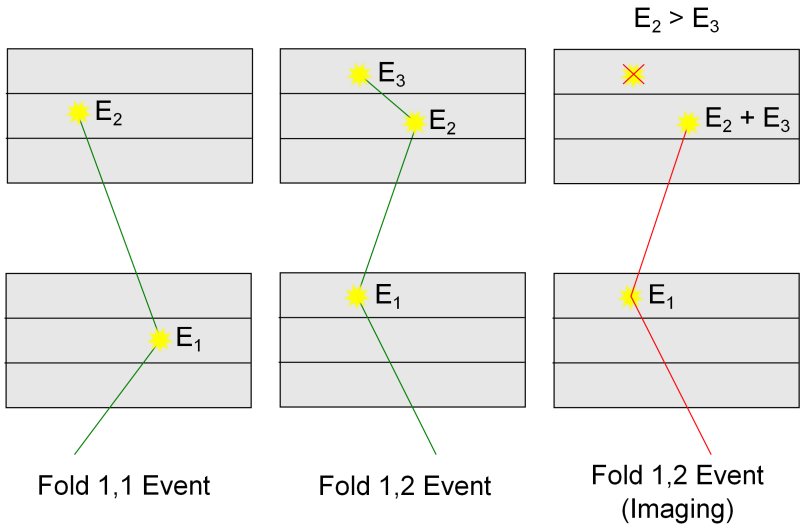

Figure 4.47: A schematic diagram of a Fold 1,1 and Fold 1,2 event in the absorber, with an example of how Fold 1,2 events can be imaged by summing the energies of Fold 2 events and taking the interaction with the most energy as the Fold 1 position.

was hoped the average interaction distance could be reduced and that the negative effect of misidentifying first interactions would be limited. This was tested using ^{137}Cs data which has a strong peak at 662 keV, giving a most probable energy deposition in the absorber of around 473 keV (from the Klein-Nishina formula). Fold 2 interactions of this energy have a strong chance that the first interaction does not deposit the most energy as there is a strong likelihood of multiple scatters in subsequent voxels with decreasing distance between interactions. This means that there is an increasing chance later interactions will occur in the same voxel and be counted as a single interaction with summed energy.

Figure 4.49 shows the percentage of raw coincident events that can be imaged by different means for an entire ^{137}Cs point source dataset 5 cm from the scatterer crystal. 43.3% of coincident events are Fold(1,1,1,1) and can be imaged using basic techniques. Considering Fold 2 events in the absorber, 33.1 % of events can be recovered if all strips are considered whereas only 5.8% can be recovered if only adjacent Fold 2 events are used. This leads to total respective imaging percentages (when combined with Fold(1,1,1,1) events) of 76.4% and 67.4%, a justifiable decrease in counts if the resulting images are significantly improved.

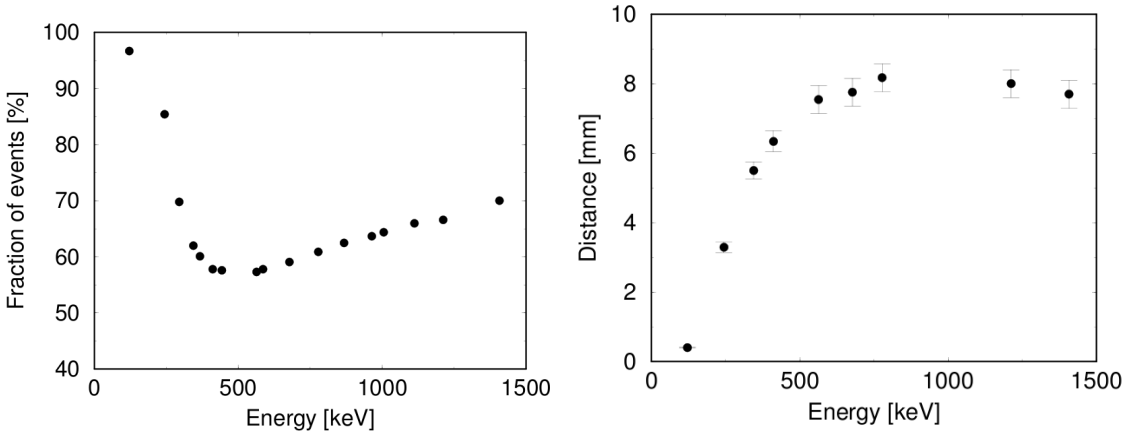

Figure 4.48: Percentage of Fold 2 events where the first interaction has the largest energy deposit as a function of energy(left). Average distance between interactions in Fold 2 events as a function of energy (right). Reproduced from Dr Martina Descovich's Thesis [92].

To obtain the optimal image quality all Fold 2 events will be used in subsequent investigations in this thesis but gating on adjacent events only it may be possible to reduce the number of strips that have to be processed and thus improve data throughput.

To ensure it was sensible to take the highest energy interaction as the first, Fold 2 images were reconstructed using this approach. By comparing them to Fold 1 images and Fold 2 images where the lowest energy interactions were taken as first the method could be validated. These are shown in Figure 4.50.

It is clear that taking the higher energy interaction as first in a Fold 2 image gives a well reconstructed image with the source clearly visible. Comparing with the Fold 1 image, the constructed source positions are in good agreement with a difference of 0.2 mm in x and 1.0 mm in y. In these figures the Fold 2 image has slightly better resolution of 19.7(12) mm and 20.7(7) mm in x and y compared to 20.2(11) mm and 22.2(11) for the Fold 1 image, though as will be shown this does not hold for increased distances. The Fold 2 image where the lowest energy interaction is taken as first is shown not to work correctly, as a large blob is reconstructed that has no bearing on the true source position.

Having shown Fold 2 imaging is viable, Figure 4.51 is a more detailed comparison of the resolution of reconstructed images. It shows three reconstructed images of a ^{137}Cs point source 1 m from the scatterer crystal; top-left is a Fold 1 image, top-right is a Fold 2 image

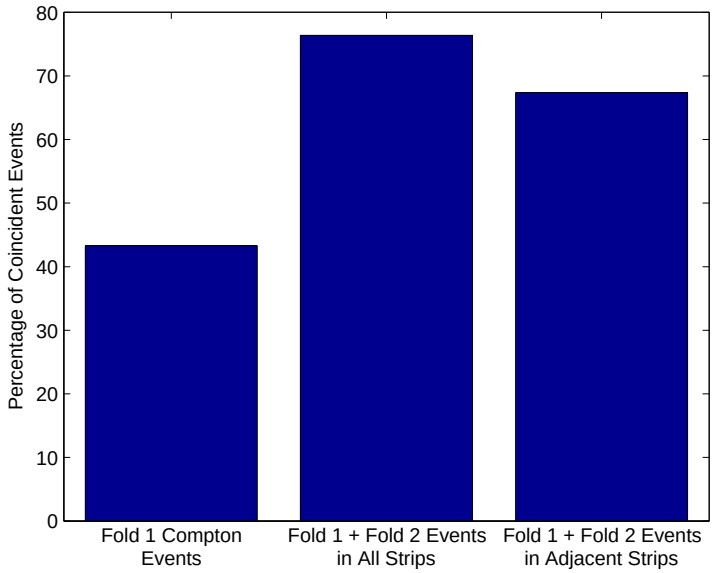

Figure 4.49: Events accepted for Fold 1, Fold 1 + all Fold 2 and Fold 1 + adjacent Fold 2 event configurations as a percentage of total coincident events for a full ^{137}Cs dataset 5 cm in depth from the scatterer crystal.

and bottom is a combined Fold 1 + Fold 2 image.

Table 4.9 shows the FWHM values of the images in Figure 4.51. All are clear images, though in this case the Fold 2 FWHM values are around 14 % larger in x and 3 % larger in y. When reconstructing an image using Fold 1 and 2 events you get a 76% increase in events, with a 10 % increase in x FWHM and a 6 % increase in y. The degradation in image resolution is relatively small compared to the huge increase in sensitivity afforded by imaging Fold 2 events and this method could prove very useful in applications involving low activity sources. However when image resolution is the primary goal and a drop in sensitivity can be managed, using PSA is a more practical imaging approach.

Efficiency

As the efficiencies were so low in the previous February 2013 experiments, steps were taken to try and improve this. The coincidence time window was previously set at 75 ns on the basis of a timing spectrum measurement between scatterer and absorber interactions col-

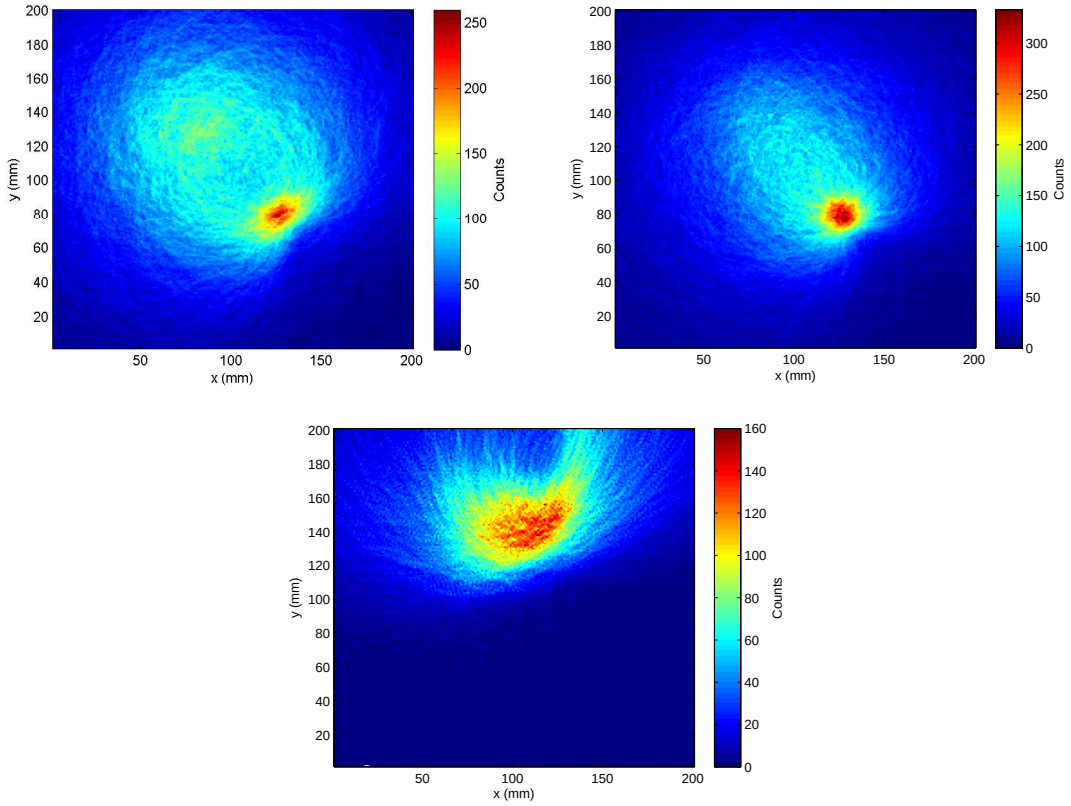

Figure 4.50: Images from a ^{137}Cs dataset 5 cm from the scatterer crystal in depth and ∼5 cm in x and y. A standard Fold 1 image (top-left), a Fold 2 image where the highest energy interaction is taken as the first (top-right) and a Fold 2 image where the lowest energy interaction is taken as first (bottom) are shown for comparison.

	Fold 1	Fold 2	Fold 1 + Fold 2
FWHM x (mm)	163.65 ± 6.61	186.31 ± 6.39	180.01 ± 4.84
FWHM y (mm)	169.07 ± 7.93	173.82 ± 6.42	179.09 ± 5.39

Table 4.9: Full Width Half Maximum values of Gaussian fits applied in x and y to the Fold 2 comparison images from Figure 4.51.

lected by the CAEN V1724 cards, but it was discovered that these results were incorrect. A following experiment using a Si(Li)/HPGe Compton camera with the same electronic setup [87] increased the coincidence time window to 250 ns and saw an improvement in efficiency, so this was adopted for the June 2013 experiments. Figure 4.52 shows the com-

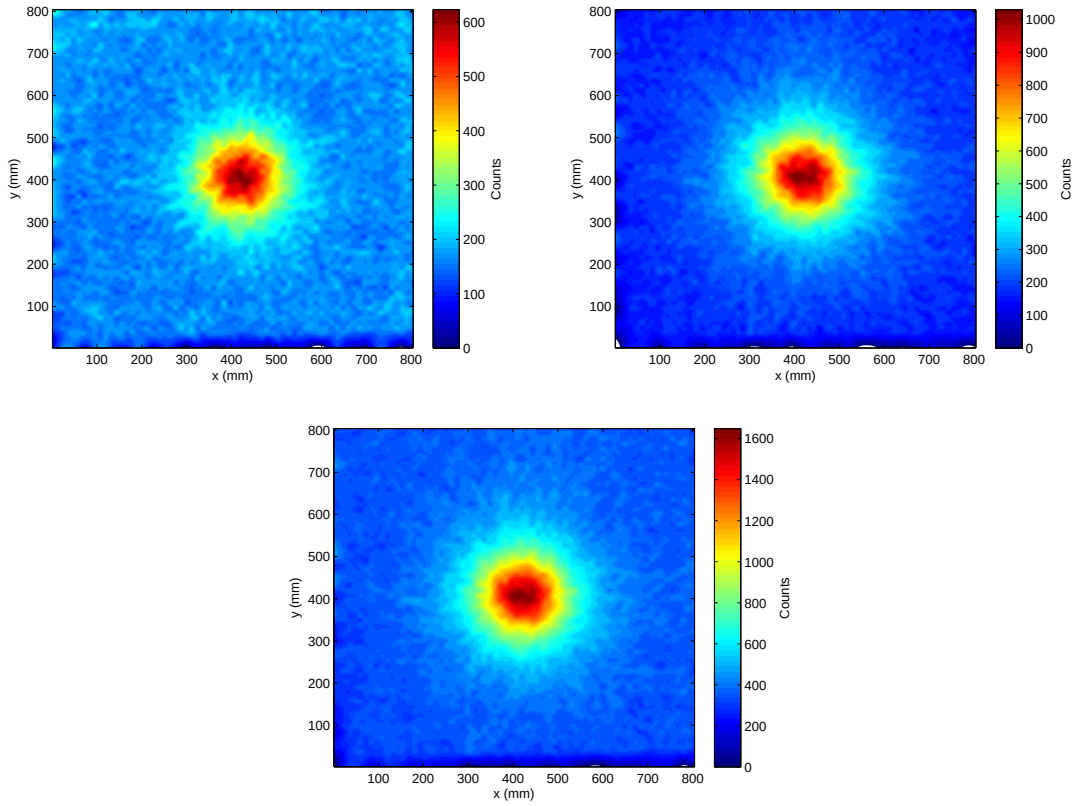

Figure 4.51: Images from a ^{137}Cs dataset 1 m from the scatterer crystal in depth. A Fold 1 image (top-left), a Fold 2 image (top-right) and a combined Fold 1 + Fold 2 image (bottom) are shown for comparison.

parison between the efficiencies of the February 2012 and June 2013 experiments against the efficiency expected by simulation. As can be seen there is a significant efficiency improvement in this latest experiment compared to the previous one but the system is not as efficient as predicted by GAMOS. The significant differences between the GAMOS validation experiment and those carried out in this project are the use of a new scatter detector (5 mm HPGe has been used in place of 20 mm HPGe) and the switch from analogue to digital electronics. As the scatterer has been seen to work as expected throughout this project it seems possible that electronic settings that aren't fully understood are to blame for the drop in statistics.

Figure 4.53 compares the efficiencies of respective imaging algorithms, highlighting the

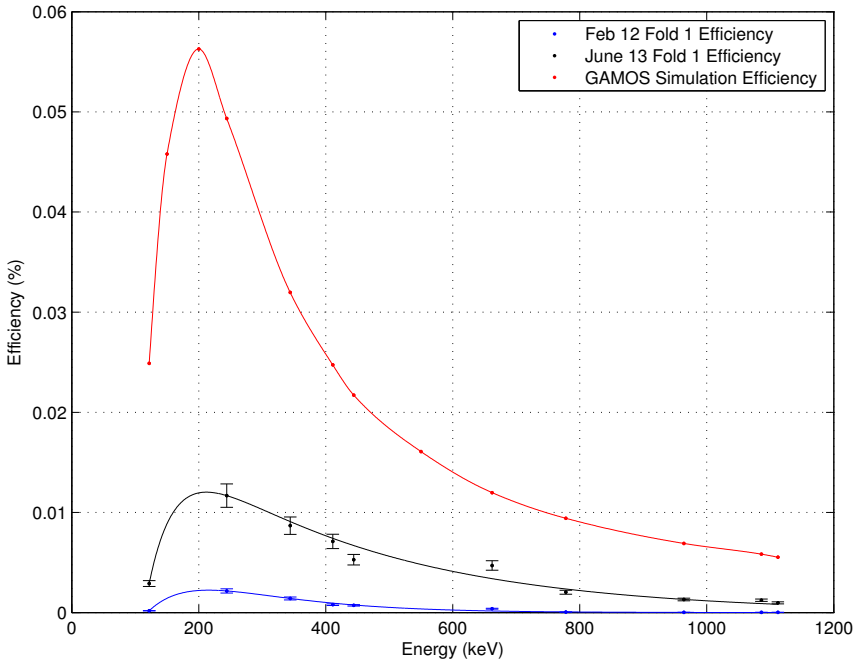

Figure 4.52: Fold 1 absolute efficiency measurements as a function of energy for the February 2012 experiments, June 2013 experiments and GAMOS simulations (5 cm from the scatterer crystal). Reproduced from Figure 4.20.

tradeoff between image quality and efficiency. As shown in the previous figure, the efficiencies were much higher in this experiment than the previous one and this is reflected in the efficiency of all imaging approaches. The efficiency at lower energies is significantly reduced for PSA imaging compared to the other approaches, though the difference between them decreases as the energy increases. This is due to the fact that smaller energy deposits will lead to smaller image charges and if these are inseparable from noise the event will be rejected by PSA gates, leading to a lower PSA efficiency. As there were no other sources of sufficient strength available to image the effect of energy on resulting PSA image quality could not be investigated, but this will be crucial to ensure PSA is applied correctly. It would be safe to assume that energies above 662 keV would show similar improvement by applying PSA but there may be an energy limit below which the problems associated with the drop in efficiency outweigh the improvements. The improvement in efficiency by imag-

ing Fold 2 events is evident and holds across the energy range when compared to only Fold 1 events. Eventually an implementation of event quality classification could be used where by the quality of an image could be judged by the interactions involved in the events that constructed it. This would allow all imaging events to be used with a threshold based on the individual requirements of image resolution and efficiency.

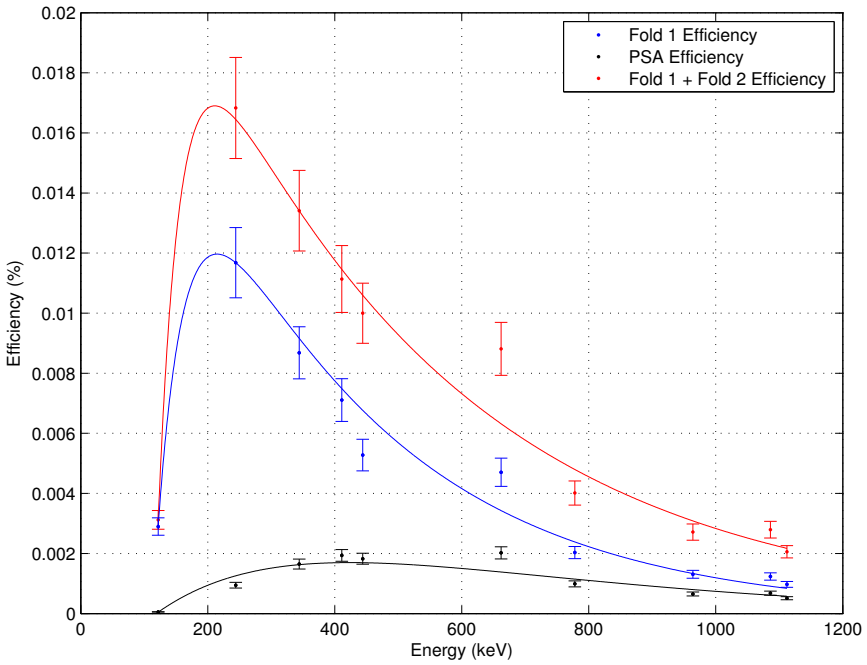

Figure 4.53: Absolute efficiencies as a function of energy for different event selection approaches from the June 2013 experiments (5 cm from the scatterer crystal).

The proof of concept of a radiometric and stereoscopic fused system has been achieved. The images fuse correctly, the radioactive source is easily located in each case and the physical objects of the image are adequately defined. These images show that it is possible to create a system that harnesses this image fusion to accurately determine the location of gamma emitting radioactive sources. The next stage of this project is to develop this work from a collection of laboratory detectors that provide limited functionality to a cohesive standalone unit that delivers all the functions required for use in a nuclear decommissioning environment. The next chapter will discuss the challenges to be faced when achieving this

and provide a potential framework for project development.

Chapter 5

Conclusions and Discussion

This thesis presents the proof of concept of a radiometric and stereoscopic fused vision system. While considerable progress has been made, the aims of this project exceed the scope of this thesis and it is important the work completed to date is used as a basis for the future development of this project. To this end, the salient points of the research undertaken for this thesis are summarised below.

5.1 Conclusions

Two major experiments and their subsequent analysis were presented in this thesis. This work has furthered the understanding of pulse shape analysis, Fold 2 imaging, radial image disparity and radiometric and stereoscopic image fusion. The specific progress has been quantified and itemised below.

5.1.1 Compton Camera Experiments: February 2012

Initial research concentrated on the image optimisation of a planar HPGe Compton camera. This was investigated from two approaches, the first using Pulse Shape Analysis to improve interaction position resolution and ultimately image resolution. The second was an in depth study into the disparity between source and image position followed by work to correct the discovered disparity. From this work the following conclusions were drawn:

- The 5 mm + 20 mm HPGe Compton camera works correctly and can be used to obtain images of gamma-ray emitting radioactive sources.

- Pulse shape analysis can be used to improve position resolution and ultimately radiometric image resolution. PSA can only be applied to single site interactions and finding the derivative of the collected charge pulse can give a good indication of the number of interactions in a given voxel. The current implementation of PSA improves image resolution by 30.0% in x and 29.5% in y on average.

- Optimising the absorber interaction position is currently more important than optimising the scatterer interaction in this Compton camera setup.

- There is a marked loss in efficiency when compared to simulations that is not currently understood. There is a slight variation with energy, with only 11.6% of expected counts recorded at 112 keV and 19.1% of expected counts at 662 keV (above which the percentage remains close to constant). As the potential efficiency improvement is a key feature driving the development of the Compton camera it is critical work is carried out to ensure this efficiency loss is understood and corrected.

- There is a discrepancy between source and image location as a function of the distance between the source and the centre of the scatterer detector. It is a radial 'pincushion' effect that can be corrected for using techniques typically employed in optical camera calibration. Iterative algorithms gave the best current estimate of distortion parameters as

$$k = -8.73 \times 10^{-5}, k2 = 1.09 \times 10^{-8}, \theta = 1.62\, mm. \tag{5.1}$$

  This corresponds to an improvement in image position accuracy by over a factor of 26. The experiment was not accurate enough to be confident that these parameters are correct. Further experiments that collect a higher number of counts from accurately positioned sources are needed to fully characterise detector image disparity response, as are investigations into the effect of source energy on image disparity.

5.1.2 Stereoscopic Fusion Experiments: June 2013

Once the Compton camera images have been optimised and image disparity had been investigated the focus of this project was to provide the proof of concept of a fused radiometric and stereoscopic imaging system. First a proprietary stereoscopic camera was chosen

based on the requirements of the project and this camera was tested to ensure it fulfilled these requirements. Following this experimental data was taken using the radiometric and stereoscopic cameras simultaneously using ^{137}Cs sources of high activity, imaged from long standoff distances. From this data the first fused radiometric and stereoscopic images were produced, while a GUI was developed in Matlab to make image fusion a quick and simple process for future users. From this work the following conclusions were drawn:

- The Bumblebee XB3 stereoscopic camera was chosen for use in this project. It provides libraries for camera control and image capture in a Linux environment. The stereoscopic images produced were sufficient though the camera does have trouble imaging bland or repetitive surfaces. Overall the Bumblebee XB3 is the right choice for this project but further work into optimizing the stereoscopic camera settings may yield more accurate images.

- Simultaneous acquisition of stereoscopic and radiometric data has been achieved. The ^{137}Cs source was successfully imaged from a maximum distance of 1.5 m that represents the longest standoff distance ever imaged using Compton cameras at the University of Liverpool.

- Fusion of radiometric and stereoscopic images has been achieved. The fused images were successfully produced in Matlab as part of a GUI that also incorporates Dr Dan Judson's filtered back projection algorithm, allowing radiometric images to be processed in a Windows environment. The radiometric image was correctly positioned on the stereoscopic image making the gamma-ray emitting source clearly visible. These images demonstrate the proof of concept of this system.

- Pulse shape analysis produces visibly improved fused images. By refining the shape of pulse risetime gates to more closely follow the expected values interaction position and image resolution can be further improved upon. Using PSA causes a significant reduction in efficiency but the improvements in image resolution outweigh this in some cases. At low energies the efficiency reduction is accentuated and this may prove to be a problem when imaging low energy sources.

- Imaging Fold 2 events in the absorber detector is a possible technique for improving image efficiency. This is most effective for higher energy radioactive sources laterally

positioned in the centre of the Compton camera field of view. Further investigation and novel reconstruction techniques are needed to make Fold 2 imaging a viable prospect.

5.2 Future Work

The work presented in this thesis shows the initial research undertaken towards developing a fused radiometric and stereoscopic system for use in a nuclear decommissioning environment. While good progress was made there are still many challenges to overcome before the finished system is ready to use and now the initial research has been completed these challenges can be more clearly defined. The future work can be broadly split into two categories: problems discovered in the completed research that require further investigation and novel research that will build upon the completed work to progress the project beyond proof of concept.

5.2.1 Further Investigation of Current Research

While the research for this thesis was largely successful there were problems that must be addressed but cannot be within the timescale of this initial work. These problems are outlined below and ideas on how to overcome them are discussed.

- The current efficiency problems must be investigated as a priority. The CAEN V1724 digitizer cards have been tested to ensure there are no dead time issues, while the computing power used has been shown to be sufficient for processing the raw data. As the Compton camera setup has been validated against simulations using analogue electronics [88] it still seems likely that the drop in statistics has been caused by switching to digital electronics. Tests have been made using pulsers to send a fixed rate of pulses to the CAEN digitizer cards and using a CAEN scaler card to read the number of pulses processed by the digitizer. These tests have shown the input rates are the same as recorded by the cards and this holds true for rates far exceeding those in this experiment. This means the cards appear to be working as expected and the cause of the efficiency problems remains unknown.

- Once the efficiency problems are fixed it is important that a high statistics radiometric image disparity experiment is undertaken. As the work in this thesis has shown the

pincushion effect is symmetric it will be unnecessary to use an entire grid of measurements; a quarter of the grid will show the same disparity response as the other three. By reducing the grid size it should be possible to either add more measurements to the grid quarter or collect a greater amount of statistics for the remaining measurements. The position of the radioactive source used must be known to a high degree of accuracy as the uncertainty of the source position used in the previous experiment led to obvious systematic errors. Once distortion parameters are calculated from an accurate set of source positions they should hold for all future data collected using the same system in the same configuration and this will also have to be verified. Once complete, these distortion parameters should be able to correct for any radial distortion and future images will incorporate these to automatically recreate the correct source location. Alternatively refining simulations to validate their radial disparity response against the experimental work would allow a number of different energies, positions and detector configurations to be simulated, optimising the distortion parameters quickly and cheaply.

- The effects of applying PSA as a function of energy must be investigated to ensure the fused images are optimised over a wide range of energies. The experimental data found there was a marked reduction in efficiency when applying PSA to lower energy pulses and there may be a limit at which this outweighs the improvements in image resolution achieved by applying PSA. Measuring pulses from known interaction locations in the 5 mm scatterer crystal could yield risetime information that could be used to improve the gates used in PSA while reductions in system noise would help to separate small image charges from noise. If these small image charges can be identified their associated interactions can be used in PSA resulting in efficiency improvements.

- A more detailed investigation into imaging Fold 2 events (and above) would allow higher fold imaging to be implemented when efficiency is a priority over image resolution.

- Many concepts have been introduced in this thesis and have been shown to work under certain conditions, but their limits have yet to be tested. What is the limit of imaging distance and detectable activity of this system? How does it cope with diffuse source

shapes? It is these questions that will potentially prove this system to be the clear device of choice for nuclear decommissioning.

5.2.2 Research Beyond the Scope of this Thesis

The work completed for this project so far has been undertaken exclusively in a laboratory environment using experimental detectors. The resulting fused images, while accurate, can only be developed individually and require a number of different steps to generate. The next stage of this project will likely have two main areas of focus: onsite testing of the current system and development of real-time fusion algorithms.

- Now that fused images have been collected in the laboratory, the same tests must be proven to work in a nuclear decommissioning environment. There will be challenges for both imaging modalities; stereoscopic imaging may struggle if the environments are bland or repetitive, while the radiometric imaging will have to be able to cope with stronger sources, increased standoff distances and increased levels of background radiation. Whilst these problems may make imaging difficult, this environment will be hugely beneficial in understanding how the system copes in practical situations as opposed to carefully controlled laboratory experiments. The data gathered from onsite tests should help inform choices on the parameters of the final fused imaging system and potentially drive research into novel techniques to overcome the challenges of the nuclear decommissioning environment. These tests will likely be of use in other Compton projects, particularly homeland security applications.

- The GUI presented in this thesis proved the concept of fused imaging but has little practical use for real time identification and quantification of radioactive sources. The algorithms developed can be used as a basis for the software however, as the image generation and fusion codes work correctly and efficiently. The most important step will be to use a well supported data acquisition environment that can process code from a number of different sources, notably C++ and Matlab in this case. To this end the LabVIEW environment [94] should be given serious consideration for use as the DAQ software for this project. It is a widely used piece of system design software with a large user base in industry and well supported integration of C++

and Matlab codes. Furthermore there are official drivers for communication between LabVIEW and the CAEN V1724 digitizer cards used in this project, making it easier to output the raw data from the electronics into LabVIEW. With this setup imaging events could be passed to the back projection imaging algorithm as soon as they are processed and using the C++ camera control libraries images could be acquired from the stereoscopic camera automatically or as the user desires. The Matlab GUI could be built into this LabVIEW environment allowing real time fused images to be produced and the system at this stage would be much more representative of a commercial system than the current set up.

- It would be beneficial to develop the simulation of the experimental data using more comprehensive tools that account for the digital processing of the collected charge. This would allow PSA to be applied to simulated data, providing a comparison for the optimised Compton camera in its current state. In addition, the rise time and multiple interaction gates could be understood in greater depth, optimising the acceptance of events that PSA can be applied to.

- Something that has not been touched upon in this thesis but may prove to be critical is the development/use of alternative radiometric imaging algorithms. The filtered back projection algorithm employed in this work is used as it is relatively quick to process events, leading to efficient image generation. It has drawbacks however, not least the difficulty in ascertaining image depth correctly. There are other algorithms that, while generally more computationally expensive, can lead to accurate image resolution in x, y and z. An approach worth considering is the stochastic algorithm [95], an iterative method. Iterative reconstruction considers the problem of image generation from a different perspective compared to analytical methods; while filtered-back projection draws a cone for each event that covers every possible source location, an iterative code will choose a point on the surface of the cone thereby making a guess at the source location. Every event is processed in this fashion and an image is reconstructed from these guesses where a large amount of them will be incorrect, giving a poor image. From this point the initial guesses influence the next set of points. For each point if the image is deemed to improve this new guess will be kept as the true event, if not the old guess will be kept. By continually guessing the path of each gamma ray the

image should converge to an optimum quality which should have a significant noise reduction compared to filtered back projection images.

There are similarities between this method and the iterative method used to correct for image disparity in Chapter 4.1.2. However radial distortion had only two unknowns (the distortion parameters), whereas the scattering angle of each event is an unknown in Compton camera iterative algorithms (in one spherical dimension θ, it is known in the other dimension ϕ). This means that the processing time required to converge on an optimal image is huge; as shown in [95] 500 iterations of 420000 counts took 2442 s whereas image processing of 52469 counts in the Matlab GUI takes 1.4 s. This equates to a factor of 427 increase in processing time by switching to iterative reconstruction (though this only a rough estimate as the processing was carried out on two different computers). However the potential image improvements mean that it is worth developing an iterative algorithm and as computing power improves the increased processing time may be significantly reduced in the future.

Appendix A

Experimental Measurement Log

This appendix will act as a reference for detailed data about each dataset collected in experimental measurements for this project.

A.1 Compton Camera Experiment: February 2012

This experiment used the 5 mm + 20 mm HPGe Compton camera system outlined in Chapter 3 and the procedure was explained in Chapter 4:

- The DC side of scatterer and the AC side of the absorber was facing the source.
- The energy thresholds of both detectors were set to be around 7 keV.
- The time coincidence window between both detectors was set to be 75 ns.
- A square scan grid of 6 x 6 positions separated by 20 mm in x or y was measured for each dataset.
- Each position measurement was collected for 5 hours.

A.1.1 Radioactive Sources Used

Source	NPRL Number	Half-life (d)	Initial Activity (MBq)	Time Between Initial Activity and Measurement (d)	Activity at Time of Measurement (MBq)
^{137}Cs	194	10982.84	0.424	12008	0.1987
^{137}Cs	304	10982.84	0.037	10052	0.0196
^{137}Cs	471	10982.84	0.331	5596	0.2325
^{152}Eu	287	4944.29	0.437	10275	0.1035
^{152}Eu	461	4944.29	0.370	5618	0.1683
^{60}Co	504	1925.34	0.459	4602	0.0876
^{22}Na	485	950.32	0.363	5281	0.0077

Table A.1: Radioactive source information for those used in the February 2012 Compton camera experiment.

A.1.2 Measurements Taken

Run Number	Source (NPRL)	Distance From Scatterer Crystal (mm)	Rates (s^{-1})	Notes
52/53	^{137}Cs (471)	50		Measurement crashed halfway through measurements, continued with R53
58	^{137}Cs (471)	100	15	
66/67	^{137}Cs (471)	140		Last two data points missed, collected in R67
68/69/70	^{152}Eu (461)	50	25	Two crashed, full measurement collected across three datasets
72/73	^{152}Eu (461)	100	10	Measurement crashed halfway through measurements, continued with R73
74	^{60}Co (504)	50	10	6 position diagonal line dataset taken across square grid due to low statistics
75	^{152}Eu (461)	140	8	
79	^{137}Cs (471)	100	8	Detector separation increased to 9.5 cm
84	^{152}Eu (461)	100		Detector separation increased to 9.5 cm

Table A.2: Dataset information for the February 2012 Compton camera experiment.

A.2 Image Fusion Experiment: June 2013

This experiment used the 5 mm + 20 mm HPGe Compton camera system outlined in Chapter 3 in conjunction with the Bumblebee XB3 steroscopic camera described in the same chapter and the procedure was explained in Chapter 4:

- A 20 MBq ^{137}Cs point source was used to collect image fusion data.
- Three standoff distances of 75 cm, 1 m and 1.5 m were imaged using this source.
- The time coincidence window between both detectors was set to be 250 ns.
- The energy threshold of the scatterer was 7 keV while the threshold of the absorber was 30 keV.

A.2.1 Radioactive Sources Used

Source	NPRL Number	Half-life (d)	Initial Activity (MBq)	Time Between Initial Activity and Measurement (d)	Activity at Time of Measurement (MBq)
^{137}Cs	192	10982.84	0.405	12419	0.185
^{152}Eu	194	4944.29	0.424	12414	0.074
^{152}Eu	461	4944.29	0.370	6059	0.158
^{133}Ba	496	3838.78	0.443	5529	0.163
^{137}Cs	580	10982.84	18.5	652	17.754

Table A.3: Radioactive source information for those used in the June 2013 Compton camera experiment.

A.2.2 Measurements Taken

Run Number	Source (NPRL)	Distance From Scatterer Crystal (cm)	Rates (s^{-1})	Notes
3	^{152}Eu (194 & 471)	10.5	300	194 - 10.5 cm from 5 mm, 461 - 10.5 cm from absorber
7	^{152}Eu (461)	9.8	2750	Calibration data (20 mm only)
10	^{152}Eu (461)	10	2400	Calibration data (5 mm only)
12	^{137}Cs (192)	5	215	
13	^{152}Eu (461)	5	250	
14	^{133}Ba (496)	5	200	
15	^{137}Cs (192)	15	45	
16	^{137}Cs (192)	25	20	
18	^{152}Eu (580)	80	130	Fusion data
19	^{152}Eu (580)	100	90	Fusion data
20	^{152}Eu (580)	150	50	Fusion data
21	^{152}Eu (580)	5	100	Offset of - 5 cm in x and y from centre of crystals

Table A.4: Dataset information for the June 2013 Compton camera experiment.

Bibliography

[1] Great Britain: Department of the Environment and Scottish Office Great Britain. *Review of Radioactive Waste Management Policy: Final Conclusions*. Cm Series. H.M. Stationery Office, 1995. ISBN 9780101291927. URL `http://books.google.co.uk/books?id=5X\_SAAAACAAJ`.

[2] IAEA (International Atomic Energy Agency). Fundamental safety principles: Safety fundamentals. *IAEA Safety Standards Series No. SF-1*, 2006. ISBN 9201107064. ISSN 1020-525X.

[3] Yangbo Du and John E. Parsons. Update on the cost of nuclear power. *Center for Energy and Environmental Policy Research (CEEPR)*, May 2009.

[4] David Kennedy. New nuclear power generation in the uk: Cost benefit analysis. *Energy Policy*, 35(7):3701 – 3716, 2007. ISSN 0301-4215. URL `http://www.sciencedirect.com/science/article/pii/S0301421507000183`.

[5] Decommissioning campaign complete at uk reactor. *World Nuclear News*, June 2011.

[6] G.B.N.D. Authority. *Strategy: effective from April 2011*. Stationery Office, 2011. ISBN 9780108510472. URL `http://books.google.co.uk/books?id=BVtivyaFjXcC`.

[7] D. F. Leushacke H. Sterner and D. Rittscher. Decommissioning and waste at the greifswald npp site. In *International Conference on Radioactive Waste Management and Environmental Remediation*. Nagoya, 1999.

[8] Food & Rural Affairs Great Britain. Dept. for Environment. *Managing Radioactive Waste Safely: A Framework for Implementing Geological Disposal*. Cm Series.

Stationery Office, 2008. ISBN 9780101738620. URL `http://books.google.co.uk/books?id=BR8\_aIBzC7IC`.

[9] C.R. Bayliss and K. Langley. *Nuclear Decommissioning, Waste Management, and Environmental Site Remediation*. Butterworth-Heinemann, 2003. ISBN 9780750677448. LCCN 2003045383. URL `http://books.google.co.uk/books?id=j2ehiQgVgY4C`.

[10] M. Reginatto, P. Shebell, and K.M. Miller. An application of the maximum entropy method for assessments of residual radioactivity at contaminated sites. *Nuclear Science, IEEE Transactions on*, 43(3):1837 –1841, June 1996. ISSN 0018-9499.

[11] R.M. Harrison, R.E. Hester, J. Walls, F. Livens, and J. Smith. *Nuclear Power and the Environment*. Issues in Environmental Science and Technology. Royal Society of Chemistry, 2011. ISBN 9781849731942. 52 pp. URL `http://books.google.co.uk/books?id=v3dKU51fEjYC`.

[12] E. Wiberg, A.F. Holleman, and N. Wiberg. *Inorganic Chemistry*. Academic Press, 2001. ISBN 9780123526519. 1679 - 1681 pp. LCCN 2001091215. URL `http://books.google.co.uk/books?id=Mtth5g59dEIC`.

[13] Xiaolin Hou. Radiochemical analysis of radionuclides difficult to measure for waste characterization in decommissioning of nuclear facilities. *Journal of Radioanalytical Analytical and Nuclear Chemistry*, 273(1):43–48, June 2007.

[14] F. Lamadie, J.R. Costes, F. Delmas, C. Mahe, P. Girones, and C. Le Goaller. Alpha imaging: first results and prospects. In *Nuclear Science Symposium Conference Record, 2004 IEEE*, volume 3, pages 1594 –1598, October 2004. ISSN 1082-3654.

[15] H.S. Stoker. *General, Organic, And Biological Chemistry*. Brooks/Cole, 2009. ISBN 9780495831464. LCCN 2008934779. URL `http://books.google.co.uk/books?id=Yig6eLv\_O4MC`.

[16] P.T Durrant, M Dallimore, I.D Jupp, and D Ramsden. The application of pinhole and coded aperture imaging in the nuclear environment. *Nuclear Instruments and Methods in Physics Research Section A: Accelerators, Spectrometers, Detectors and*

Associated Equipment, 422(13):667 – 671, 1999. ISSN 0168-9002. URL `http://www.sciencedirect.com/science/article/pii/S0168900298010146`.

[17] M. Woodring, D. Souza, S. Tipnis, P. Waer, M. Squillante, G. Entine, and K.P. Ziock. Advanced radiation imaging of low-intensity gamma-ray sources. *Nuclear Instruments and Methods in Physics Research Section A: Accelerators, Spectrometers, Detectors and Associated Equipment*, 422(13):709 – 712, 1999. ISSN 0168-9002. URL `http://www.sciencedirect.com/science/article/pii/S0168900298010225`.

[18] N.P. Kocherov and The Advisory Group meeting. *Nuclear Data Requirements for Fission Reactor Decommissioning: Proceedings*. INDC-NDS–269. 1993. URL `http://books.google.co.uk/books?id=rGEIRAAACAAJ`.

[19] R. H. Dicke. Scatter-hole cameras for x-rays and gamma rays. *The Astrophysical Journal*, 153(L101), June 1968.

[20] D. E. Copeland and E. W. Benjamin. Pinhole camera for gamma-ray sources. *Nucleonics*, 5:44, 1949.

[21] A. Ganguly. *Essential Physics For Radiodology And Imaging*. Academic Publishers, 2001. ISBN 9788189781842. 63 pp. URL `http://books.google.co.uk/books?id=BBj6icI6eEAC`.

[22] H. O. Anger. Scintillation camera with multichannel collimators. *Journal of Nuclear Medicine*, 5:515–531, 1964.

[23] B.F. Phlips, W.N. Johnson, R.A. Kroeger, J.D. Kurfess, G. Phillips, E.A. Wulf, and P.N. Luke. Development of germanium strip detectors for environmental remediation. *Nuclear Science, IEEE Transactions on*, 49(2):597–600, April 2002. ISSN 0018-9499.

[24] L.E. Smith, C. Chen, D.K. Wehe, and Z. He. Hybrid collimation for industrial gamma-ray imaging: combining spatially coded and compton aperture data. *Nuclear Instruments and Methods in Physics Research Section A: Accelerators, Spectrometers, Detectors and Associated Equipment*, 462(3):576 – 587, 2001. ISSN 0168-9002. URL `http://www.sciencedirect.com/science/article/pii/S0168900200011487`.

[25] F. De Notaristefani and P. Lecoq. *Heavy Scintillators for Scientific and Industrial Applications: Proceedings of the "Cristal 2000" International Workshop*. Ed. Frontières, 1993. ISBN 9782863321287. LCCN 97172970. URL `http://books.google.co.uk/books?id=RdoHBA2fxtEC`.

[26] M. Gmar, O. Gal, C. Le Goaller, O.P. Ivanov, V.N. Potapov, V.E. Stepanov, F. Laine, and F. Lamadie. Development of coded-aperture imaging with a compact gamma camera. *Nuclear Science, IEEE Transactions on*, 51(4):1682 – 1687, August 2004. ISSN 0018-9499.

[27] G. F. Knoll. *Radiation Detection and Measurement*. John Wiley & Sons, fourth edition, 2010.

[28] The Harshaw Chemical Company. Harshaw radiation detectors catalogue. 1984.

[29] Charlotte Meaker Davisson and Robley D. Evans. Gamma-ray absorption coefficients. *Rev. Mod. Phys.*, 24(2):79, April 1952.

[30] C. M. Davisson. Interaction of γ-RADIATION with Matter. In K. Siegbahn, editor, *Alpha-, Beta- and Gamma-ray Spectroscopy*, pages 37 – 78, 1965.

[31] Oskar Klein and Yoshio Nishina. Ueber die streuung von strahlung durch freie elektronen nach der neuen relativistischen quantendynamik von dirac. *Zeit. f. Phys.*, 52: 853–868, 1929.

[32] C.E. Ordonez, A. Bolozdynya, and W. Chang. Doppler broadening of energy spectra in compton cameras. In *Nuclear Science Symposium, 1997. IEEE*, volume 2, pages 1361 –1365 vol.2, November 1997. ISSN 1082-3654.

[33] PJ Nolan. Eurogam-a high efficiency escape suppressed spectrometer array. *Nuclear Physics A*, 520:657, 1990.

[34] Dino Bazzacco. The advanced gamma ray tracking array agata. *Nuclear Physics A*, 746(0):248 – 254, 2004. ISSN 0375-9474. URL `http://www.sciencedirect.com/science/article/pii/S0375947404009625`. Proceedings of the Sixth International Conference on Radioactive Nuclear Beams (RNB6).

[35] Helmuth Spieler. *Semiconductor Detector Systems*. Series on Semiconductor Science and Technology. OUP Oxford, 2005. ISBN 9780198527848. LCCN 2006295669. URL `http://books.google.co.uk/books?id=MUMb3y37yqYC`.

[36] G. Lutz. *Semiconductor Radiation Detectors: Device Physics - Accelerator Physics*. Springer, 1999.

[37] K. Seeger. *Semiconductor Physics: An Introduction*. Advanced Texts in Physics. Springer, 2004. ISBN 9783540219576. LCCN 2004105250. URL `http://books.google.co.uk/books?id=il4nyDF0IJIC`.

[38] E.M. Hussein. *Handbook on Radiation Probing, Gauging, Imaging and Analysis: Volume I Basics and Techniques*. Non-Destructive Evaluation Series. Springer, 2003. ISBN 9781402012945. 183 pp. LCCN 2003273021. URL `http://books.google.co.uk/books?id=gADROD8S93sC`.

[39] A. J. Tavendale. Semiconductor lithium-ion drift diodes as high-resolution gamma-ray pair spectrometers. *Nuclear Science, IEEE Transactions on*, 11(3):191 –200, 1964. ISSN 0018-9499.

[40] L. Mihailescu, W' Gast, R.M Lieder, H' Brands, and H. Jger. The influence of anisotropic electron drift velocity on the signal shapes of closed-end hpge detectors. *Nuclear Instruments and Methods in Physics Research Section A: Accelerators, Spectrometers, Detectors and Associated Equipment*, 447(3):350 – 360, 2000. ISSN 0168-9002. URL `http://www.sciencedirect.com/science/article/pii/S0168900299012863`.

[41] J.C. Whitaker. *Microelectronics 2nd Edition*. Electronics Handbook Series. Taylor & Francis, 2005. ISBN 9781420037593. URL `http://books.google.co.uk/books?id=n-fh3wIPZbkC`.

[42] G. Ottaviani, C. Canali, and A. Alberigi Quaranta. Charge carrier transport properties of semiconductor materials suitable for nuclear radiation detectors. *Nuclear Science, IEEE Transactions on*, 22(1):192–204, Feb 1975. ISSN 0018-9499.

[43] Zhong He. Review of the shockley-ramo theorem and its application in semiconductor gamma-ray detectors. *Nuclear Instruments and Methods in Physics Research Section A:*

Accelerators, Spectrometers, Detectors and Associated Equipment, 463(12):250 – 267, 2001. ISSN 0168-9002. URL http://www.sciencedirect.com/science/article/pii/S0168900201002236.

[44] Ortec Detectors Catalogue. Matching the preamplifier to the detector and the application, 2012.

[45] W.R. Leo. *Techniques for Nuclear and Particle Physics Experiments: A How-To Approach*. Springer, 1994. ISBN 9783540572800. LCCN 93038494. URL http://books.google.co.uk/books?id=8VufE4SD-AkC.

[46] M.C. Cantone and C. Hoeschen. *Radiation Physics for Nuclear Medicine*. Springer, 2011. ISBN 9783642113260. 148 pp. URL http://books.google.co.uk/books?id=s3n1vEHw9wUC.

[47] G. Gilmore. *Practical Gamma-ray Spectroscopy*. John Wiley & Sons, 2011. ISBN 9781119964698. URL http://books.google.co.uk/books?id=S0Dy4hjkmmMC.

[48] W. Dietze, E. Doering, P. Glasow, W. Langheinrich, A. Ludsteck, H. Mader, A. Mühlbauer, W. Münch, H. Runge, L. Schleicher, et al. *Technology of Si, Ge, and SiC / Technologie von Si, Ge und SiC*. Number v. 17. Springer, 1983. ISBN 9783540114741. URL http://books.google.co.uk/books?id=4aYylPYsf90C.

[49] T. Papp, M.-C. Lpy, J. Plagnard, G. Kalinka, and E. Papp-Szab. A new approach to the determination of the fano factor for semiconductor detectors. *X-Ray Spectrometry*, 34(2):106–111, 2005. ISSN 1097-4539. URL http://dx.doi.org/10.1002/xrs.754.

[50] Alan Owens. Spectral degradation effects in an 86 cm^3 ge(hp) detector. *Nuclear Instruments and Methods in Physics Research Section A: Accelerators, Spectrometers, Detectors and Associated Equipment*, 238(23):473 – 478, 1985. ISSN 0168-9002. URL http://www.sciencedirect.com/science/article/pii/0168900285904875.

[51] Ortec Detectors Catalogue. Overview of semiconductor photon detectors, 2012.

[52] R.B. Todd, J.M. Nightingale, and D.B. Everett. A proposed gamma camera. *Nature*, 251:132 – 134, 1974.

[53] J.W. LeBlanc, N.H. Clinthorne, C.-H. Hua, E. Nygard, W.L. Rogers, D.K. Wehe, P. Weilhammer, and S.J. Wilderman. C-sprint: a prototype compton camera system for low energy gamma ray imaging. *Nuclear Science, IEEE Transactions on*, 45(3):943 –949, June 1998. ISSN 0018-9499.

[54] Y.F. Du, Z. He, G.F. Knoll, D.K. Wehe, and W. Li. Evaluation of a compton scattering camera using 3-d position sensitive cdznte detectors. *Nuclear Instruments and Methods in Physics Research Section A: Accelerators, Spectrometers, Detectors and Associated Equipment*, 457(12):203 – 211, 2001. ISSN 0168-9002. URL `http://www.sciencedirect.com/science/article/pii/S0168900200006690`.

[55] L. Harkness, A. Boston, H. Boston, J. Cresswell, F. Filmer, J. Groves, J. Headspith, G. Kemp, I. Lazarus, M. Jones, D. Judson, P. Nolan, J. Sampson, D. Scraggs, and J. Simpson. Development of the prospectus semiconductor compton camera for medical imaging. In *Nuclear Science Symposium Conference Record (NSS/MIC), 2009 IEEE*, pages 2452 –2455, November 2009. ISSN 1095-7863.

[56] K. Vetter, M. Burks, C. Cork, M. Cunningham, D. Chivers, E. Hull, T. Krings, H. Manini, L. Mihailescu, K. Nelson, D. Protic, J. Valentine, and D. Wright. High-sensitivity compton imaging with position-sensitive si and ge detectors. *Nuclear Instruments and Methods in Physics Research Section A: Accelerators, Spectrometers, Detectors and Associated Equipment*, 579(1):363 – 366, 2007. ISSN 0168-9002. URL `http://www.sciencedirect.com/science/article/pii/S0168900207006481`. Proceedings of the 11th Symposium on Radiation Measurements and Applications.

[57] A. Takada, K. Hattori, H. Kubo, K. Miuchi, T. Nagayoshi, H. Nishimura, Y. Okada, R. Orito, H. Sekiya, A. Tada, and T. Tanimori. Development of an advanced compton camera with gaseous tpc and scintillator. *Nuclear Instruments and Methods in Physics Research Section A: Accelerators, Spectrometers, Detectors and Associated Equipment*, 546(12):258 – 262, 2005. ISSN 0168-9002. 6th International Workshop on Radiation Imaging Detectors.

[58] Shigeto Kabuki, Kaori Hattori, Ryota Kohara, Etsuo Kunieda, Atsushi Kubo, Hidetoshi Kubo, Kentaro Miuchi, Tadaki Nakahara, Tsutomu Nagayoshi, Hironobu

Nishimura, Yoko Okada, Reiko Orito, Hiroyuki Sekiya, Takashi Shirahata, Atsushi Takada, Toru Tanimori, and Kazuki Ueno. Development of electron tracking compton camera using micro pixel gas chamber for medical imaging. *Nuclear Instruments and Methods in Physics Research Section A: Accelerators, Spectrometers, Detectors and Associated Equipment*, 580(2):1031 – 1035, 2007. ISSN 0168-9002. URL `http://www.sciencedirect.com/science/article/pii/S0168900207013186`. Imaging 2006: Proceedings of the 3rd International Conference on Imaging Techniques in Subatomic Physics, Astrophysics, Medicine, Biology and Industry.

[59] R.J. Cooper, A.J. Boston, H.C. Boston, J.R. Cresswell, A.N. Grint, A.R. Mather, P.J. Nolan, D.P. Scraggs, G. Turk, C.J. Hall, I. Lazarus, A. Berry, T. Beveridge, J. Gillam, and R.A. Lewis. Smartpet: Applying hpge and pulse shape analysis to small-animal pet. *Nuclear Instruments and Methods in Physics Research Section A: Accelerators, Spectrometers, Detectors and Associated Equipment*, 579(1):313 – 317, 2007. ISSN 0168-9002. Proceedings of the 11th Symposium on Radiation Measurements and Applications.

[60] Gerardus Turk. *Characterisation of the first SmartPET HPGe planar detector.* PhD thesis, University of Liverpool, 2006.

[61] C.E. Lehner, Zhong He, and Feng Zhang. 4 pi; compton imaging using a 3-d position-sensitive cdznte detector via weighted list-mode maximum likelihood. *Nuclear Science, IEEE Transactions on*, 51(4):1618–1624, August 2004. ISSN 0018-9499.

[62] D. Marr and T. Poggio. A computational theory of human stereo vision. *Proceedings of the Royal Society of London. Series B. Biological Sciences*, 204(1156):301–328, 1979. URL `http://rspb.royalsocietypublishing.org/content/204/1156/301.abstract`.

[63] D. Hutber. Active stereo vision and its application to industrial inspection. pages 1–4, February 1991.

[64] M. Xie, Y. Xiong, C. Xiong, and Z. Hu. *Intelligent Robotics and Applications: Second International Conference, ICIRA 2009, Singapore, December 16-18, 2009, Proceedings.*

Lecture Notes in Artificial Intelligence. Springer, 2010. ISBN 9783642108167. 185-194 pp. LCCN 2009940407. URL http://books.google.co.uk/books?id=T4F2SFeoyy4C.

[65] Sonal J. Kaye, Willy R. Kaye, and Zhong He. coded aperture imaging using 3d position-sensitive cdznte detectors. In *Nuclear Science Symposium Conference Record, 2008. NSS '08. IEEE*, pages 711 –713, October 2008. ISSN 1095-7863.

[66] W.R. Hook, R.H. Dishington, and R.P. Hilberg. Contour imaging; a new type of imaging technique. *Proceedings of the IEEE*, 56(7):1218 – 1219, July 1968. ISSN 0018-9219.

[67] D. Scharstein. *View Synthesis Using Stereo Vision*. Number no. 1583 in Lecture Notes in Computer Science. Springer, 1999. ISBN 9783540661597. LCCN 99035631. URL http://books.google.co.uk/books?id=i8OsrUmamxcC.

[68] M. Sonka, V. Hlavac, and R. Boyle. *Image processing, analysis, and machine vision*. Thompson Learning, 2008. ISBN 9780495082521. LCCN 2007921908. URL http://books.google.co.uk/books?id=2PQeAQAAIAAJ.

[69] Point Grey Research. Technical application note tan2008005: Stereo vision introduction and applications, February 2010.

[70] M.Z. Brown, D. Burschka, and G.D. Hager. Advances in computational stereo. *Pattern Analysis and Machine Intelligence, IEEE Transactions on*, 25(8):993 – 1008, August 2003. ISSN 0162-8828.

[71] Point Grey Research. Point grey stereo vision camera catalogue, 2011.

[72] P. Melin and W. Pedrycz. *Soft Computing for Recognition based on Biometrics*. Studies in Computational Intelligence. Springer, 2010. ISBN 9783642151101. 431-432 pp. LCCN 2010934862. URL http://books.google.co.uk/books?id=EYp9bpvP_-QC.

[73] Vincenzo Di Lecce Alberto Amato and Vincenzo Piuri. *Semantic Analysis and Understanding of Human Behavior in Video Streaming*. Springer New York, New York, NY, September 2012. ISBN 9781461454861. URL http://books.google.co.uk/books?id=yfavgKQJGJ8C.

[74] O. Schreer, P. Kauff, and T. Sikora. *3D Videocommunication: Algorithms, concepts and real-time systems in human centred communication*. John Wiley & Sons, 2005. ISBN 9780470022726. 102 pp. URL `http://books.google.co.uk/books?id=fdrTq7cWxmwC`.

[75] Paul Furgale and Timothy D. Barfoot. Visual teach and repeat for long-range rover autonomy. *Journal of Field Robotics*, 27(5):534–560, 2010. ISSN 1556-4967. URL `http://dx.doi.org/10.1002/rob.20342`.

[76] Claron Technologies. Microntracker3 brochure, 2012.

[77] D.S. Judson, A.J. Boston, P.J. Coleman-Smith, D.M. Cullen, A. Hardie, L.J. Harkness, L.L. Jones, M. Jones, I. Lazarus, P.J. Nolan, V. Pucknell, S.V. Rigby, P. Seller, D.P. Scraggs, J. Simpson, M. Slee, and A. Sweeney. Compton imaging with the porgam-rays spectrometer. *Nuclear Instruments and Methods in Physics Research Section A: Accelerators, Spectrometers, Detectors and Associated Equipment*, 652(1):587 – 590, 2011. ISSN 0168-9002. URL `http://www.sciencedirect.com/science/article/pii/S0168900211002543`. Symposium on Radiation Measurements and Applications (SORMA) {XII} 2010.

[78] A.J. Boston, H.C. Boston, J.R. Cresswell, M.R. Dimmock, L. Nelson, P.J. Nolan, S. Rigby, I. Lazarus, J. Simpson, P. Medina, C. Santos, and C. Parisel. Gamma-ray tracking: Characterisation of the agata symmetric prototype detectors. *Nuclear Instruments and Methods in Physics Research Section B: Beam Interactions with Materials and Atoms*, 261(12):1098 – 1102, 2007. ISSN 0168-583X. URL `http://www.sciencedirect.com/science/article/pii/S0168583X07010270`.

[79] CAEN Electronic Instrumentations. Caen product catalogue, 2012.

[80] A. Georgiev, W. Gast, and R.M. Lieder. An analog-to-digital conversion based on a moving window deconvolution. *Nuclear Science, IEEE Transactions on*, 41(4):1116 –1124, August 1994. ISSN 0018-9499.

[81] John Cresswell and Janet Simpson. mtsort sorting program, February 2011.

[82] Reynold James Cooper. *Performance of the SmartPET Positron Emission Tomography System for Small Animal Imaging.* PhD thesis, University of Liverpool, October 2007.

[83] D. Judson. Analytical back-projection compton camera algorithm. private communication, 2013.

[84] Rene Brun and Fons Rademakers. {ROOT} an object oriented data analysis framework. *Nuclear Instruments and Methods in Physics Research Section A: Accelerators, Spectrometers, Detectors and Associated Equipment*, 389(12):81 – 86, 1997. ISSN 0168-9002. URL `http://www.sciencedirect.com/science/article/pii/S016890029700048X`. New Computing Techniques in Physics Research V.

[85] J.T. Bushberg. *The Essential Physics of Medical Imaging, 2e.* Williams & Wilkins, 2002. ISBN 9780683301182. 353 pp. LCCN 20141711. URL `http://books.google.co.uk/books?id=jTAwGTYYiusC`.

[86] D. Scraggs. *Digital Signal Processing Techniques for Semiconductor Compton Cameras.* PhD thesis, University of Liverpool, 2007.

[87] Anthony Sweeney. *Compton Imaging for Homeland Security.* PhD thesis, University of Liverpool, 2013.

[88] L.J. Harkness, P. Arce, D.S. Judson, A.J. Boston, H.C. Boston, J.R. Cresswell, J. Dormand, M. Jones, P.J. Nolan, J.A. Sampson, D.P. Scraggs, A. Sweeney, I. Lazarus, and J. Simpson. A compton camera application for the gamos geant4-based framework. *Nuclear Instruments and Methods in Physics Research Section A: Accelerators, Spectrometers, Detectors and Associated Equipment*, 671(0):29 – 39, 2012. ISSN 0168-9002. URL `http://www.sciencedirect.com/science/article/pii/S0168900211022777`.

[89] A. Gruen and T.S. Huang. *Calibration and Orientation of Cameras in Computer Vision.* Springer Series in Information Sciences. Springer, 2001. ISBN 9783540652830. 103 pp. LCCN 01020735. URL `http://books.google.co.uk/books?id=yY8RB\_yN9k0C`.

[90] R.Y. Tsai. A versatile camera calibration technique for high-accuracy 3d machine vision metrology using off-the-shelf tv cameras and lenses. *Robotics and Automation, IEEE Journal of*, 3(4):323–344, 1987. ISSN 0882-4967.

[91] P.W. Hawkes. *Advances in Imaging and Electron Physics*. Number 156 in Advances in Imaging and Electron Physics Series. Elsevier Science, 2009. ISBN 9780080912004. 34 pp. URL `http://books.google.co.uk/books?id=Z-36P9InswAC`.

[92] Martina Descovich. *Improving the position resolution of Highly Segmented HPGe Detectors using Pulse Shape Analysis Methods*. PhD thesis, University of Liverpool, November 2002.

[93] S. Agostinelli et al. G4–a simulation toolkit. *Nuclear Instruments and Methods in Physics Research Section A: Accelerators, Spectrometers, Detectors and Associated Equipment*, 506(3):250 – 303, 2003. ISSN 0168-9002.

[94] C. J. Kalkman. Labview: a software system for data acquisition, data analysis, and instrument control. *Journal of Clinical Monitoring*, 11(1):51 –58, 1995.

[95] A. Andreyev, A. Sitek, and A. Celler. Stochastic image reconstruction method for compton camera. In *Nuclear Science Symposium Conference Record (NSS/MIC), 2009 IEEE*, pages 2985–2988, 2009. ISSN 1095-7863.